ISSN:2661-4448(online)
2661-443X(print)
Volume 2 No.1 2020

MECHANICAL ENGINEERING SCIENCE

VISER
www.viserdata.com

COMPANY INTRODUCTION

Viser Technology Pte. Ltd. was founded in Singapore with branch offices in both Hebei and Chongqing, China. Viser focuses on publishing scientific and technological journals and books that promote the exchange of scientific and technological findings among the research community and around the globe. Despite being a young company, Viser is actively connecting with well-known universities, research institutes, and indexation database, and has already established a stable collaborative relationship with them. We also have a group of experienced editors and publishing experts who are dedicated to publishing high-quality journal and book contents. We offer the scholars various academic journals covering a variety of subjects and we are committed to reducing the hassles of scholarly publishing. To achieve this goal, we provide scholars with an all-in-one platform that offers solutions to every publishing process that a scholar needs to go through in order to show their latest finding to the world.

Mechanical Engineering Science

VISER

Publisher: Viser Technology Pte. Ltd.

ISSN: 2661-4448 (online)

2661-443X (print)

Frequency: Semi-annual

Add.:21 Woodlands Close, #08-18,

Primz Bizhub SINGAPORE (737854)

https://www.viserdata.com/

Mechanical Engineering Science

Volume 2 No.1 (2020)

CONTENTS

Seeding Performance Simulations and Experiments for a Spoon-Wheel Type Precision Cottonseed-Metering Device Based on EDEM 1

Yudao LI, Shulun XING, Shasha LI, Li LIU, Xiaohui ZHANG , Zhanhua SONG, Fade LI

Simulation and Experimental Study on Load-bearing Deformation Characteristics of 11R22.5 Vehicle Retreaded Tire 9

Qiang WANG , Li JIANG, Xiaojie QI

Modeling size-dependent behaviors of axially functionally graded Bernoulli-Euler micro-beam 17

Shuai WANG, Zetian KANG, Shichen ZHOU, Bo ZHOU, Shifeng XUE

Vibration Frequency Characteristic Study of Two-stage Excitation Valve Used in Vibration Experiment System 30

Yongping WU, Chengwei XIONG, Yi LIU, Jiafei ZHENG , Mingxuan ZOU

Design and Engineering Application of Direct Mixing Lubrication System for Emulsion Pipeline in Secondary Cold Rolling Mill 36

Hangzhe DONG, Yazhen ZHANG, Wantong HU,Zhen-hua BAI,Yan-yan ZHANG

Analytic solution for size-dependent behaviors of micro-beam under forced vibration 48

Shuai WANG, Zhiyong WANG, Feifei WANG, Bo ZHOU, Shifeng XUE

VISER

Viser Technology Pte. Ltd.
Mechanical Engineering Science
doi: 10.33142/mes.v2i1.2615

Research Article Open Access

Seeding Performance Simulations and Experiments for a Spoon-Wheel Type Precision Cottonseed-Metering Device Based on EDEM

Yudao LI[1,2,3] and Shulun XING[1], Shasha LI[1], Li LIU[4], Xiaohui ZHANG [1,2,3], Zhanhua SONG [1,2,3*], Fade LI [1,2,3*]

1 Shandong Agricultural University, Taian, Shandong 271018, China;
2 Shandong Provincial Key Laboratory of Horticultural Machinery and Equipment, Taian, Shandong 271018, China;
3 Shandong Provincial Engineering Laboratory of Agricultural Equipment Intelligence, Taian, Shandong 271018, China;
4 Shandong University, Jinan, Shandong 250061, China.

***Corresponding Author:** Zhanhua SONG, E-mail: songzh6688@163.com; Fade LI, E-mail: lifade@sdau.edu.cn*

Abstract:
To study the effects of seed metering on seeding performance under different motion parameters, a simulation model for a spoon-wheel type seeder was established. A seed meter was tested by using EDEM (Engineering Discrete Element Method) software to simulate its working process at different speeds and tilt angles. The trajectories of individual cottonseeds in the seed-metering device were obtained, concurrently, the stress trend in the grain group was determined as a function of time. The simulation results suggest that at larger speeds, the metering index of the seed meter gradually decreases, while the index and the missing index gradually increase. As the tilt angle increased, the multiples index and missing index gradually decreased, while the multiples index gradually increased. When the seed meter speed reached 50 r/min and the tilt angle was 15°, the seed meter had a relatively good working performance with a seed spacing acceptance index of 92.59%, a multiples index of 1.85%, and a missing rate index of 5.56%. The seed meter was tested on a bench by using a JPS-12 performance-tester bench. At the aforementioned speed and angle, the coefficient of variation for the cottonseed spacing was 2.1%. The field trial results indicated that the multiples and the missing rates were higher than those for the tester bench but still met a passing rate of more than 90%. The coefficient of variation for the seed spacing was less than 10%, suggesting that the design could be used for field sowing. The resulting seeding uniformity was higher under these conditions, which indicates that the seed meter has a better working performance and the bench has a good seeding effect.

Keywords: *spoon-wheel type seeder; EDEM simulation; tester bench; field trial; cottonseed*

1 Introduction

An inevitable trend in the development of modern agriculture in China is the modernization of agricultural machinery and equipment to promote land productivity [1]. A seed metering device is a key planting component, enabling related research to be implemented to facilitate precise cotton sowing. To date, there are two types of precision seed metering devices: pneumatic [2–4] and mechanical. A pneumatic device has low requirements for the shape uniformity of the seed and can be applied to high-speed operations; however, the internal structure is complicated and the maintenance is expensive [5]. A mechanical seed meter has a simple structure, is convenient to manufacture, and has low costs. To date, scholars have conducted in-depth theoretical analyses for mechanical precision seed-metering devices while optimizing the meter. To enhance the uniformity of the spoon-wheel type metering device, Wang et al. [6] designed a cushioning device to reduce the impact velocity of the seed in the seeding tube. Wang et al. designed a combined curved-type retracting spoon for applications as a spoon-type seed metering device [7]. Simulation analyses and experimental verifications have shown that its working performance is good and can meet the requirements of precision cotton-seeding.

Zhang et al. simulated the gas-solid flow in an inside-filling air-blowing maize precision seed-metering device [8], performed by means of a coupling approach of EDEM and computational fluid dynamics (CFD). The qualified rate of the optimized seed-metering device was greater than 93% when the working pressure was above 5.5 kPa,

with a working speed lower than 10 km/h throughout the experiment. The results indicated that the EDEM-CFD coupling approach was a reliable instrument for simulating the physical phenomenon of seed movement in an airflow field.

When the spoon-wheel type cottonseed metering device works, the movement parameters affect the movement of the cottonseeds, which affects the metering quality. To improve the quality of the metering, the optimal working parameters of the device were studied by using both simulations and experiments under different motion parameters. It is understood that non-delinted cottonseed is a bulk material based on the accepted definition of the term. To obtain an optimal combination of factors, the motion parameters of the de-stapled cottonseeds can be simulated by using EDEM software[9], which is a multi-objective simulation package based on the discrete element method. Since the 1990s, scholars around the world have performed EDEM-based analyses on the relative motion of bulk materials and working parts [10-11]. Liao et al. performed EDEM-based analyses on the relative motion of bulk materials and working parts. A numerical study of gas-solid flow in the seed feeding device of an air-assisted centralized metering system was implemented by means of an EDEM and CFD coupling approach [12].

Using the discrete element method, Van Liedekerke [13] established a particle flow model with horizontal and inclined discs. Being experimentally verified, the experimental results were nearly consistent with the simulation results. Dun et al [14] used the EDEM model on the structure of the wheel on a wheel-type seed metering disc to obtain the optimal parameters of the hole-diameter ratio and the inclination angle.

EDEM software was used here to simulate the working process of a spoon-wheel type cottonseed metering device. The motion law for cottonseeds under different characteristic parameters and their effects on the seeding performance of the metering device were studied to find the best relative motion characteristic parameters. Verifications of the tests were also implemented [15].

2 Structure and working principle of spoon-wheel type cottonseed metering device

2.1 Overall structure and working principle of meter

As illustrated in Figure 1, the components of a spoon-wheel type fine cottonseed metering device mainly include a speed-governing device, casing, guiding wheel, partition plate, seeding spoon wheel, and wall of seed hopper[16-17]. As depicted in Figure 2, the work of the seed metering device is divided into five processes: filling, clearing, delivering, guiding, and seeding the seeds.

Following is a description of the components of this device and how it works. Power is provided by the ground wheels. The transmission of power through a speed-governing device drives the guiding wheel and seeding spoon-wheel to rotate in tandem. When the seeding spoon-wheel passes through the filling area and enters the clearing area, the excess cottonseeds in this wheel fall back to the filling area by the force of gravity, so that only one seed remains in the wheel. When the cottonseed moves to the delivery hole on the top of the partition plate, the seed falls into the seed-guide wheel through the opening on the partition plate; the guide wheel turns, carrying the seed through the guiding area to the seeding area; the seed leaves the metering device under the combined action of gravity, centrifugal force, friction and other forces to complete the delivery.

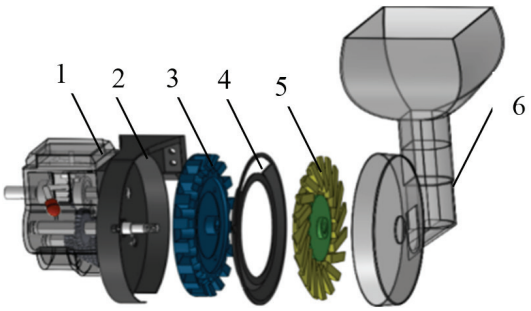

1. Speed governing device, 2. Casing, 3. Guiding wheel, 4. Partition plate, 5. Seeding spoon-wheel, 6. Wall of seed hopper

Figure 1 Structural diagram of spoon-wheel type seed metering device

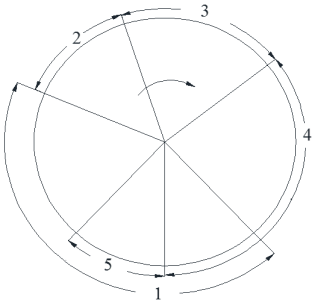

Areas: 1. Filling, 2. Clearing, 3. Delivery , 4. Guiding, 5. Seeding

Figure 2 Diagram of working principles of seed metering device

2.2 Design of critical structure for seed meter and critical speed calculation

As the key structure of the spoon-wheel type seed metering device is its wheel arrangement, the seeding work depends on the size of the inlet hole. Therefore, the empirical formula (1) is used to derive the diameter of the inlet hole to determine whether the seed meter can realize a precise row clock.

$$d = kL_{max} \quad (1)$$

where L_{max} is the maximum size of the cottonseed after classification in mm, and k is a coefficient ranging from 1.1 to 1.3.

The k value is determined from the different wheel forms and seed sizes. When the seed length and width are nearly equal, k takes a larger value. By measuring the size

of the common seed with Shannongmian No. 11 cotton, the average length, width, and thicknesses are 10.07, 6.07, and 5.36 mm, respectively; and the maximum grain size is the length value. The formula is obtained as d = 1.1 × 10 = 11 mm. The width b of the spoon requires more than one-half of the seed length and less than 1.5 times the seed thickness, so that only one seed is in the spoon wheel. Based on previous measurements for the size of cottonseeds, the width of the seed spoon is set at 8 mm.

During the seed-metering operation, if the linear speed of the spoons is too fast, it is difficult for the seed to overcome the centrifugal forces generated by the rotation and the friction between the wheel and the separator. Thus, the seed cleaning cannot be completed, thereby increasing the multiples rate. Concurrently, the high rotation speed reduces the seeding time; thus, the seed cannot enter the seeding wheel from the spoon-wheel, thereby resulting in a missed rate. The critical speed of the seed in suspension is then derived as

$$V_c = \sqrt{gR} \tag{2}$$

where g is the gravitational acceleration at 9.8 m/s^2, and R is the radius of the spoon-wheel in m.

In general, the rotation speed of the seed meter is 70–80% of the critical speed to improve the cleaning and seeding efficiency. It is evident in Formula (2) that the larger the radius of the seed spoon-wheel, the greater the critical speed, which correspondingly improves the seeding efficiency. However, according to the structure of the metering device, the radius of the spoon-wheel should not be too large; therefore, its radius for this research was set at 0.119 m, thus giving a critical speed of 1.08 m/s. The overall structure is illustrated in Figure 3.

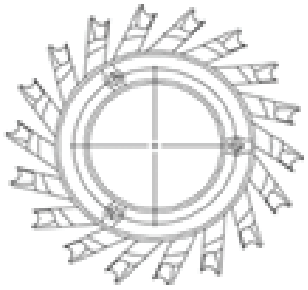

Figure 3 Schematic diagram of spoon wheel

3 EDEM simulation analysis

3.1 Creating a simulation model

EDEM software was used to simulate the working process of the seed meter [18–20]. The most basic step was to create a simulation model of a cottonseed, the shape of which is similar to an ellipsoid with one tapered end and one semi-spherical. The Hertz–Mindlin non-sliding contact model was selected because the surface of the seed is smooth and lacks adhesion [21]. Since it is difficult to accurately draw the shape of cotton kernels with drawing software, a method for splicing balls of different diameters was selected to establish a model of the grain by using a simulation approach, as depicted in Figure 4.

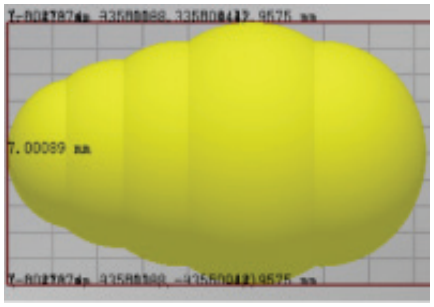

Figure 4 Schematic diagram of simulation model for cottonseeds

The external environment for grain movement is the spoon-wheel type seed geometry model. To reduce the simulation time, the 3D model of the meter removes the speed control device during the preservation process without affecting the simulation results [22]. The resulting structure is illustrated in Figure 5.

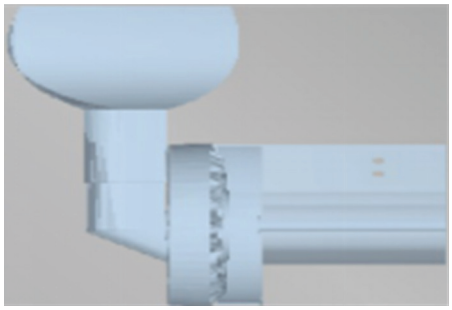

Figure 5 Schematic diagram of simulation model of the seed metering device

3.2 Simulation calculations

First, a fixed time step based on the Rayleigh time step is set. According to formula (3), the theoretical maximum for the time step in the EDEM simulated quasi-static particle set can be calculated as

$$T_R = \pi R \left(\frac{\rho}{G}\right)^{\frac{1}{2}} (0.1631\sigma + 0.8766)^{-1} \tag{3}$$

where R is the particle radius in mm; ρ, the particle density in g/cm^3; G, the shear modulus in Pa; and σ, Poisson's ratio.

In actual simulation operations, a percentage of the Rayleigh value is generally used for a fixed time step. In simulations where the number of contacts for a single particle is greater than 4, it is appropriate to choose a fixed time step of 0.2, which establishes a grid where the ideal side length of the grid element is twice the minimum particle radius of the simulation model, i.e., 2 mm. Therefore, the minimum radius of the simulation model established in this research was set at 2 mm. When the grid size is defined as twice the minimum radius of the model, the number of grid cells is large; thus, the grid size is set at 6.25 times the minimum radius. The total simulation duration defined according to the test requirements is 8 s. The relevant parameter settings in the simulation calculation process are listed in Table 1.

Table 3 Simulation process parameters

Project	Attribute value	Units
Rayleigh step size	3.42×10^{-4}	s
Fixed step size	6.84×10^{-5}	s
Target save interval	0.01	s
Total simulation time	8	s
Minimum radius of particles	2	mm
Grid size	12.5	mm
Number of grids	4056	

3.3 Single Factor Test

3.3.1 Simulation test of seed meter at different speeds

After the cottonseed and seed meter simulation model had been created, the physical parameters and contact parameters were set, as listed in Tables 2 and 3.

Table 2 Material properties for simulation model

Material	Poisson's ratio	Shear modulus (MPa)	Density (kg·m^{-3})
Seed	0.25	1.0×10^{10}	860
Wall	0.28	8.2×10^{10}	7890

Table 3 Material contact parameters of simulation model

Contact parameter	Collision recovery coefficient	Static friction factor	Rolling friction factor
Seed - Seed	0.30	0.56	0.15
Seed -wall	0.52	0.50	0.10

Wang used the working speed as the influencing factor and analyzed it with EDEM software to obtain the spoon performance [23]. Concurrently, the design of the spoon-wheel structure and the critical working speed determined in the previous study suggested that the working speed has a certain influence on the movement laws of cottonseeds and the seeding performance of the meter. In the present study, a single-factor simulation test for the rotational speed was established to explore the effects of different values on the performance of the metering device. During the simulation, the speed of the meter was set at 15, 20, 25, 30, 35, 40, 45, 50, and 55 r/min. The 0th to the 1st second constituted the seed generation time, after which the spoon-wheel and seeding wheel began to rotate.

3.3.2 Simulation Test of Seed Metering Device under Different Tilt angles

In a spoon-wheel type seed meter, a cottonseed can be cleaned by gravity. The meter has an inclination angle with respect to the ground that causes the seed to produce a force component in the gravitational direction, thereby affecting the cleaning process, as well as the movement laws of cottonseeds and seed-planting performance. Therefore, a single-factor simulation test of the tilt angle was constructed, in which the test was performed when the tilt angle was set at 0, 5, 10, 15, 20, 25, 30, 35, and 40° with a rotation speed of 40 r/min. The total simulation time was 8 seconds. The 0 to 1st second constituted the seed generation time, after which the spoon-wheel and the seeding wheel began to rotate.

4 Simulation Results and Analysis

4.1 Simulation analysis of cottonseed movement process

During the simulation, the cottonseeds were statically generated at the pellet factory and then entered the filling area with a falling process depicted in Figure 6. The spoon-wheel and seeding wheel began to rotate. The subsequent operation of the meter is illustrated in Figure 7. The different colors indicate the various seed speeds, and the arrows indicate the direction of the movement .

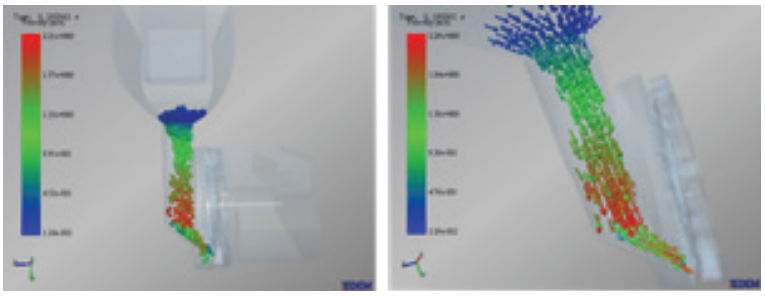

Figure 6 Schematic diagram of seed dropping process

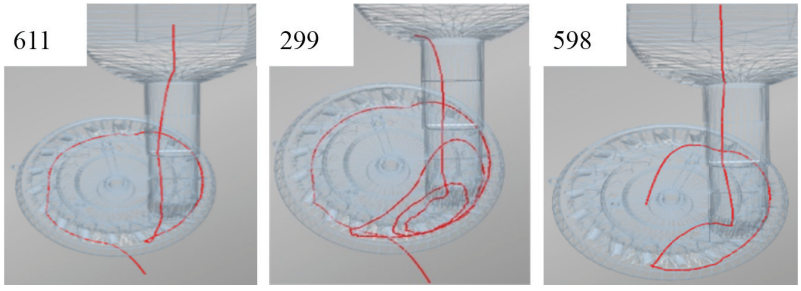

Figure 7 Schematic diagram for simulation process of seed metering device

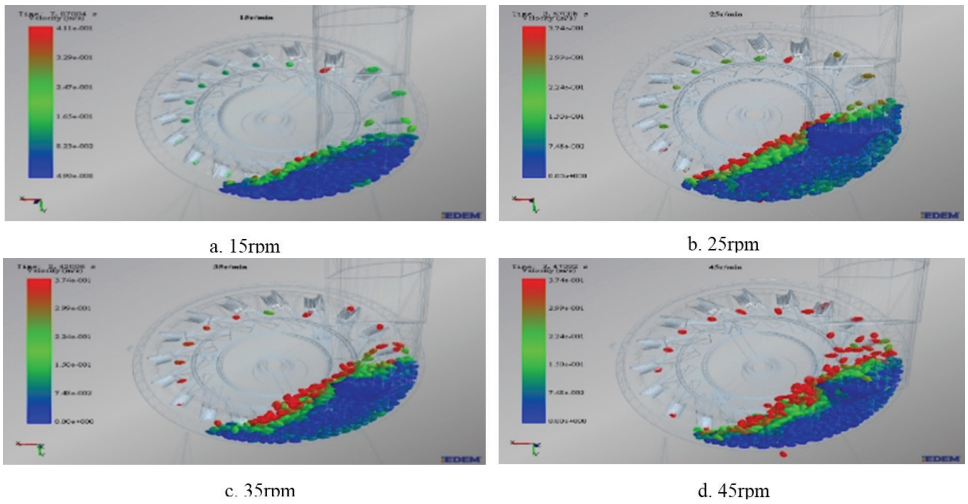

Figure 8 Sketch of seeds 611, 299, and 598 for grain metering device

As depicted in Figure 8, the cottonseed movement during the post-simulation processing module was set for a streamlined display, in which the movement trajectory of the single seed in the meter can be clearly observed. Figure 7 is a schematic diagram illustrating the movement trajectory of a single seed when the rotation speed of the meter is set at 45 r/min. Parts (a), (b), and (c) show the results for seed numbers 611, 299, and 598, respectively. During the operation of the metering device, model No. 611 had a shorter residence time in the filling area. The seed was picked up by the seeding wheel, after which process the grain entered the seeding port. After the seed was formed for No. 299, it was disturbed by the spoon-wheel in the filling area. After two rotational motions, it was picked up by the seeding wheel, followed by the movement of seed No. 611. After seed No. 598 was generated, it entered the filling area and was picked up by the seeding wheel. However, during the process, the seed failed to enter the wheel, thus causing the seed to be missed while the area was waiting for the next fill.

4.2 Effect of seed meter speed on seeding performance

During the simulation of the seed meter, higher rotation speeds caused the external force of the grain to change continuously. During the process of filling, clearing, delivering, and guiding seeds, collisions occurred between the metering device, the seed, and the wall, which caused missing and multiples during the operation of the device. The treatment and evaluation of the metering device are based on "Technical Conditions for a Single Grain (Precision) Planter" and GB/T 6973-2005 [24] "Test Method for a Single Grain (Precision) Planter," as listed in Table 4.

Table 4 Performance index of seed metering device at different rotational speeds

Rotational speed (rpm)	15	20	25	30	35	40	45	50	55
Acceptance index (%)	100	100	100	100	97.22	97.22	94.44	92.59	87.96
Multiples index (%)	0	0	0	0	0	0	0.93	1.85	2.78
Missing index (%)	0	0	0	0	2.78	2.78	4.63	5.56	9.26

Table 5 Performance index of seed metering device at different tilt angles

Simulation angle (°)	0	5	10	15	20	25	30	35	40
Acceptance index (%)	97.22	98.14	97.22	98.15	92.59	81.48	75	65.74	54.63
Multiples index (%)	0	0.93	0.93	1.85	7.41	18.52	25	34.26	45.37
Missing index (%)	2.78	0.93	1.85	0	0	0	0	0	0

The performance indicators for the precision seed metering device reveal the following three items: the grain distance qualified index *S*, the multiples index *D*[25], and the missing index *M*. These performance indexes are calculated as follows:

$$S = \frac{n_1}{N} \times 100\% \quad (4)$$

$$D = \frac{n_2}{N} \times 100\% \quad (5)$$

$$M = \frac{n_0}{N} \times 100\% \quad (6)$$

In the preceding formulas, n_0 is the number of air leaks; n_1, the single seed row number; n_2, the number of granules; and N, the number of theoretical rows.

During the simulation tests, a total of 108 grains of cotton were discharged under the theoretical condition of 6 times the circular motion. By using Formulas (4)–(6), the

grain distance acceptance index *S*, the multiples index *D*, and the missing index M of the seed meter are obtained at different rotational speeds. The results are listed in Table 4.

As indicated in Table 4, as the rotation speed increases, the metering index shows a downwards trend; thus, lower rotation speeds provide a better seed-metering effect. When the rotation speed is greater than or equal to 45 r/min, the multiples index increases with the rotation speed. If both are less than 2%, the performance requirements of the seed meter are met. When the rotation speed is less than 35 r/min, the missing index of the seed meter is 0, and the seeding effect is good. When the rotation speed is greater than 50 r/min, the missing index is significantly increased, and the work performance deteriorates.

In the actual working process of a spoon-wheel type seed meter with a certain structural form, a higher rotational speed leads to a greater seed volume per unit time. This improves the working efficiency of the metering device while simultaneously increasing both the multiples and missing indexes. After considering the various factors, the relative optimum speed of the seed meter was determined to be 50 r/min.

4.3 Influence of inclination angle of seed meter on seeding performance

Table 5 lists the simulation results for different inclination tilt angles for the seed meter. It is observed that as the inclination angle increases, both the acceptance and the missing indexes of the meter gradually decrease while the multiples index increases. When the inclination angle is less than 15°, the seed particle size acceptance index is maximized and fluctuates over a small range. When the meter speed is 50 r/min and the tilt angle is 0°, a leakage process occurs during the operation of the device, which leads directly to an occurrence of cavitation. Thus, proper re-play is beneficial to increase the seed germination rate. After considering the various factors, the relative optimum tilt angle of the metering device was determined to be 15°.

5 Test verification

The spoon-wheel type seeder test bench was built on the basis of the JPS-12 performance test benchmark. To verify the simulation results, the test material was selected from Shannongmian Cotton No. 11 cottonseeds with a smooth surface and no damage.

The distance required between cottonseeds is 10 cm. On the basis of the simulation tests, when the metering speed is 50 r/min and the tilt angle is 15°, the meter is operating at a relatively optimal level; thus, the relevant parameters of the test bench should be adjusted and tested. After the metering device operates under stable conditions for 30 seconds, the power supply can be shut off, after which the distance between the discharged grains is measured, and the coefficient of variation is calculated, as listed in Table 6.

Table 6 Test bench results from precision cotton-metering device

Seed bed speed (m/s)	Metering speed (r/min)	Tilting angles (°)	Multiples rate (%)	Missing rate (%)	Acceptant (%)	Mean spacing (cm)	Variation coefficient (%)
1.5	50	0	0.2	2.1	97.7	9.8	3.4
1.5	50	5	2.1	1.5	96.4	10.7	4.8
1.5	50	10	4.5	0.9	94.6	10.4	5.1
1.5	50	15	5.1	0.7	94.2	10.2	8.9

Figure 9 Test bench for precision cotton-metering device

When the belt speed of the seed bed is 1.5 m/s and the rotation speed of the seed meter is 50 r/min, the measured average grain distance is comparable to the specified grain distance. In this case, the coefficient of variation for the seed meter is small, indicating greater seed uniformity. When the tilt angle of the meter is 15°, the coefficient of variation for the grain distance of the seed meter is lower than the coefficient of variation at a tilt angle of 0°. This indicates that a tilt angle of 15° leads to an improved metering performance. The simulations provide results that are nearly the same as the experiments, thus indicating that the test bench is adequate.

In June 2019, a field trial was conducted on a prototype at the Agricultural Research Station on the South Campus of Shandong Agricultural University (Figure 10).

Figure 10 Field trial of precision cotton-metering

The drive of the planter was a 26 kW Revo 350 tractor, working in loamy soil with a moisture content of 23.2%. The instrumentation used in the tests mainly included cotton planters, rulers, stopwatches, moisture analyzers, and other related equipment. To measure the accuracy and convenience of the seed spacing, the sowing depth of the planter was adjusted to 0 at the time of sowing the seeds on the ground. Approximately 100 seed pitches were measured for each seeding length greater than 10 meters. The test results indicate that the machine can complete the relevant processes with a good seeding performance, during which single-seed precision sowing is realized with consistent spacing. The test results are listed in Table 7.

Table 7 Field trial results of precision cotton-metering

Sowing speed (m/s)	Tilting angle (°)	Multiples rate (%)	Missing rate (%)	Acceptance (%)	Mean spacing (cm)	Variation coefficient (%)
1.5	0	0.3	2.9	96.8	10.7	3.6
1.5	5	2.4	1.4	96.2	10.4	7.8
1.5	10	4.7	1.1	94.2	9.8	5.6
1.5	15	5.6	0.9	93.5	10.1	9.4

The field trial results for the reactions in Table 7 suggest that the replay and leakage rates are higher than the test bench results, but still meet a passing rate of more than 90%. The coefficient of variation for the grain distance is less than 10%, meaning it can be used for field sowing. The reasons that the replay and leakage rates as well as the coefficient of variation of the grain distance are higher than the results of the test bench are the vibrations and soil moisture of the field trials.

The design and simulation results of the seed metering device were verified by a bench test and field trial. The results of the bench test and field trial were categorized according to the grain distance qualified index and the coefficient of variation. The grain distance obtained in the seed-metering device test ranged from 94.2-97.7%; the coefficient of variation, from 3.4-8.9%. The grain distance obtained in the field trial ranged from 93.5-96.8%; the coefficient of variation, from 3.6-9.4%. Zhang D X et al. tested the distance qualified index and the coefficient of variation for a precision maize seed-metering device. They found that the qualified rate of the optimized device was greater than 93%. R.C. Singh et al. did some work on optimization of the design and operational parameters of a pneumatic seed-metering device for planting cottonseeds. Their metering system, with a speed of 0-42 m/s and a vacuum pressure of 2 kPa, produced superior results with a feed index of 94.7% and a coefficient of variation ranging from 6-8% [26-28].

6 Conclusion

(1) The width of the seeding spoon was determined to be 8 mm based on the 3D size of the cottonseed. The structure and working principles of the meter indicate that its radius was 119 mm, giving a total of 18 kinds of spoons. The critical speed was calculated to be 1.08 m/s.

(2) EDEM software was used to simulate the seeding process of the meter at different speeds and inclination angles. According to the tests, when the meter speed achieved 50 r/min and the tilt angle was 15°, the meter exhibited a relatively good working performance. In this case, the grain distance acceptance index was 92.59%; the multiples index, 1.85%; and the missing index, 5.56%.

(3) The seeding meter was tested on the bench and in the field. The test bench was considered for the meter through the PS-12 performance benchmark. For the simulation test bench, the seeding meter speed was 50 r/min; the tilt angle, 15°. At this time, the coefficient of variation for the spacing of the discharged cottonseeds in the metering device was 2.1%, the uniformity of which was high. The field trial results for the reactions indicated that the multiples and the missing rates were higher than in the test bench results but still met a passing rate of more than 90%. The coefficient of variation in the seed spacing was less than 10%, indicating that this design can be used for field sowing. This outcome suggests that the meter has a better working performance and is nearly consistent with the simulation results. Therefore, the test bench is considered to have a good seeding effect.

References

[1] Xu D. Research and Application of Wheat Precision Seeding Machinery[J]. Agricultural Science & Technology and Equipment, 2015(06):79-80.

[2] Wang J W, Tang H, Wang J F, et al. Analysis and Experiment of Guiding and Dropping Migratory Mechanism on Pickup Finger Precision Seed Metering Device for Corn[J]. Transactions of the Chinese Society for Agricultural Machinery, 2017,48(01):29-37.（in Chinese）

[3] Wang J Q, Wang G, Xin N, et al. Simulation Analysis of Working Process and Performance of Cell Wheel Metering Device[J]. Transactions of the Chinese Society for Agricultural Machinery, 2011,42(12):83-87.（in Chinese）

[4] Liang S Y, Feng J, Zeng A J, et al. Performance Experiments of the Seed-Meter Device With Combined Suckers[J]. Transactions of the Chinese Society of Agricultural Engineering, 2001,17(02):84-87.（in Chinese）

[5] Arzu Yazgi, Adnan Degirmencioglu. Optimisation of The Seed Spacing Uniformity Performance of a Vacuum-type

Precision Seeder Using Response Surface Methodology[J]. Biosystems Engineering, 2007,97(3):347-356.

[6] Wang Y, Wang F, Yin Y X, et al. Design of Spoon Type Seed Metering Device[J]. Journal of Anhui Agricultural Sciences, 2016,44(03):320-323. (in Chinese)

[7] Wang X Y, Wang J W, Tang H, et al. Improve Design and Experiment on Spoon of Spoon Precision Seed Metering Device [J]. Journal of Northeast Agricultural University, 2015, 46(12): 79-85.

[8] Han D D, Zhang D X, Jing H R , et al. DEM-CFD Coupling Simulation and Optimization of an Inside-filling Airblowing Maize Precision Seed-metering Device[J]. Computers and Electronics in Agriculture, 2018,150:426-438.

[9] Chen T, Zhai C N, Xing Z Z, et al. Discrete Element Simulation Study of Seed Metering Process of Inside-Filling Meter Based on EDEM[J]. Journal of Anhui Agricultural Sciences, 2016,44(16),250-253+278. (in Chinese)

[10] Zhang X, Vu-Quoc L. Simulation of chute flow of soybeans using an improved tangential force–displacement model[J]. Mechanics of Materials,2000,32(2):115-129.

[11] Momozu M, Oida A, Yamazaki M, et al. Simulation of a soil loosening process by means of the modified distinct element method[J]. Journal of Terramechanics,2002,39(4):207-220.

[12] Lei X L, Liao Y T, Liao Q X . Simulation of Seed Motion in Seed Feeding Device with DEM-CFD Coupling Approach for Rapeseed and Wheat [J]. Computers and Electronics in Agriculture,2016,131:29-39.

[13] van Liedekerke P, Tijskens E, Dintwa E, et al . DEM simulations of the particle flow on a centrifugal fertilizer spreader[J] . Powder Technology,2009,190(3):348-360.

[14] Dun G Q, Chen H T, Zha S H, et al. Parameter Optimization and Validation of Soybean Cell Wheel Seeding Plate Type-hole Based on EDEM[J]. Soybean Science,2016,35(05),830-839.

[15] Wang Y, Yang X, Wang J H, et al. Simulation for Performance to Seed Cotton with Spoon-type Based on Discrete Element Method[J]. Journal of Shandong Agricultural University(Natural Science Edition),2016,47(06),873-878. (in Chinese)

[16] Brosh, T., Kalman, H., Levy, A., Peyron, I., Ricard, F.. DEM-CFD simulation of particle comminution in jet-mill. Powder Technol. , 2014,257, 104–112.

[17] Yuan G Z, Zhang T, Liu Y Q, et al. Design of a Spoon Wheel Type Seed Metering Device and Simulation of Soybean Seeds By Discrete Elemen[J]. Journal of Agricultural Mechanization Research,2017,11:25-29.

[18] Liu T, He R Y, Lu J, et al. Simulation and verification on seeding performance of nest hole wheel seed-metering device based on [J].Journal of South China Agricultural University,2017,11:25-29.(in Chinese)

[19] Shi S, Zhang D X, Yang L, et al. Simulation and verification of seed-filling performance of pneumatic-combined holes maize precision [J].Transactions of the Chinese Society of Agricultural Engineering, 2015,31(3)：62-69. (in Chinese)

[20] Wang J W, Tang H, Wang Q, et al. Numerical simulation and experiment on seeding performance of pickup finger precision seed-metering device based on EDEM[J]. Transactions of the Chinese Society of Agricultural Engineering,2015,31(21)：43-50.(in Chinese)

[21] Cao X Y, Liao Y T, Cong J L, et al. Design and Experiment on Metering Hole Structure of Centrifugal Precision Metering Device for Rapeseed[J].Transactions of the Chinese Society for Agricultural Machinery,2014,45,(S1):40-46. (in Chinese)

[22] Kamgar S, Eslami MJ, Maharlouie MM. Design, development and evaluation of a mechatronic transmission system to improve the performance of a conventional row crop planter. Intl J Agron Plant Prod, 2013,4(3):480–7.

[23] Wang X Y, Wang J W, Tang H, et al. Improve design and experiment on spoon of spoon precision seed metering device[J].Journal of Northeast Agricultural University,2015,46(12):79-85.

[24] GB/T6973-2005 Single grain (precision) planter technical conditions. People's Republic of China machinery industry standard, 2005.(in Chinese)

[25] Shi L R , WuCJ M, Sun W, et al. Simulation test for metering process of horizontal disc precision metering device based on discrete [J].Transactions of the Chinese Society of Agricultural Engineering,2014,30(08):40-48. (in Chinese)

[26] R.C. Singh, G. Singh, D.C. Saraswat. Optimisation of design and operational parameters of a pneumatic seed metering device for planting cottonseeds [J]. Biosystems Engineering , 2005, 92 (4), 429–438.

[27]Yang, L., Yan, B.X., Cui, T., Yu, Y.M., He, X.T., Liu, Q.W., Liang, Z.J., Yin, X.W., Zhang,D.X.. Global overview of research progress and development of precision maize planters[J]. Int. J. Agri. Biol. Eng. , 2016, 9 (1), 9–26.

[28]Tong, Z.B., Zheng, B., Yang, R.Y., Yu, A.B., Chan, H.K.. CFD-DEM investigation of the dispersion mechanisms in commercial dry powder inhalers[J]. Powder Technol. , 2013,240, 19–24.

[29] Zhao, Y.Z., Ding, Y.l., Wu, C.N., Cheng, Y.. Numerical simulation ofhydrodynamics in downers using a CFD-DEM coupled approach[J]. Powder Technol. , 2010199, 2–12.

[30] Li, H.C., Li, Y.M., Gao, F., Zhao, Z., Xu, L.Z.. CFD-DEM simulation of material motion in the air-and-screen cleaning device[J]. Comput. Electr. Agri. , 2012b 88, 111–119.

Viser Technology Pte. Ltd.
Mechanical Engineering Science
doi: 10.33142/mes.v2i1.2616

Research Article Open Access

Simulation and Experimental Study on Load-bearing Deformation Characteristics of 11R22.5 Vehicle Retreaded Tire

Qiang WANG *, Li JIANG, Xiaojie QI

School of Automobile and Traffic Engineering, Heilongjiang Institute of Technology, Harbin, China

***Corresponding Author:** Qiang WANG , E-mail: 630702666@qq.com*

Abstract:
The finite element bearing deformation simulation was implemented on 11.00R22.5 retreaded tires by ANSYS software in the paper in order to further clarify the bearing deformation characteristics of retreaded tires and improve the performance of retreaded tires effectively. The characteristic laws of bearing radial deformation and bearing lateral deformation of retreaded tire and new tires of the same model under different working conditions were obtained through load deformation tests. The radial deformation calculation results, simulation results and measured results of retreaded tires were comparatively analyzed. The calculation formula of bearing radial deformation of retreaded tires was proposed based on the linear regression principle. The difference of bearing deformation characteristics and ground area characteristics of retreaded tires and new tires were comparatively analyzed. The results showed that the radial and lateral deformation of retreaded tires and new tires is increased with the increase of radial load when the tire pressure was constant, and the increase trend is approximately linear. The radial stiffness of retreaded tires is similar to that of new tires under certain tire pressure and low load. The radial stiffness of retreaded tires is larger than that of new tires, and the stiffness difference is increased with the increasing of load under constant tire pressure and high load. Rubber aging phenomenon in retreaded tire carcass have an impact on the bearing deformation characteristics of retreaded tires, thereby producing great impact on the remaining service life of retreaded tires.

Keywords: *vehicle retreaded tire; load-bearing deformation characteristics; finite element; radial stiffness; rubber aging*

1 Introduction

The tire industry has undergone rapid development with the rapid development of the automobile industry in China. China has become the largest tire production and consumption power all over the world. However, natural rubber resources are extremely scarce in China, and about 70% of the annual demand should be imported. Therefore, how to recycle, reduce and make waste tire harmless is related to environmental protection- an important social issue on the one hand, it also belongs to an important topic related to the sustainable development of national economy in China. The waste tires in China are recycled and mainly used to produce recycled rubber and rubber powder. The international practice of "refurbishing followed by scrapping" is usually adopted in order to maximize the effectiveness of waste tire utilization. About 30% of the economic use value of the whole tires is used only, and about 70% value can be reused by retreading when the tread is polished[1, 15, 17]. A tire can be retread for many times under sound use and maintenance. The service life of new tires equal to 60%~90% can be restored after each retreading. The total service life of the tire can be extended by 1~2 times by repeated retreading. The value of rubber and other resources consumed in the retreading of a waste tire is equivalent to 15%~30% of the production of a new tire, and the sales price is 20%~50% of that of new tires by comparison. Meanwhile, the excellent retreaded tire can even achieve similar mileage and security as that of a new tire. Therefore, we can make the best use of the usage value of tires from retreaded tires. The tire retreading industry can be developed with excellent social and economic benefit as well as great social sustainable development significance [14, 2, 11]. Truck vehicle tires are mostly used in professional transportation systems among various tires, which are characterized by heavy bearing and poor working environment. They are often driven in poor roads and bad environment, which are usually replaced once 1~2 years in batches mostly. Transportation enterprises can save huge cost if retreaded tires are used instead of new tires. However, tire retreading technology is weak in China. The truck tire refurbishment products have short service, thereby greatly limiting promotion and application thereof

in a wide range. It is necessary to study the performance of radial retreaded tires of trunks in order to improve the performance and service life of retreaded tires accordingly, thereby laying an important theoretical foundation for optimizing tire retreading process and improving retreaded tire performance [12, 13].

2 Finite element simulation of load-bearing deformation

The radial deformation cloud image of 11.00R22.5 retreaded tires is obtained by ANSYS finite element software as shown in figure 1. The lateral deformation cloud image is shown in figure 2. Figure 1 and figure 2 show that the tread of retreaded tires is in full contact with the surface of the ground target near the center of the tire ground mark when the load is 30kN and the tire pressure is 830kPa, the tread layer becomes flat, and the tire expands outwards laterally. The maximum radial deformation of retreaded tires is 23.72mm, and the maximum lateral deformation is 23.059mm. The radial deformation under different loads (15kN~35kN) and different tire pressures (530kPa~830kpa) is obtained as shown in figure 3, and the lateral deformation is shown in figure 4 through several simulations. Figure 3 and figure 4 show that the radial and lateral deformation of retreaded tires is increased with the increase of load when the tire pressure is constant, and the increase trend is approximately linear. The radial and lateral deformation of retreaded tire is increased with the decrease of tire pressure when the load is constant, and the increase trend is also approximately linear. The simulation value of retreaded tire radial deformation is compared with the calculated value when the tire pressure is 530kPa, 630kPa, 730kPa and 830kPa as shown in figure 5. Figure 5 shows that the simulation results thereof are constant with the theoretical calculation results under four different tire pressure conditions. The simulation values are slightly larger than the theoretical calculation values mainly because the finite element model has certain calculation accuracy error [7, 10].

3 Load-bearing deformation test

3.1Test purpose

The radial and lateral deformation of 11.00R22.5 retreaded tired and new tires of the same model under3.1.1 and3.1.2 working conditions were determined. The bearing deformation laws of retreaded tires and new tires were obtained. The differences thereof were compared. The accuracy of the finite element simulation analysis results was verified[4, 5, 8].

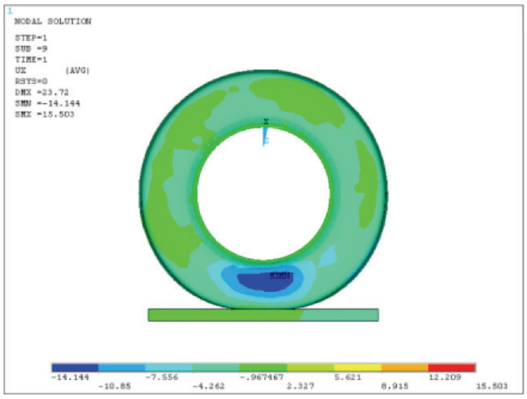

Figure 1 Radial Deformation Graph

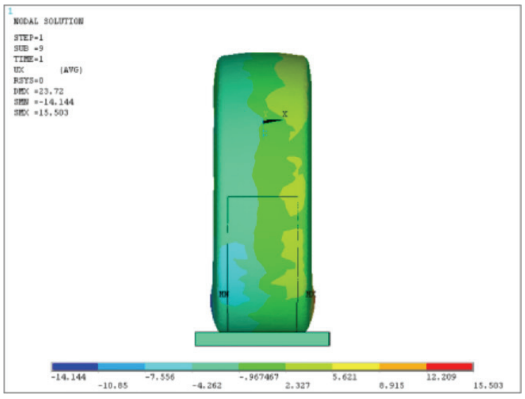

Figure 2 Lateral Deformation Graph

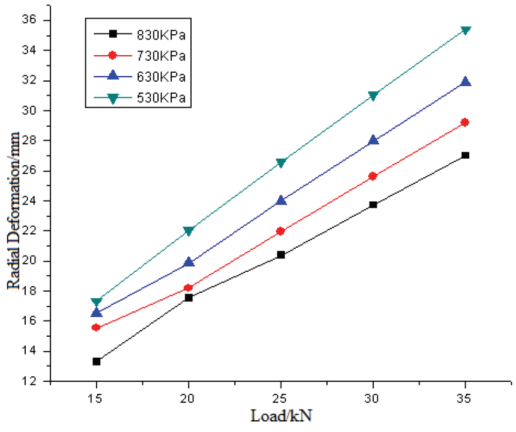

Figure 3 Radial Deformation under different working conditions

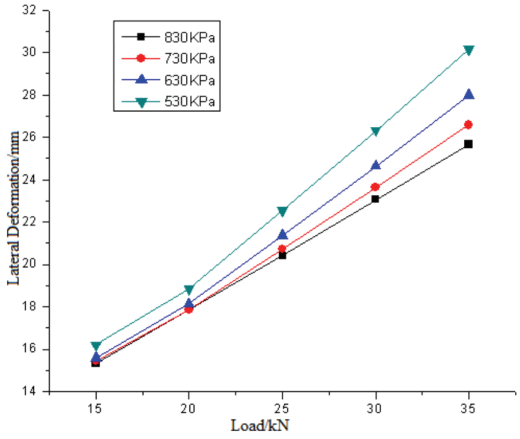

Figure 4 Lateral Deformation under Different Working Conditions

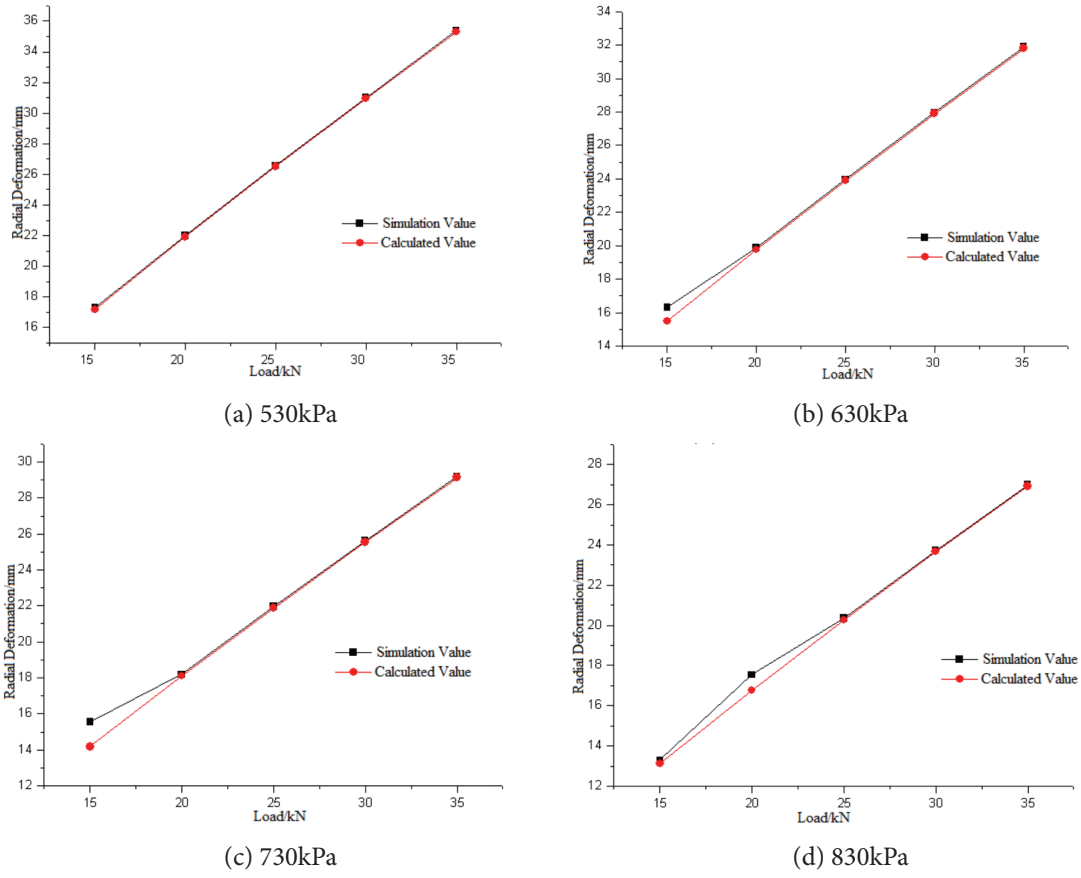

Figure 5 Comparison of Simulation Value and Calculated Value of Radial Deformation under Different Tire Pressures

3.1.1Constant tire pressure and load change

The tire pressure is set as 530kPa, 630kPa, 730kPa and 830kPa respectively. The load F1 is set as 15kN, 20kN, 25kN, 30kN and 35kN. The corresponding loading force F2 is 30kN, 40kN, 50kN, 60kN and 70kN.

3.1.2 Constant load and tire pressure change

The load F1 is set as 15kN, 20kN, 25kN, 30kN and 35kN respectively. The corresponding loading force F2 is 30kN, 40kN, 50kN, 60kN and 70kN. The tire pressure is set as 530kPa, 630kPa, 730kPa and 830kPa.

3.2 Test system

The load deformation measurement system of retreaded tires is shown in figure 6. The test

system is mainly composed of a loading system and a deformation measurement system. The test system belongs to a fore closed loop structure with smooth stress state. The loading force value accuracy error is less than 2%. The main equipment includes press, radial scale, lateral scale, plate, bracket, working platform, axle tube, tire gauge, air compressor, etc. Wherein, a professional production press with an indicating pressure gauge is mainly utilized in the loading system, which is loaded through the hydraulic cylinder manual lever. The loading force range is 0~30t. The deformation measurement system is mainly composed of a radial scale and

a lateral scale. The measuring accuracy is ±0.5mm [9, 16].

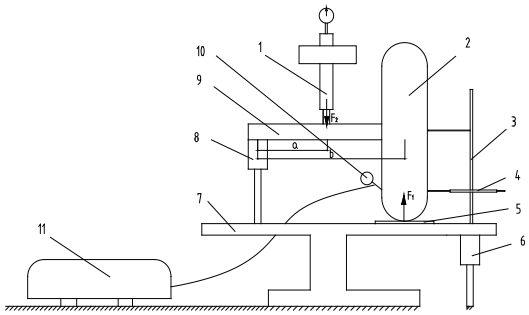

1-A Pressure Machine 2-Tested Tire 3-Radial Ruler 4-Lateral Ruler 5-flat 6-Bracket 1 7-Work Platform 8-Bracket 2 9-Axle Casing 10-Tire Pressure Gauge 11-Air Compressor

Figure 6 Load-bearing Deformation Test System

4 Results and analysis

The radial deformation and lateral deformation of retreaded tire under different working conditions is obtained by bearing deformation tests as shown in figure 7. The radial deformation and lateral deformation of new tire under different working conditions are obtained as shown in figure 8. Figure 7 and figure 8 show that the radial and lateral deformation of retreaded tires and new tires are increased with the increase of vertical load when the tire pressure is constant, and the increase trend is approximately linear.

It is consistent with the simulation results. The calculated value, simulation value and measured value of retreaded tire radial deformation are compared as shown in figure 9 when the tire pressure is constant. Figure 9 shows that the test values, simulation values and numerical values of retreaded tire radial and lateral deformation are constant well, and the error is less than 3%. The error is produced mainly because of certain precision errors between the loading system and the measurement system. The radial deformation test data are linearly regressed according to the test results, simulation results and numerical calculation results. The obtained linear equation of the radial deformation regression [3, 7] is shown in table 1.

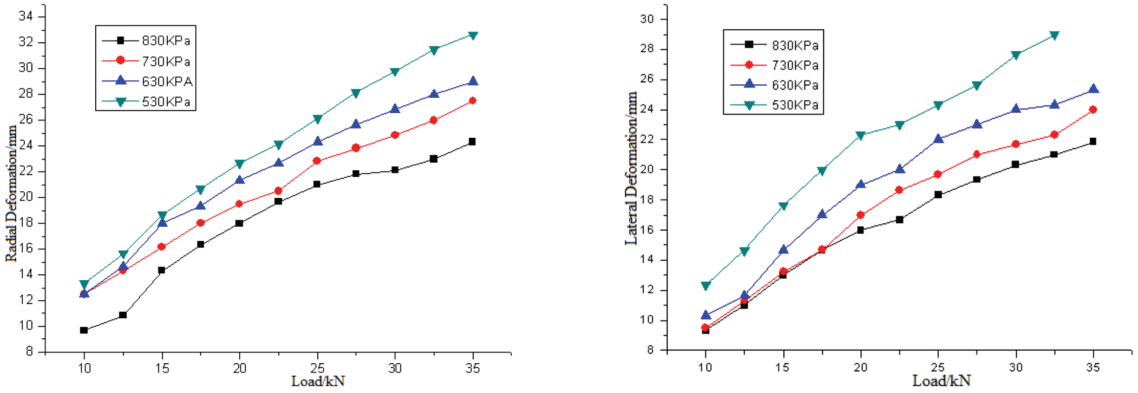

(a) Radial Deformation (b) Lateral Deformation

Figure 7 Deformation of Retreaded Tire under Different Conditions

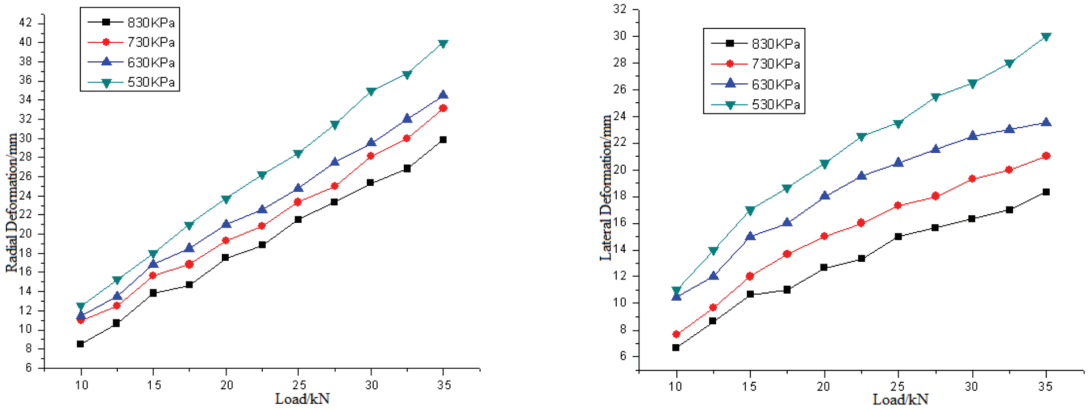

(a) Radial Deformation (b) Lateral Deformation

Figure 8 Deformation of New Tire under Different Conditions

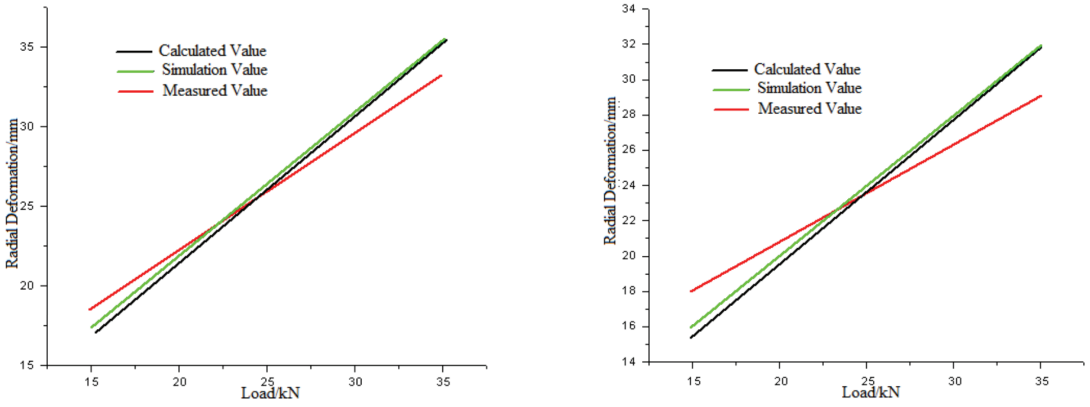

(a)530kPa (b)630kPa

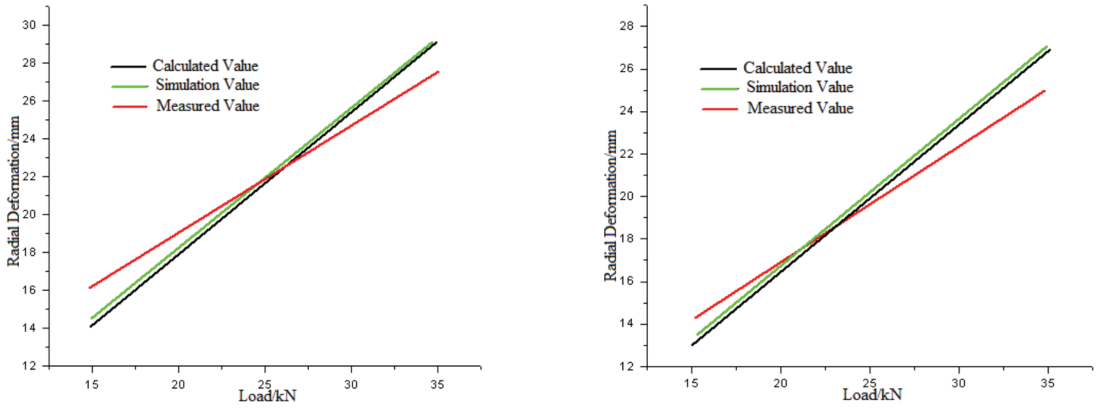

(c) 730kPa (d) 830kPa

Figure 9 Comparison of Calculated Value, Simulation Value and Measured Value of Retreaded Tire Radial Deformation

Table 1 Regression Equation of Radial Deformation

Tire Pressure(kPa)	Regression Equation
830	$\delta_1 = 1.21 + 8.36W$
730	$\delta_2 = 0.86 + 8.46W$
630	$\delta_3 = 0.59 + 8.76W$
530	$\delta_4 = 0.34 + 8.96W$

The principle of multiple linear regression of the least square method is utilized to propose the formula for calculating the radial deformation theory of 11.00R22.5 retreaded tire as shown in (2).

$$\delta = \mu \frac{W^{a_2}}{p_i^{a_1}} \tag{2}$$

The logarithm $\ln\delta=\ln\mu + \alpha_2 \ln W - \alpha_1 \ln p_i$ is obtained at both sides, the theoretical formula for calculating the radial deformation of 11.00R22.5 retreading radial tires is shown in (3).

$$\delta = 9.46\times10^{-3} \frac{W^{0.78}}{p_i^{0.467}} \tag{3}$$

The formula (3) can be used for calculating the radial deformation value of 11.00R22.5 retreaded radial tires under radial load. It can provide theoretical basis for the research on bearing deformation characteristics of 11.00R22.5 retreaded tires. Figure 10 and figure 11 respectively show the comparison curves of load radial deformation and ground area under different inflation pressures of 11.00R22.5 retreaded tires and new tire of the same brand and model. As can be seen from figure 10 and figure 11, the radial deformation and ground area characteristics of retreaded tire are consistent with that of new tire of the same brand and model, but there are some differences. The radial deformation and ground area change laws of new tires and retreaded tires are linearly regressed when the tire pressure is 830kPa. The radial deformation and ground area regression equations of retreaded tires and new tires are shown in table 2, and the regression comparison was shown in figure 12 and figure 13. Figure 12 and figure 13 show that the curve slope of retreaded tires is smaller than that of new tires when the tire pressure is constant. The radial deformation of retreaded tires is similar to that of new tires when the load is less than 20kN. Moreover, The difference thereof is larger and larger with the continuous increase of load. It is obvious that the radial stiffness of retreaded tires is larger than that of new tires when it is close to the standard load. The lateral deformation of retreaded tires is smaller than that of new tires when the tire pressure is constant. There is little difference between retreaded tires and new tires when the tire pressure is low. The difference is larger and larger when the tire pressure is gradually increased. The ground area of retreaded tires is smaller than that of new tires when the tire pressure is constant.The difference between retreaded tires and new tires is small when the load is small. The imprinted area of retreaded tires is increased with the increase of vertical load when the tire pressure, lateral force and camber angle used in the test are zero. The imprinted area of retreaded tires is increased with the increase of vertical load. The tire will be approximately elliptic in contact with the ground for the entire width when the vertical load is increased to a certain value. The vertical load is increased continuously, the tire imprint width remains constant, the imprint length is increased, the imprint area is increased, and the imprint is approximately rectangular. The imprint law of new tires is consistent with that of retreaded tires, but the imprinted area of retreaded tires is smaller than that of new tires under the same working condition [6].

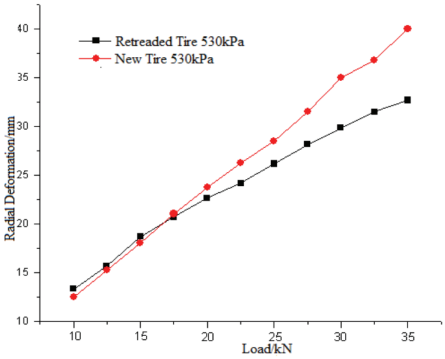

(a)530kPa

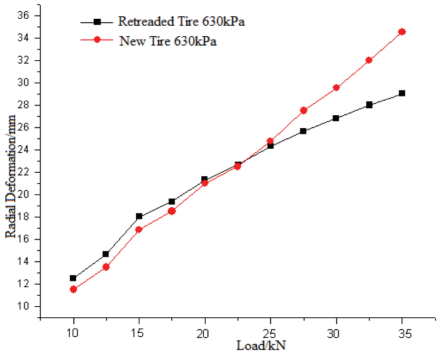

(b) 630kPa

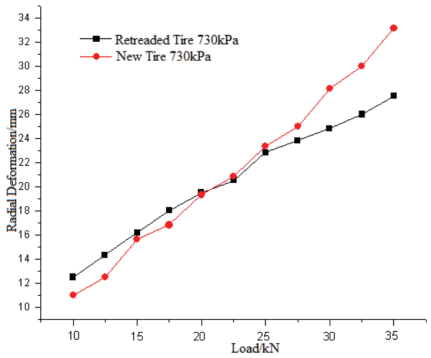

(c) 730kPa

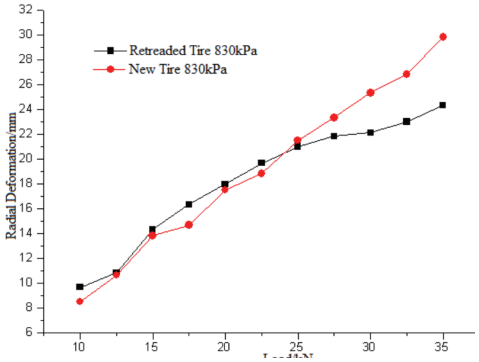

(d) 830kPa

Figure 10 Radial Deformation Contrast of Retreaded Tire with New Tire

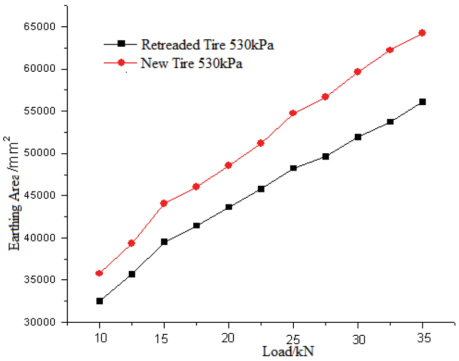

(a)530kPa

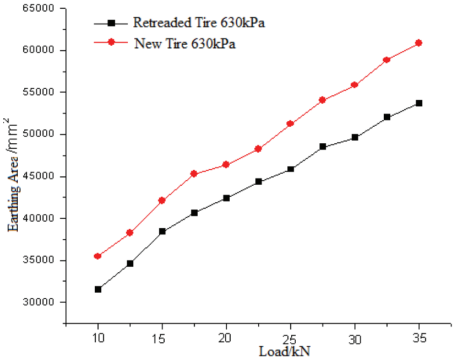

(b)630kPa

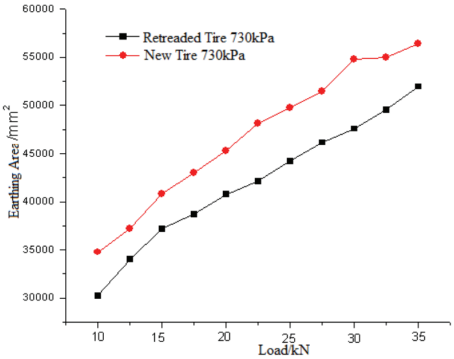

(c)730kPa

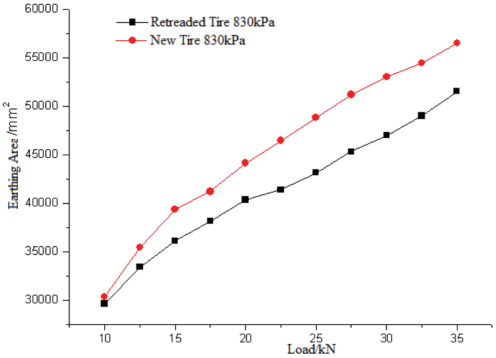

(d)830kPa

Figure 11 Earthing Area Contrast of Retreaded Tire with New Tire

Table 2 Radial Deformation and Earthing Area Regression Equations of Retreaded Tire with New Tire

	Radial Deformation	Earthing Area
Retreaded Tire	$\delta_1 = 4.18 + 6.38W$	$S_1 = -7856 + 9.67W$
New Tire	$\delta_2 = 1.52 + 10.24W$	$S_2 = 2338 + 12.24W$

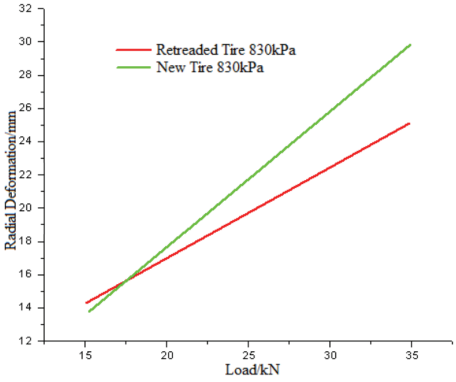

Figure 12 Radial Deformation Regression Contrast of Retreaded Tire with New Tire

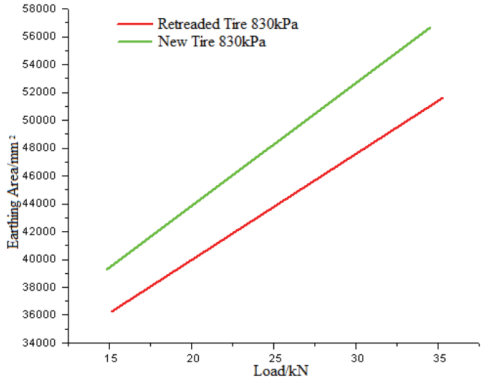

Figure 13 Earthing Area Regression Contrast of Retreaded Tire with New Tire

5 Main conclusions

The radial and lateral deformation of retreaded tires and new tires is increased with the increase of radial load when the tire pressure is constant, and the increase trend is approximately linear. Retreaded tire carcass suffers from certain rubber aging. The overall elastic modulus of the carcass thereof is larger than that of new tires. The waste tire rubber elastic modulus is increased with the increase of aging time according to approximate linear law. The inflation pressure and the steel cord layer in the carcass mainly support the tires during low load, and steel cord is less affected by the aging degree. Therefore, radial stiffness difference is not significant between retreaded tires and new tires. The inflation pressure and carcass steel cord/rubber composite integrity mainly support the tires when the value is close to the standard load (30kN). The elastic modulus of retreaded tires is increased due to aging, and its radial stiffness is greater than that of new tires. Moreover, the radial deformation difference between retreaded tires and new tires is increased with the increase of the load. The research method in the paper also can be used for predicting the aging degree of retreaded tire carcass rubber accordingly. Namely the ground area difference is larger if the radial deformation difference between retreaded tires and new tires is larger under near-standard load. The retreaded tire carcass rubber has higher aging degree if the lateral deformation difference between retreaded tires and new tires is lager when the value is close to the standard inflation pressure, and the remaining service life of retreaded tires is shorter.

Author Contributions: Qiang WANG (1981-), Male, Associate professor, Ph.D., Postdoctoral, Master's Supervisor. The main research direction is vehicle tire technology, automobile product optimization design and analysis. E-mail: 630702666@qq.com; Li JIANG, Female, born in 1981, Associate professor, Ph.D., The main research direction is vehicle tire technology.

Acknowledgments: This study was supported by Basic Scientific Research Operating Expense Funding Project of Provincial Univeristies in Heilongjiang Province (2018CX07); Heilongjiang Institute of Engineering Ph. D. Fund. (2016BJ02).

References

[1] Behnke R, Wollny I, Hartung F, et al(2019). Thermo-mechanical finite element prediction of the structural long-term response of asphalt pavements subjected to periodic traffic load: Tire-pavement interaction and rutting. Computers and Structures218.

[2] Cui L(2019). Performance Characteristics and Quality Inspection of Retreaded Tire Products. Comprehensive Utilization of Tire Resources in China (12): 41-48.

[3] Liu D(2016). Tire Innovation Leads the Future of Low Carbon and Energy Saving. Modern Rubber Technology42 (02): 9-14.

[4] Mehdi R, Mir Hamid Reza G, Ghasem N(2019). Computer simulation of tire rolling resistance using finite element method: Effect of linear and nonlinear viscoelastic models. Proceedings of the Institution of Mechanical Engineers, Part D: Journal of Automobile Engineering233(11).

[5] Payam F,Abdollah G,Ahmad S Malvajerd,et al(2019). Finite element modeling of the interaction of a treaded tire with clay-loam soil. Computers and Electronics in Agriculture162.

[6] Qi X, Wang Q, Yu J(2010). Load Bearing Deformation Characteristics of Retreaded Tires. Journal of Transportation Engineering10 (05): 47-56.

[7] Qi X(2010). Load Bearing Simulation and Failure Mechanism Research of Retreaded Heavy Vehicle Tire. Harbin: Northeast Forestry University.
[8] Ravivat R,Chakrit S(2019). Proper Radial Spokes of Non-Pneumatic Tire for Vertical Load Supporting by Finite Element Analysis. International Journal of Automotive Technology20(4).
[9] Seongrae K, Hanseok P, Byungwoo M, et al(2018). The prediction methodology for tire's high speed durability regulation test using a finite element method. International Journal of Fatigue118.
[10] Wu J, Chen L, Wang Y,et al(2019). Effect of temperature on wear performance of aircraft tire tread rubber. Polymer Testing79.
[11] Wang Q, Jiao S(2018). Load Bearing Deformation Characteristics of Retreaded tires for Engineering Vehicles. Journal of China Highway31 (05): 191-198.
[12] Wang Q, Qi X, Wang Y(2018). Research on Deformation Characteristics of Engineering Retreaded Tire under Free Inflation and Free Rotation Conditions . Journal of Hubei University of Automotive Industry32 (02): 17-21,26.
[13] Wang Q(2015). Study on Mechanical Properties and Performance Reinforcement Mechanism of Retreaded tires. Harbin: Northeast Forestry University.
[14] Wang Y(2018). Major Problems to Be Solved in The Field of Tire Retreading. Comprehensive Utilization of Tire Resources in China (07): 35.
[15] Xiao J(2017). Tire Retreading and Remanufacturing Technology. Comprehensive Utilization of Tire Resources in China (01): 26-28.
[16] Zhang Y, Gao J, Li Q(2019). Study on tire-ice traction using a combined neural network and secondary development finite element modeling method. Concurrency and Computation: Practice and Experience31(9).
[17] Zhong J(2016). Necessity Analysis of Quality Monitoring of Retreaded Tire Products. China New Technology and New Products(11): 161.

Viser Technology Pte. Ltd.
Mechanical Engineering Science
doi: 10.33142/mes.v2i1.2617

Research Article Open Access

Modeling size-dependent behaviors of axially functionally graded Bernoulli-Euler micro-beam

Shuai WANG, Zetian KANG, Shichen ZHOU, Bo ZHOU*, Shifeng XUE

College of Pipeline and Civil Engineering, China University of Petroleum (East China), Qingdao 266580, P. R. China

***Corresponding Author:** Bo ZHOU, Email: zhoubo@upc.edu.cn*

Abstract:
This work focus on the mechanical behaviors, which are related to the size effect, functionally graded (FG) effect and Poisson effect, of an axially functionally graded (AFG) micro-beam whose elastic modulus varies according to sinusoidal law along its axial direction. The displacement field of the AFG micro-beam is set according to the Bernoulli-Euler beam theory. Employing the modified couple stress theory (MCST), the components of strain, curvature, stress and couple stress are expressed by the second derivative of the deflection of the AFG micro-beam. A size-dependent model related to FG effect and Poisson effect, which includes the formulations of bending stiffness, deflection, normal stress and couple stress, is developed to predict the mechanical behaviors of the AFG micro-beam by employing the principle of minimum potential energy. The mechanical behaviors of a simply supported AFG micro-beam are numerically investigated using the developed model for demonstrating the size effects, FG effects and Poisson effects of the AFG micro-beam. Results show that the mechanical behaviors of AFG micro-beams are distinctly size-dependent only when the ratio of micro-beam height to material length-scale parameter is small enough. The FG parameter is an important factor that determines and regulates the size-dependent behaviors of AFG micro-beams. The influences of Poisson's ratio on the mechanical behaviors of AFG micro-beams are not negligible, and should be also considered in the design and analysis of an AFG micro-beam. This work supplies a theoretical basis and a technical reference for the design and analysis of AFG micro-beams in the related regions.

Keywords: *axially functionally graded micro-beam; size-dependent behaviors; size effect; functionally graded effect; Poisson effect*

1 Introduction

Functionally graded (FG) materials are a new group of non-homogeneous materials and have some desirable performances to satisfy special features in engineering design [34]. By proper design, they can not only eliminate the stress concentration, reduce the residual stress, but also reduce crack driving force to improve the strength of structural members. In the last decade, they are commonly used in applications of construction, aerospace, energy absorption or even in biomedical sectors [26]. Many theoretical researches on the macroscopical characteristics of FG materials have been carried out based on the classical continuum mechanics [6, 21, 22].

With the rapid development of micro-technologies, FG materials have been broadly applied in micro-electro-mechanical system (MEMS) and nano-electro-mechanical system (NEMS). Micro-scale experiments [13-14] have revealed the size-dependent properties of micro-structures, which is called size effect [33]. The classical continuum theory fails to express the size effects of microstructures. Therefore, several higher-order continuum mechanics theories, such as strain gradient theories, couple stress theory and nonlocal elasticity theory, have been proposed to capture the size effects in microstructures [28]. In the couple stress theory, the size effects of microstructures are interpreted by two material length-scale parameters. The modified couple stress theory (MCST), which contains one material length-scale parameter, has been proposed by Yang et al. (2002)[32] and widely used to investigate the size-dependent bending, vibration, dynamic and buckling behaviors of the microstructures made of homogeneous materials [2-4, 12, 17-18, 20].

In recent years, the mechanical behaviors of transverse functionally graded (TFG) micro-beams/plates, whose material properties vary along the thickness direction, have been investigated on the basis of MCST. Asghari et al. (2010)[1] investigated the size effects of static bending deflection and natural frequency of a TFG cantilever micro-beam using the Bernoulli-Euler beam theory and Hamilton's principle. Reddy (2011)[23] developed nonlinear Bernoulli-Euler and Timoshenko micro-beam theories,

which can consider the Poisson effect and the von Kármán geometric nonlinearity, to study the size effects and FG effects of bending deflection, natural frequency and buckling of a simply supported TFG micro-beam based on the principle of virtual displacements. Ke et al. (2011, 2012a, 2012b)[9-11] investigated the size effects and FG effects of bending, free vibration and buckling characteristics of TFG composite micro-beams/plates with different boundary conditions using the Hamilton's principle. Salamat-Talab et al. (2012)[24] analyzed the size effects, FG effects and Poisson effects of the deflection, rotation and natural frequencies of a simply supported TFG micro-beam utilizing a third-order shear deformation beam theory, Hamilton's principle and series method. Thai et al. (2015)[27] studied the size effects and FG effects of the normal stress, transverse shear stress, deflection and frequency of a simply supported TFG sandwich Timoshenko micro-beam based on the Hamilton's principle and Mori-Tanaka scheme. And then, considering the Poisson effect, Trinh et al. (2016)[29] used a unified beam theory to explore the influences of the material length-scale parameter, FG parameter and slenderness ratio on the deflection, stresses, natural frequencies and critical buckling loads of a simply supported TFG micro-beam.

In addition to these TFG micro-beams/plates aforementioned, axially functionally graded (AFG) micro-beams, whose material properties vary along the longitudinal direction, have also been investigated[7, 25, 30]. For instance, Ghayesh et al. (2017)[5] examined the size effects of the nonlinear bending and forced vibrations of an AFG Bernoulli-Euler tapered micro-beam, and the influences of FG parameter and taper ratio on the deflection and frequency based on the MCST, Hamilton's principle, Galerkin method and Newton-Raphson technique. Li et al. (2017)[16] studied the size effects and FG effects of the bending, bucking and free vibration of an AFG Bernoulli-Euler micro-beam using the nonlocal strain gradient theory, the Hamilton's principle and generalized differential quadrature method. Karamanlı and Vo (2018)[8] investigated the size-dependent flexural behavior of a bi-directional FG micro-beam based on the MCST and the principle of minimum potential energy for several boundary conditions.

All of size effect, FG effect and Poisson effect play important roles in governing the mechanical behaviors of both TFG and AFG micro-beams. However few work have been published to investigate all of size effects, FG effects and Poisson effects of an AFG micro-beam comprehensively. The objective of this paper is to develop the mechanical model of an AFG micro-beam, which is related to the size effects, FG effects and Poisson effects. Firstly the displacement field of an AFG micro-beam is set according to the Bernoulli-Euler beam theory, and the components of strain, curvature, stress and couple stress are expressed by the deflection of the AFG micro-beam in Section 2. And then an AFG micro-beam model, which includes the size-dependent formulations of bending stiffness, deflection, stress and couple stress of the AFG micro-beam, is established by employing the principle of minimum potential energy in Section 3. Subsequently the size effects, the FG effects and the Poisson effects of the AFG micro-beam are respectively investigated in Section 4, Section 5 and Section 6 based on the developed model. Finally the important conclusions related to the size-dependent behaviors of an AFG micro-beam are summarized in section 7.

2 MCST descriptions of basic variables

According to the MCST, a generic matter point in an elastomer has 6 degrees of freedom, including 3 displacement components expressed by the vector u_i and 3 rotation components expressed by the vector θ_i, respectively. The differential relationship between displacement vector and rotation vector reads as

$$\theta_i = \frac{1}{2} e_{ijk} u_{k,j} \tag{1}$$

where e_{ijk} is the permutation symbol. The geometric equations of an elastomer read as

$$\varepsilon_{ij} = \frac{1}{2}(u_{i,j} + u_{j,i}) \tag{2a}$$

$$\chi_{ij} = \frac{1}{2}(\theta_{i,j} + \theta_{j,i}) \tag{2b}$$

where ε_{ij} and χ_{ij} denote the strain tensor and curvature tensor, respectively. For the case of small deformation, we write the constitutive equations of an isotropic elastomer as

$$\sigma_{ij} = \lambda \varepsilon_{kk} \delta_{ij} + 2G\varepsilon_{ij} \tag{3a}$$

$$m_{ij} = 2l^2 G \chi_{ij} \tag{3b}$$

where σ_{ij} is the stress tensor, m_{ij} is the deviatoric part of couple stress tensor, which is shortly called as the couple stress tensor in this paper, l is called as the material length-scale parameter, which is a material constant characterizing the size effect, λ and G represent Lame's coefficients expressed as

$$\lambda = \frac{E\mu}{(1+\mu)(1-2\mu)} \tag{4a}$$

$$G = \frac{E}{2(1+\mu)} \tag{4b}$$

with E and μ being the elastic modulus and Poisson's ratio, respectively.

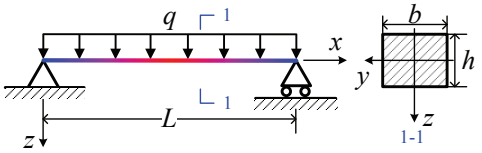

Figure 1 Simply supported AFG micro-beam subjected to uniformly distributed load under a rectangular coordinate system.

Figure 1 plots a simply supported AFG micro-beam with rectangular constant section subjected to the uniformly distributed load under a rectangular coordinate system. The length, width and thickness are respectively presented by L, b and h. Its elastic modulus is assumed to vary along the axial direction according to

$$E(x)=E_0+(E_1-E_0)\sin\frac{\pi x}{L} \tag{5}$$

where E_0 and E_1 stand for the values of elastic modulus in the left end and the middle cross-section of the micro-beam, respectively. According to the Bernoulli-Euler beam theory, we can express the displacement field of the AFG micro-beam as

$$u=-z\frac{\mathrm{d}w}{\mathrm{d}x},\ v=0,\ w=w(x) \tag{6}$$

where u, v and w are the displacement components in the x-, y- and z- directions, respectively. The displacement component in z-direction, w, is often called as the deflection of beam. Substituting the displacement field Eq. (6), into the geometric equation Eq. (2a), we formulate the strain components of the AFG micro-beam as

$$\varepsilon_x=-z\frac{\mathrm{d}^2w}{\mathrm{d}x^2},\ \varepsilon_y=\varepsilon_z=0$$
$$\varepsilon_{xy}=\varepsilon_{yx}=\varepsilon_{zx}=0 \tag{7}$$

Substituting the displacement field Eq. (6) into the rotation components Eq. (1), we formulate the rotation components of the AFG micro-beam as

$$\theta_y=-\frac{\mathrm{d}w}{\mathrm{d}x},\ \theta_x=\theta_z=0 \tag{8}$$

Plugging the rotation components Eq. (8) into the geometric equation Eq. (2b), we formulate the curvature components of the AFG micro-beam as

$$\chi_{xx}=\chi_{yy}=\chi_{zz}=0,$$
$$\chi_{xy}=\chi_{yx}=-\frac{1}{2}\frac{\mathrm{d}^2w}{\mathrm{d}x^2},\ \chi_{xz}=0 \tag{9}$$

Plugging the strain components Eq. (7) into the constitutive equation Eq. (3a), we formulate the stress components of the AFG micro-beam as

$$\sigma_{xx}=-[\lambda(x)+2G(x)]z\frac{\mathrm{d}^2w}{\mathrm{d}x^2},$$
$$\sigma_{zz}=\sigma_{yy}=-\lambda(x)z\frac{\mathrm{d}^2w}{\mathrm{d}x^2},$$
$$\sigma_{xy}=\sigma_{yz}=\sigma_{zx}=0 \tag{10}$$

where the coefficients λ(x) and G(x) can be determined by Eqs. (5) and (4). Plugging the curvature components Eq. (9) into the constitutive equation Eq. (3b), we formulate the couple stress components of the AFG micro-beam as

$$m_{xx}=m_{yy}=m_{zz}=0,$$
$$m_{xy}=m_{yx}=-G(x)l^2\frac{\mathrm{d}^2w}{\mathrm{d}x^2} \tag{11}$$

3 AFG micro-beam model

3.1 Bending stiffness formulation

According to the MCST, we can calculate the strain energy of an elastomer by

$$U=\frac{1}{2}\int_V(\sigma_{ij}\varepsilon_{ij}+m_{ij}\chi_{ij})\mathrm{d}V \tag{12}$$

where V is the volume the elastomer occupying. Inserting the strain Eq. (7), curvature Eq. (9), stress Eq. (10) and couple stress Eq. (11) into the strain energy Eq. (12), we obtain

$$U=\frac{1}{2}\int_L K(x)\left(\frac{\mathrm{d}^2w}{\mathrm{d}x^2}\right)^2\mathrm{d}x \tag{13}$$

where

$$K(x)=\alpha\left[E_0+(E_1-E_0)\sin\frac{\pi x}{L}\right]I \tag{14}$$

is the bending stiffness of the AFG micro-beam, where

$$I=\int_A z^2\mathrm{d}A \tag{15}$$

is the inertia moment of the cross-section of the micro-beam, and

$$\alpha=\frac{(1-\mu)}{(1-2\mu)(1+\mu)}+\frac{l^2A}{2(1+\mu)I} \tag{16}$$

is called as the size effect parameter of the AFG micro-beam because it is related to the material length-scale parameter l. For an AFG micro-beam with rectangular cross-section, we express the size effect parameter as

$$\alpha=\frac{1-\mu}{(1+\mu)(1-2\mu)}+\left(\frac{l}{h}\right)^2\frac{6}{(1+\mu)} \tag{17}$$

In order to express the size effect of the bending stiffness of the AFG micro-beam, we define a dimensionless bending stiffness as

$$K'(x)=\frac{K(x)}{E_0I} \tag{18}$$

Inserting Eq. (14) into Eq. (18), we formulate the dimensionless bending stiffness of the AFG micro-beam as

$$K'(x)=\alpha\left[1+(e-1)\sin\frac{\pi x}{L}\right] \tag{19}$$

where

$$e=\frac{E_1}{E_0} \tag{20}$$

is called as the FG parameter of the AFG micro-beam.

3.2 Deflection formulation

According to the displacement boundary conditions of the AFG micro-beam in Figure 1, we assume the deflection formulation as

$$w(x)=C_1\sin\left(\frac{\pi x}{L}\right)+C_2\sin\left(\frac{3\pi x}{L}\right) \tag{21}$$

where C_1 and C_2 are the undetermined coefficients. The total potential energy of the AFG micro-beam reads as

$$\Pi=U+V \tag{22}$$

where U is the strain energy formulated by Eq. (13), and

$$V=-\int_0^L q\cdot w(x)dx \tag{23}$$

is the loaded potential energy.

Plugging the strain energy Eq. (13), loaded potential energy Eq. (23) and deflection formulation Eq. (21) into the total potential energy Eq. (22), we express the total potential energy of the AFG micro-beam in Figure 1 as

$$\Pi(C_1,C_2)=\frac{\alpha E_0I\pi^3}{L^3}\left\{\left[\frac{\pi}{4}+\frac{2(e-1)}{3}\right]C_1^2-\frac{12(e-1)}{5}C_1C_2+\left[\frac{81\pi}{4}+\frac{1458(e-1)}{35}\right]C_2^2\right\}$$
$$-qC_1\frac{2L}{\pi}-qC_2\frac{2L}{3\pi} \tag{24}$$

According to the principle of minimum total potential

energy, the actual displacement field minimizes the total potential energy of an elastomer. Hence, the first order variation of the total potential energy expressed by Eq. (24) should be zero, i.e.

$$\delta\Pi(C_1, C_2)=\frac{\partial\Pi}{\partial C_1}\delta C_1+\frac{\partial\Pi}{\partial C_2}\delta C_2=0 \tag{25}$$

Eq. (25) should be identical for arbitrary δC_1 and δC_2, which asks for

$$\frac{\partial\Pi}{\partial C_1}=0 \tag{26a}$$

$$\frac{\partial\Pi}{\partial C_2}=0 \tag{26b}$$

Substituting the expression of total potential energy Eq. (24) into Eqs. (26a) and (26b), we obtain an algebraic equation set. Solving the obtained algebraic equation set, we have

$$C_1=\frac{2qL^4}{3\pi^4E_0I\alpha}\cdot\frac{a_2+3a_3}{a_1a_3-a_2^2} \tag{27a}$$

$$C_2=\frac{2qL^4}{3\pi^4E_0I\alpha}\cdot\frac{a_1+3a_2}{a_1a_3-a_2^2} \tag{27b}$$

where

$$a_1=\frac{3\pi+8(e-1)}{6} \tag{28a}$$

$$a_2=\frac{12(e-1)}{5} \tag{28b}$$

$$a_3=\frac{2835\pi+5832(e-1)}{70} \tag{28c}$$

Substituting Eq. (27) into the deflection formulation Eq. (21), we obtain

$$w(x)=\frac{2qL^4}{3\pi^4E_0I\alpha}\cdot\left[\frac{a_2+3a_3}{a_1a_3-a_2^2}\cdot\sin\frac{\pi x}{L}+\frac{a_1+3a_2}{a_1a_3-a_2^2}\cdot\sin\frac{3\pi x}{L}\right] \tag{29}$$

In order to express the size effect of the deflection of an AFG micro-beam, we define a dimensionless deflection as

$$w'(x)=w(x)/(\frac{2qL^4}{3\pi^4E_0I}) \tag{30}$$

Substituting Eq. (29) into Eq. (30),we formulate the dimensionless deflection of the AFG micro-beam in Figure 1 as

$$w'(x)=\frac{1}{\alpha}\cdot\left[\frac{a_2+3a_3}{a_1a_3-a_2^2}\cdot\sin(\frac{\pi x}{L})+\frac{a_1+3a_2}{a_1a_3-a_2^2}\cdot\sin(\frac{3\pi x}{L})\right] \tag{31}$$

3.3 Normal stress formulation

Plugging the deflection formulation Eq. (29) into the stress expression Eq. (10), we formulate the normal stress in a generic matter point of the AFG micro-beam cross-section as

$$\sigma_{xx}=\frac{2qL^2z}{3\pi^2I}\cdot\frac{E'(x)}{\alpha}\cdot\left(\frac{a_2+3a_3}{a_1a_3-a_2^2}\cdot\sin\frac{\pi x}{L}+\frac{9a_1+27a_2}{a_1a_3-a_2^2}\cdot\sin\frac{3\pi x}{L}\right) \tag{32}$$

where

$$E'(x)=\frac{1-\mu}{(1+\mu)(1-2\mu)}\left[1+(e-1)\sin\frac{\pi x}{L}\right] \tag{33}$$

In order to analyze the size effect of the normal stress of an AFG micro-beam, we define a dimensionless normal stress as

$$\sigma'_{xx}=\sigma_{xx}/(\frac{2qL^2z_{\max}}{3\pi^2I}) \tag{34}$$

Substituting Eq. (32) into Eq. (34), we formulate the dimensionless normal stress of the AFG micro-beam in Figure 1 as

$$\sigma'_{xx}=\frac{E'(x)}{\alpha}\cdot\left(\frac{a_2+3a_3}{a_1a_3-a_2^2}\cdot\sin\frac{\pi x}{L}+\frac{9a_1+27a_2}{a_1a_3-a_2^2}\cdot\sin\frac{3\pi x}{L}\right)\cdot\frac{z}{z_{mzx}} \tag{35}$$

3.4 Couple stress formulation

Plugging the deflection formulation Eq. (29) into the couple stress expression Eq. (11), we formulate the couple stress in a generic point of the AFG micro-beam cross-section as

$$m_{xy}=\frac{2qL^2h^2}{3\pi^2I}\cdot\frac{G'(x)}{\alpha}\cdot(\frac{l}{h})^2\cdot\left[\frac{a_2+3a_3}{a_1a_3-a_2^2}\cdot\sin\frac{\pi x}{L}+\frac{9a_1+27a_2}{a_1a_3-a_2^2}\cdot\sin\frac{3\pi x}{L}\right] \tag{36}$$

where

$$G'(x)=\frac{1}{2(1+\mu)}\left[1+(e-1)\sin\frac{\pi x}{L}\right] \tag{37}$$

In order to analyze the size effect of the couple stress of the AFG micro-beam, we define a dimensionless couple stress as

$$m'_{xy}=m_{xy}/(\frac{2qL^2h^2}{3\pi^2I}) \tag{38}$$

Substituting Eq. (36) into Eq. (38), we formulate the dimensionless couple stress of the AFG micro-beam as

$$m'_{xy}=\frac{G'(x)}{\alpha}\cdot(\frac{l}{h})^2\cdot\left[\frac{a_2+3a_3}{a_1a_3-a_2^2}\cdot\sin\frac{\pi x}{L}+\frac{9a_1+27a_2}{a_1a_3-a_2^2}\cdot\sin\frac{3\pi x}{L}\right] \tag{39}$$

4. Size effects of AFG micro-beam

4.1 Size effect of bending stiffness

The size effect of bending stiffness of the AFG micro-beam in Figure 1 are numerically investigated in this section. Figure 2 plots the bending stiffness curves related to size effect, where the dimensionless bending stiffness is calculated by Eq. (19) and maximum dimensionless bending stiffness is specified by Eq. (19) with x = L/2, respectively.

Figure 2(a) plots the dimensionless bending stiffness curves versus dimensionless coordinate with respect to different values of dimensionless height. It is clear that each dimensionless bending stiffness curve of the AFG micro-beam forms a sinusoidal hump whose peak declines with the increased value of dimensionless height. This indicates the size effect of bending stiffness that the smaller the value of dimensionless height is, the larger the value of dimensionless bending stiffness of the AFG micro-beam is.

Figure 2(b) shows the maximum dimensionless bending stiffness curves versus dimensionless height with respect to different values of FG parameter. It is found that the value of maximum dimensionless bending stiffness rapidly decreases with the increased value of dimensionless height when the dimensionless height is less than 4, however it gradually becomes a stable constant when the value of dimensionless height is greater than 10. This explains the size effect of bending stiffness that it is obvious when the value of dimensionless height is less than 4, while it can be neglected when the value of dimensionless height

is greater than 10. It is seen that the curve of maximum dimensionless bending stiffness moves upward and extends vertically when the FG parameter becomes larger. This explains the influence of FG parameter on the size effect of bending stiffness that the larger the value of FG parameter is, the more obvious the size effect of bending stiffness is.

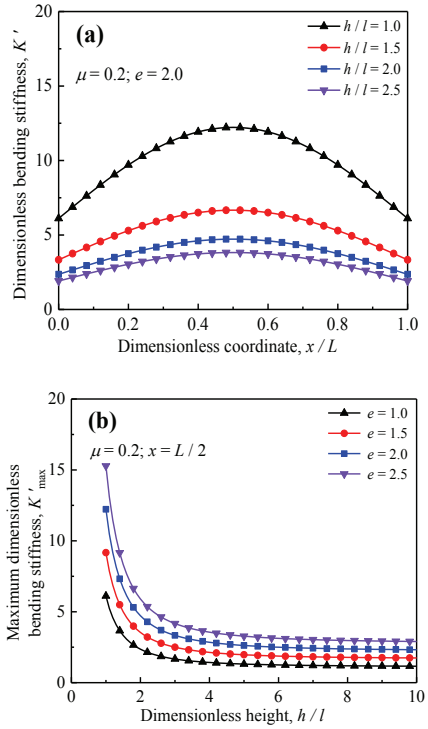

Figure 2 Bending stiffness curves related to the size effect: (a) dimensionless bending stiffness vs. dimensionless coordinate with different value of dimensionless height, and (b) maximum dimensionless bending stiffness vs. dimensionless height with different value of FG parameter.

4.2 Size effect of deflection

The size effect of deflection of the AFG micro-beam in Figure 1 is numerically investigated in this section. Figure 3 plots the deflection curves related to the size effect, where the dimensionless deflection is calculated by Eq. (31) and maximum dimensionless deflection is specified by Eq. (31) with x = L/2, respectively.

Figure 3 (a) plots the dimensionless deflection curves versus dimensionless coordinate with respect to different values of dimensionless height. It is clear that each dimensionless deflection curve of the AFG micro-beam forms a different sinusoidal hump whose peak rises with the increased dimensionless height. This indicates the size effect of deflection that the bending flexibility of an AFG micro-beam rises with the increased value of dimensionless height.

Figure 3 (b) shows the maximum dimensionless deflection curves versus dimensionless height with respect to different values of FG parameter. It is found that the value of maximum dimensionless deflection obviously increases with the increased value of dimensionless height when the value of dimensionless height is less than 4, however it gradually becomes a stable constant when the value of dimensionless height is greater than 10. This illustrates the size effect of deflection that it is obvious when the value of dimensionless height is less than 4, however it can be neglected when the value of dimensionless height is greater than 10. It is clear that the curve of maximum dimensionless deflection moves downward and shrinks vertically when the FG parameter becomes larger. This explains the influence of FG parameter on the size effect of deflection that the smaller the value of FG parameter is, the more obvious the size effect of deflection of an AFG micro-beam is.

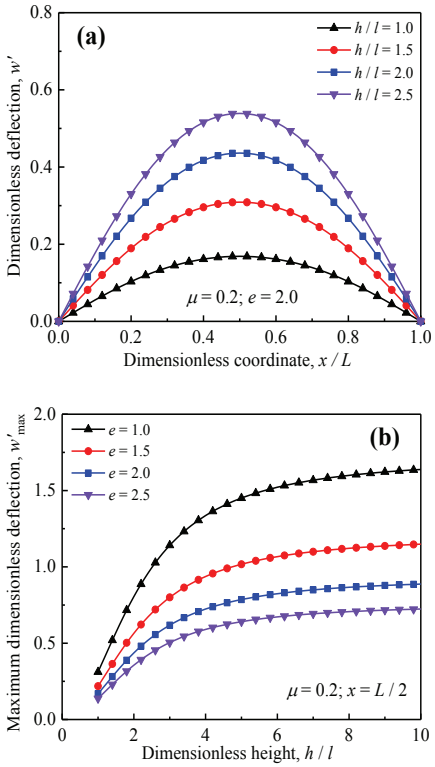

Figure 3 Deflection curves related to the size effect: (a) dimensionless deflection vs. dimensionless coordinate with different value of dimensionless height, and (b) maximum dimensionless deflection vs. dimensionless height with different value of FG parameter.

4.3 Size effect of normal stress

The size effect of normal stress of the AFG micro-beam in Figure 1 is numerically investigated in this section. Figure 4 plots the normal stress curves related to the size effect, where the dimensionless normal stress is calculated by Eq. (35) with z = h/2 and maximum dimensionless normal stress is specified by Eq. (35) with z = h/2 and x = L/2, respectively.

Figure 4(a) shows the dimensionless normal stress curves versus dimensionless coordinate with respect to different values of dimensionless height. It is clear that each dimensionless normal stress curve is with a platform

which is due to the FG effect of an AFG micro-beam. The altitude of platform of dimensionless normal stress rises with the increased value of dimensionless height, which explains the size effect of normal stress that the larger the value of dimensionless height is, the larger the value of dimensionless normal stress is.

Figure 4(b) plots the maximum dimensionless normal stress curves versus dimensionless height with respect to different values of FG parameter. It is found that the value of maximum dimensionless normal stress nonlinearly increases with the increased value of dimensionless height when the value of dimensionless height is below 10, however it gradually becomes a stable constant when the value of dimensionless height is above 20. This indicates that the size effect of normal stress of an AFG micro-beam is obvious when the value of dimensionless height is below 10, however it can be neglected when the value of dimensionless height is above 20. It is seen that the influence of FG parameter on the size effect of normal stress is not very obvious.

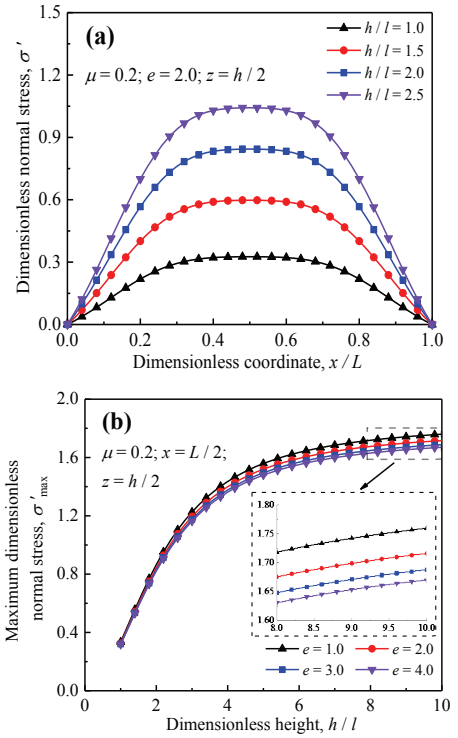

Figure 4 Normal stress curves related to the size effect: (a) dimensionless normal stress vs. dimensionless coordinate with different value of dimensionless height, and (b) the maximum dimensionless normal stress vs. dimensionless height with different value of FG parameter.

4.4 Size effect of couple stress

The size effect of couple stress of the AFG micro-beam in Figure 1 is numerically investigated in this section. Figure 5 plots the couple stress curves related to the size effect, where the dimensionless couple stress is calculated by Eq. (39) and maximum dimensionless couple stress is specified by Eq. (39) with x = L/2, respectively.

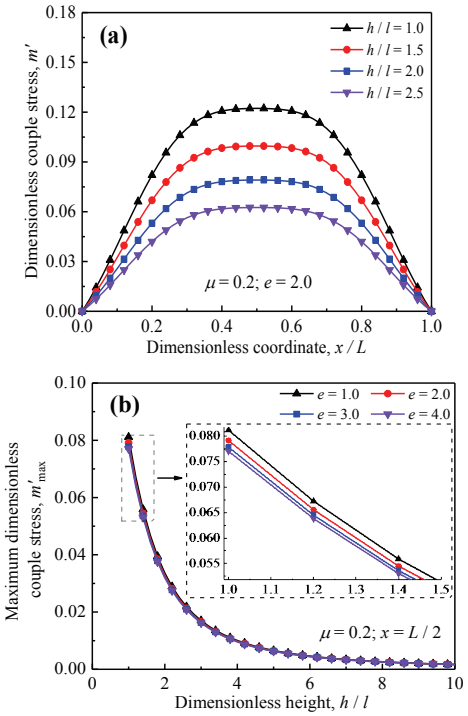

Figure 5 Couple stress curves related to the size effect: (a) dimensionless couple stress vs. dimensionless coordinate with different value of dimensionless height, and (b) maximum dimensionless couple stress vs. dimensionless height with different value of FG parameter.

Figure 5(a) shows the dimensionless couple stress curves versus dimensionless coordinate with different values of dimensionless height. It is also clear that each dimensionless couple stress curve is with a platform due to the FG effect of an AFG micro-beam. But the altitude of platform of dimensionless normal stress declines with the increased value of dimensionless height, which indicates the size effect of couple stress of an AFG micro-beam that the smaller the value of dimensionless height is, the larger the value of dimensionless couple stress is.

Figure 5(b) shows the maximum dimensionless couple stress curves versus dimensionless height with different values of FG parameter. It is seen that the value of maximum dimensionless couple stress rapidly decreases with the increased value of dimensionless height when the value of dimensionless height is below 5, however it gradually becomes a stable constant when the value of dimensionless height is above 10. This indicates the size effect of couple stress of an AFG micro-beam that it is obvious when the value of dimensionless height is below 5, while it can be neglected when the value of dimensionless height is above 10. It is also seen that the influences of FG parameter on the size effect of couple stress of an AFG micro-beam is not obvious.

5 FG effects of AFG micro-beam

5.1 FG effect of bending stiffness

The FG effect of bending stiffness of the AFG micro-beam in

Figure 1 is numerically investigated in this section. Figure 6 shows the bending stiffness curves related to the FG effect, where the dimensionless bending stiffness is calculated by Eq. (19) and maximum dimensionless bending stiffness is specified by Eq. (19) with x = L/2, respectively.

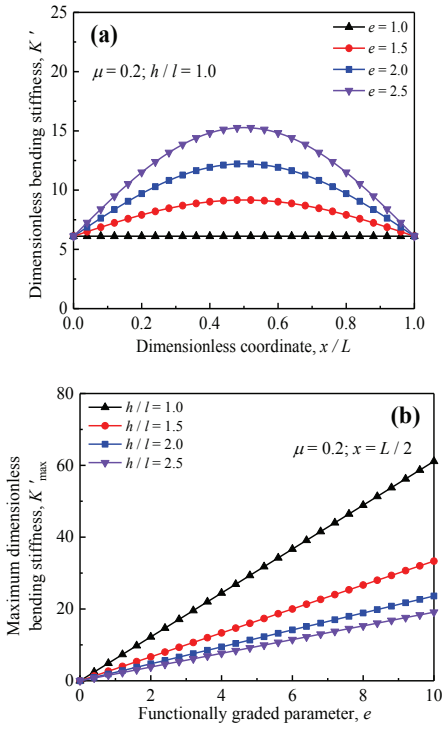

Figure 6 Bending stiffness curves related to the FG effect: (a) dimensionless bending stiffness vs. dimensionless coordinate with different value of FG parameter, and (b) dimensionless bending stiffness vs. FG parameter with different value of dimensionless height.

Figure 6(a) plots the dimensionless bending stiffness curves versus dimensionless coordinate with respect to different values of FG parameter. It is clear that the peak of dimensionless bending stiffness curve rises with the increased value of FG parameter, which is due to the expression of elastic modulus Eq. (5), and the definition of FG parameter Eq. (20). This illustrates the FG effect of bending stiffness of an AFG micro-beam that the bending stiffness increases with the increased value of FG parameter.

Figure 6(b) plots the maximum dimensionless bending stiffness curves versus FG parameter with respect to different values of dimensionless height. It is clear that the value of maximum dimensionless bending stiffness increases with the increased value of FG parameter, which also indicates FG effect of bending stiffness of an AFG micro-beam. It is found that the curve of maximum dimensionless bending stiffness extends vertically with the decreased value of dimensionless height, which indicates the influence of dimensionless height on the FG effect of bending stiffness that the smaller the value of dimensionless height is, the more obvious the FG effect of an AFG micro-beam is.

5.2 FG effect of deflection

The FG effect of deflection of the AFG micro-beam in Figure 1 is numerically investigated in this section. Figure 7 shows the deflection curves related to the FG effect, where the dimensionless deflection is calculated by Eq. (31) and maximum dimensionless deflection is specified by Eq. (31) with x = L/2, respectively.

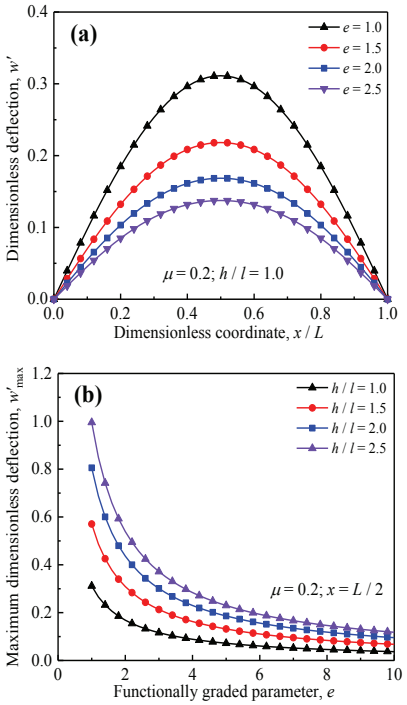

Figure 7 Deflection curves related to the FG effect of deflection: (a) dimensionless deflection vs. dimensionless coordinate with different value of FG parameter, and (b) maximum dimensionless deflection vs. FG parameter with different value of dimensionless height.

Figure 7(a) shows the dimensionless deflection curves versus dimensionless coordinate with respect to different values of FG parameter. It is clear that the peak of sinusoidal curve of dimensionless deflection decreases with the increased value of FG parameter. This illustrates the FG effect of deflection that the bending flexibility of an AFG micro-beam decreases with the increased value of FG parameter.

Figure 7(b) plots the maximum dimensionless deflection curves versus FG parameter with respect to different values of dimensionless height. It is found that the value of maximum dimensionless deflection rapidly decreases with the increased value of FG parameter when the FG parameter is below 5, however it gradually becomes a stable constant when the FG parameter is above 10. This means that the FG effect of deflection of an AFG micro-beam is obvious when the FG parameter is below 5, while it can be neglected when the FG parameter is above 10. It is clear that the maximum dimensionless deflection curve moves upward and extends vertically when the dimensionless height becomes larger. This explains the

influence of dimensionless height on the FG effect of deflection of an AFG micro-beam that the larger the value of dimensionless height is, the more obvious the FG effect is.

5.3 FG effect of normal stress

The FG effect of normal stress of the AFG micro-beam in Figure 1 is numerically investigated in this section. Figure 8 plots the normal stress curves related to the FG effect, where the dimensionless normal stress is calculated by Eq. (35) with z = h/2 and maximum dimensionless normal stress is specified by Eq. (35) with z = h/2 and x = L/2, respectively.

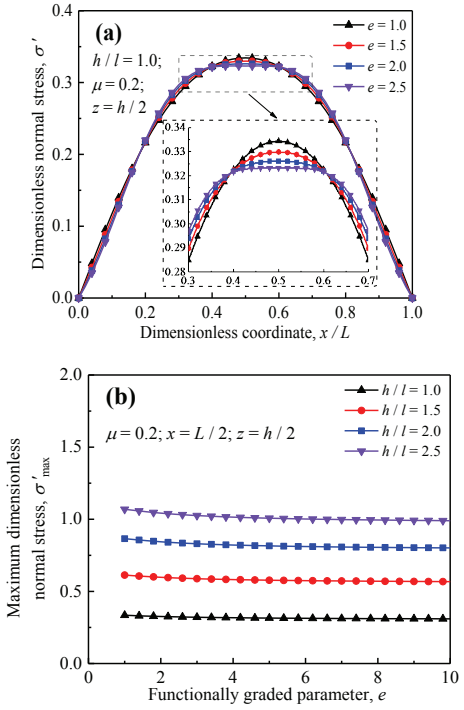

Figure 8 Normal stress curves related to the FG effect: (a) dimensionless normal stress vs. dimensionless coordinate with different value of FG parameter, and (b) maximum dimensionless normal stress vs. FG parameter with different value of dimensionless height.

Figure 8(a) shows the dimensionless normal stress curves versus dimensionless coordinate with respect to different values of FG parameter. It is found that the curve peak of dimensionless normal stress decreases with the increased value of FG parameter. However the curves of dimensionless normal stress for different FG parameters are very close and similar, which indicates that the FG effect of normal stress of an AFG micro-beam is not obvious.

Figure 8(b) plots the maximum dimensionless normal stress curves versus FG parameter with respect to different values of dimensionless height. It is clear that the value of maximum dimensionless normal stress has only slight decrease with the increased value of FG parameter, which also means that the FG effect of normal stress of an AFG micro-beam is not obvious. It is seen that the maximum dimensionless normal stress curve moves upward and becomes more declining with the increased value of dimensionless height. This explains that the larger the value of dimensionless height is, the more obvious the FG effect of normal stress of an AFG micro-beam is.

5.4 FG effect of couple stress

The FG effect of couple stress of the AFG micro-beam in Figure 1 is numerically investigated in this section. Figure 9 plots the couple stress curves related to the FG effect, where the dimensionless couple stress is calculated by Eq. (39) and maximum dimensionless couple stress is specified by Eq. (39) with x = L/2, respectively.

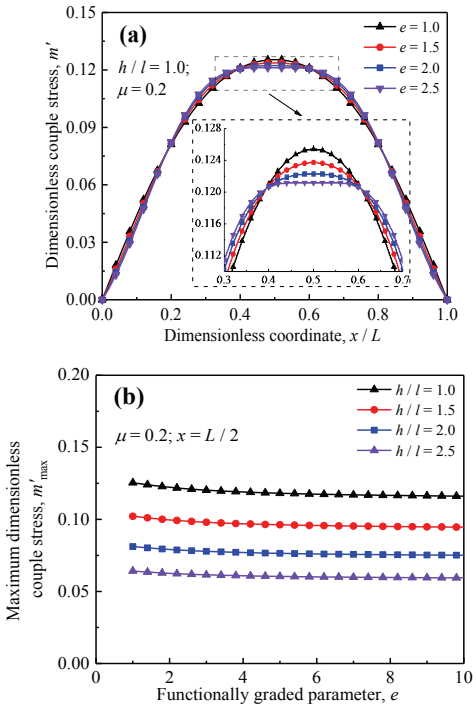

Figure 9 Couple stress curves related to the FG effect: (a) dimensionless couple stress vs. dimensionless coordinate with different value of FG parameter, and (b) maximum dimensionless couple stress vs. FG parameter with different value of dimensionless height.

Figure 9(a) plots the dimensionless couple stress curves versus dimensionless coordinate with respect to the different values of FG parameter. It is found that the curve peak of dimensionless couple stress decreases with the increased value of FG parameter. However the curves of dimensionless couple stress for the different values of FG parameter are very close and similar, which indicates that the FG effect of couple stress of an AFG micro-beam is also not obvious.

Figure 9(b) shows the maximum dimensionless couple stress curves versus FG parameter with respect to different values of dimensionless height. It is found that the value of maximum dimensionless couple stress has only slight decrease with the increased value of FG parameter, which also means that the FG effect of couple stress of an AFG micro-beam is not obvious. It is clear that the maximum dimensionless couple stress curve moves upward and becomes more declining with the decreased

dimensionless height. This explains that the smaller the value of dimensionless height is, the more obvious the FG effect of couple stress of an AFG micro-beam is.

6 Poisson effects of AFG micro-beam

6.1 Poisson effect of bending stiffness

The Poisson effect of bending stiffness of the AFG micro-beam in Figure 1 is numerically investigated in this section. Figure 10 shows the bending stiffness curves related to the Poisson effect, where the dimensionless bending stiffness is calculated by Eq. (19) and maximum dimensionless bending stiffness is specified by Eq. (19) with x = h/2, respectively.

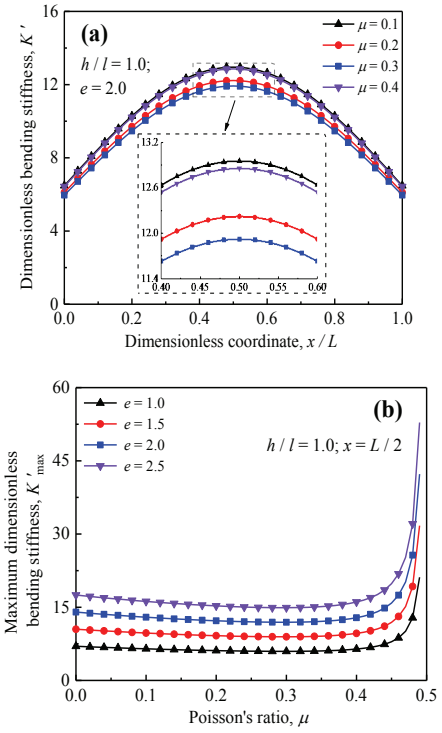

Figure 10 Bending stiffness curves related to the Poisson effect: (a) dimensionless bending stiffness vs. dimensionless coordinate with different value of Poisson's ratio, and (b) maximum dimensionless bending stiffness vs. Poisson's ratio with different value of FG parameter.

Figure 10(a) plots the dimensionless bending stiffness curves versus dimensionless coordinate with respect to different values of Poisson's ratio. It is clear that each dimensionless bending stiffness curve is with a sinusoidal shape. The Poisson's ratio has an obvious influence on the curve of dimensionless bending stiffness of an AFG micro-beam, which is the Poisson effect of bending stiffness.

Figure 10(b) shows the maximum dimensionless bending stiffness curves versus Poisson's ratio with respect to different values of FG parameter. It is seen that the value of maximum dimensionless bending stiffness slightly decreases with the increased value of Poisson's ratio when the value of Poisson's ration is below 0.4, however it rapidly increases with the increased value of Poisson's ratio when the value of Poisson's ration is above 0.4. This indicates that the Poisson effect of bending stiffness is obvious when the value of Poisson's ration is above 0.4, while it can be neglected when the value of Poisson's ration is below 0.4. It is seen that the maximum dimensionless bending stiffness curve moves upward and extends vertically when the value of FG parameter becomes larger. This explains the influence of FG parameter on the Poisson effect of bending stiffness that the larger the value of FG parameter is, the more obvious the Poisson effect of bending stiffness of an AFG micro-beam is.

6.2 Poisson effect of deflection

The Poisson effect of deflection of the AFG micro-beam in Figure 1 is numerically investigated in this section. Figure 11 shows the deflection curves related to the Poisson effect, where the dimensionless deflection is calculated by Eq. (31) and maximum dimensionless deflection is specified by Eq. (31) with x = L/2, respectively.

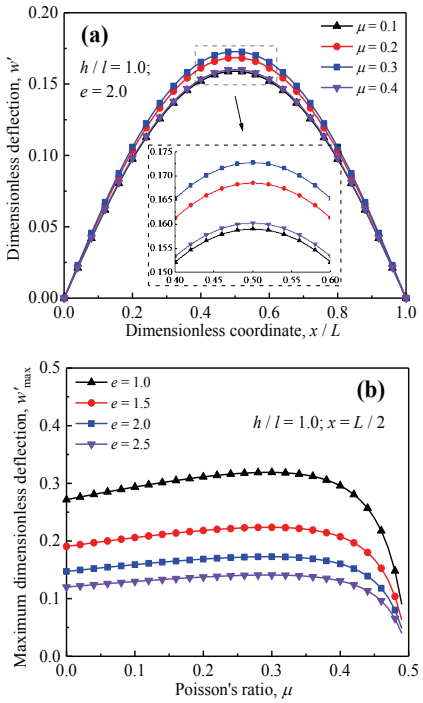

Figure 11 Deflection curves related to the Poisson effect: (a) dimensionless deflection vs. dimensionless coordinate with different value of Poisson's ratio, and (b) maximum dimensionless deflection vs. Poisson's ratio with different value of FG parameter.

Figure 11(a) plots the dimensionless deflection curves versus dimensionless coordinate with respect to different values of Poisson's ratio. It is found that each dimensionless deflection curve is with a sinusoidal shape and the Poisson's ratio has an obvious influence on the curve of dimensionless deflection, which is the Poisson effect of deflection of an AFG micro-beam.

Figure 11(b) shows the maximum dimensionless deflection curves versus Poisson's ratio with respect to different values of FG parameter. It is clear that the value

of maximum dimensionless deflection slightly increases with the increased value of Poisson's ratio when the value of Poisson's ratio is below 0.4, however it rapidly decreases with the increased value of Poisson's ratio when the value of Poisson's ratio is above 0.4. This indicates that the Poisson effect of deflection of an AFG micro-beam is obvious when the value of Poisson's ratio is above 0.4, while it can be neglected when the value of Poisson's ratio is below 0.4. It is seen that the maximum dimensionless deflection curve moves downward and shrinks vertically with the increased value of FG parameter. This explains the influence of FG parameter on the Poisson effect of deflection that the smaller the value of FG parameter is, the more obvious the Poisson effect of deflection of an AFG micro-beam is.

6.3 Poisson effect of normal stress

The Poisson effect of normal stress of the AFG micro-beam in Figure 1 is numerically investigated in this section. Figure 12 shows the normal stress curves related to the Poisson effect, where the dimensionless normal stress is calculated by Eq. (35) with z = h/2 and the maximum dimensionless normal stress is specified by Eq. (35) with z = h/2 and x = L/2, respectively.

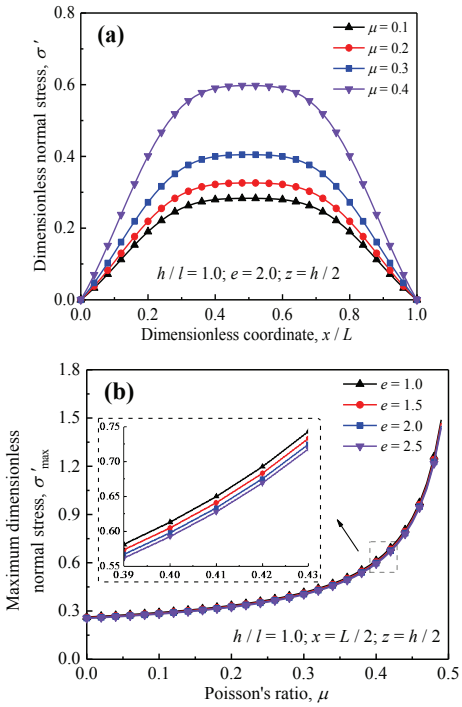

Figure 12 Normal stress curves related to the Poisson effect: (a) dimensionless normal stress vs. dimensionless coordinate with different value of Poisson's ratio, and (b) maximum dimensionless normal stress vs. Poisson's ratio with different value of FG parameter.

Figure 12(a) shows the dimensionless normal stress curves versus dimensionless coordinate with respect to different values of Poisson's ratio. It is clear that a platform appears in the dimensionless normal stress curve due to the FG effect of an AFG micro-beam. The altitude of platform of dimensionless normal stress increases with the increased value of Poisson's ratio. This indicates the influence of Poisson's ratio on the dimensionless normal stress, which is the Poisson effect of normal stress of an AFG micro-beam.

Figure 12(b) shows the maximum dimensionless normal stress curves versus Poisson's ratio with respect to different values of FG parameter. It is seen that the value of maximum dimensionless normal stress nonlinearly increases with the increased value of Poisson's ratio, which means that the Poisson effect of normal stress of an AFG micro-beam is obvious. It is found that the maximum dimensionless normal stress curves with different values of FG parameter are very close and similar, which means that the influence of FG parameter on the Poisson effect of normal stress of an AFG micro-beam is not obvious and then can be neglected.

6.4 Poisson effect of couple stress

The Poisson effect of couple stress of the AFG micro-beam in Figure 1 is numerically investigated in this section. Figure 13 shows the couple stress curves related to the Poisson effect, where the dimensionless couple stress is calculated by Eq. (39) and maximum dimensionless couple stress is specified by Eq. (39) with x = L/2, respectively.

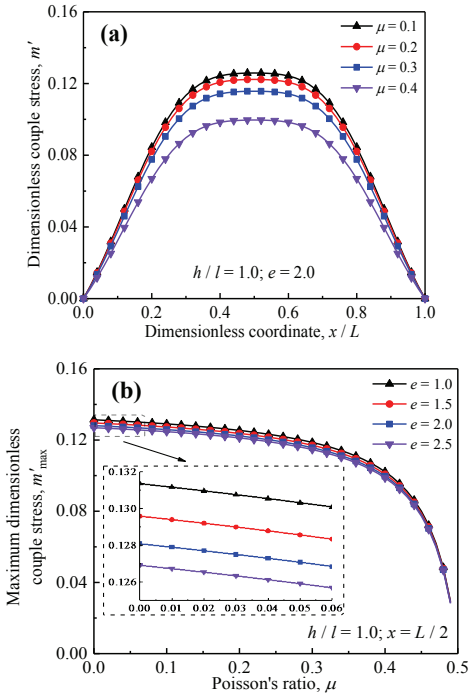

Figure 13 Couple stress curves related to the Poisson effect: (a) dimensionless couple stress vs. dimensionless coordinate with different value of Poisson's ratio, and (b) maximum dimensionless couple stress vs. Poisson's ratio with different value of FG parameter.

Figure 13(a) shows the dimensionless couple stress curves versus dimensionless coordinate with respect to different values of Poisson's ratio. It is clear that a platform also appears in the dimensionless couple stress curve due to the FG effect of couple stress of an AFG micro-beam. The altitude of platform decreases with the increased value of

Poisson's ratio. This explains the influence of Poisson's ratio on the dimensionless couple stress, which is the Poisson effect of couple stress of an AFG micro-beam.

Figure 13(b) plots the maximum dimensionless couple stress curves versus Poisson's ratio with respect to different values of FG parameter. It is seen that the value of maximum dimensionless couple stress nonlinearly decreases with the increased value of Poisson's ratio, which indicates that the Poisson effect of couple stress of an AFG micro-beam is obvious. It is found that maximum dimensionless couple stress curves for different values of FG parameter are very close and similar, which indicates that the influence of FG parameter on the Poisson effect of couple stress of an AFG micro-beam is not obvious and then can be neglected.

7 Conclusions

The components of strain, curvature, stress and couple stress of an AFG micro-beam are described according to the MCST and Bernoulli-Euler theory. The size-dependent model related to FG effect and Poisson effect is developed to describe and predict the mechanical behaviors of the AFG micro-beam by using the principle of minimum potential energy. The mechanical behaviors of the AFG micro-beam, which are related to size the effects, FG effects and Poisson effects, are numerically investigated via the dimensionless definitions such as dimensionless bending stiffness, dimensionless deflection, dimensionless normal stress and dimensionless couple stress. Through the numerical simulation, some important conclusions are summarized as follows.

1) The size effects of mechanical behaviors, which includes the size effects of bending stiffness, deflection, normal stress and couple stress of the AFG micro-beam, are obvious when the value of dimensionless height is small enough. However the size effects can be neglected when the value of dimensionless height of micro-beam is large enough.

2) The FG effects, i.e. the influences of FG parameter, are important factors related to the bending stiffness and deflection of AFG micro-beam. However the FG effects of normal stress and couple stress are not very obvious. The dimensionless height has visible influences on the FG effects of bending stiffness, deflection, normal stress and couple stress of the AFG micro-beam.

3) The Poisson effects, i.e. the influences of Poisson's ratio, are not negligent for the bending stiffness, deflection, normal stress and couple stress of the AFG micro-beam. The dimensionless height has obvious influences only on the Poisson effects of bending stiffness and deflection, while it has little influences on the Poisson effects of normal stress and couple stress.

Author Contributions: Bo ZHOU first proposed a method to analyze the size effect, functionally graded (FG) effect and Poisson effect of an axially functionally graded (AFG) micro-beam by using Bernoulli-Euler beam theory and modified coupled stress theory and combining with the principle of minimum potential energy. Shuai WANG established a size-dependent model related to FG effect and Poisson effect, including the calculation formulas of bending stiffness, deflection, normal stress and couple stress, and numerically investigated the size effect, FG effect and Poisson effect of simply supported AFG micro-beam of the established model. Zetian KANG and Shichen ZHOU determined the displacement field of AFG micro-beam based on Bernoulli-Euler beam theory. And expressed the components of strain, curvature, stress and couple stress according to the modified coupling stress theory. Using the principle of minimum potential energy. Shifeng XUE put forward some guiding opinions on the logicality and innovation of the article.

Conflict of Interest: We are committed to that there is no conflict of interest regarding the publication of this paper.

Acknowledgments: The authors of this paper acknowledge the supports from the National Key Research and Development Program of China (Grant No. 2017YFC0307604) and the Talent Foundation of China University of Petroleum (Grant No. Y1215042).

This is the Appendix: This article does not cover the details that require an appendix.

References

[1] Asghari M, Ahmadian M T, Kahrobaiyan M H, Rahaeifard M, 2010. On the size-dependent behavior of functionally graded micro-beams. Materials & Design. 31(5), 2324-2329. https://doi.org/10.1016/j.matdes.2009.12.006

[2] Dai H L, Wang Y K, Wang L, 2015. Nonlinear dynamics of cantilevered microbeams based on modified couple stress theory. International Journal of Engineering Science. 94, 103-112. https://doi.org/10.1016/j.ijengsci.2015.05.007

[3] Dehrouyeh-Semnani A M, Nikkhah-Bahrami M, 2015a. The influence of size-dependent shear deformation on mechanical behavior of microstructures-dependent beam based on modified couple stress theory. Composite Structures. 123, 325-336. https://doi.org/10.1016/j.compstruct.2014.12.038

[4] Dehrouyeh-Semnani A M, Nikkhah-Bahrami M, 2015b. A discussion on incorporating the poisson effect in microbeam models based on modified couple stress theory. International Journal of Engineering Science. 86, 20-25. https://doi.org/10.1016/j.ijengsci.2014.10.003

[5] Ghayesh M H, Farokhi H, Gholipour A, Tavallaeinejad M, 2017. Nonlinear bending and forced vibrations of axially functionally graded tapered microbeams. International Journal of Engineering Science. 120, 51-62. https://doi.org/10.1016/j.ijengsci.2017.03.010

[6] Heydari A, Jalali A, Nemati A, 2017. Buckling analysis of circular functionally graded plate under uniform radial compression including shear deformation with linear

and quadratic thickness variation on the Pasternak elastic foundation. Applied Mathematical Modelling. 41, 494-507. https://doi.org/10.1016/j.apm.2016.09.012

[7] Huang Y, Li X F, 2010. A new approach for free vibration of axially functionally graded beams with non-uniform cross-section. Journal of Sound and Vibration. 329(11), 2291-2303. https://doi.org/10.1016/j.jsv.2009.12.029

[8] Karamanlı A, Vo T P, 2018. Size dependent bending analysis of two directional functionally graded microbeams via a quasi-3D theory and finite element method. Composites Part B: Engineering. 144, 171–183. https://doi.org/10.1016/j.compositesb.2018.02.030

[9] Ke L L, Wang Y S, 2011. Size effect on dynamic stability of functionally graded micro-beams based on a modified couple stress theory. Composite Structure. 93(2), 342-350. https://doi.org/10.1016/j.compstruct.2010.09.008

[10] Ke L L, Wang Y S, Yang J, Kitipornchai S, 2012a. Free vibration of size-dependent Mindlin microplates based on the modified couple stress theory. Journal of Sound and Vibration. 331(1), 94-106. https://doi.org/10.1016/j.jsv.2011.08.020

[11] Ke L L, Yang J, Kitipornchai S, Bradford M A, 2012b. Bending, buckling and vibration of size-dependent functionally graded annular microplates. Composite Structures. 94(11), 3250-3257. https://doi.org/10.1016/j.compstruct.2012.04.037

[12] Kong S L, Zhou S J, Nie Z F, Wang K, 2008. The size-dependent natural frequency of Bernoulli-Euler micro-beams. International Journal of Engineering Science. 46(5), 427-437. https://doi.org/10.1016/j.ijengsci.2007.10.002

[13] Kouzeli M, Mortensen A, 2002. Size dependent strengthening in particle reinforced aluminium. Acta Materialia. 50(1), 39-51. https://doi.org/10.1016/S1359-6454(01)00327-5

[14] Lama D C C, Yang F, Chonga A C M, Wang J, Tong P, 2003. Experiments and theory in strain gradient elasticity. Journal of the Mechanics and Physics of Solids. 51, 1477-1508. https://doi.org/10.1016/S0022-5096(03)00053-X

[15] Li X B, Li L, Hu Y J, Ding Z, Deng W M, 2017. Bending, buckling and vibration of axially functionally graded beams based on nonlocal strain gradient theory. Composite Structures. 165, 250-265. https://doi.org/10.1016/j.compstruct.2017.01.032

[16] Liu Z, Meyers M A, Zhang Z, Ritchie R O, 2017. Functional gradients and heterogeneities in biological materials: Design principles, functions, and bioinspired applications. Progress in Materials Science. 88, 467-498. https://doi.org/10.1016/j.pmatsci.2017.04.013

[17] Ma H M, Gao X L, Reddy J N, 2008. A microstructure-dependent Timoshenko beam model based on a modified couple stress theory. Journal of the Mechanics & Physics of Solids. 56(12): 3379-3391. https://doi.org/10.1016/j.jmps.2008.09.007

[18] Mohammadabadi M, Daneshmehr A R, Homayounfard M, 2015. Size-dependent thermal buckling analysis of micro composite laminated beams using modified couple stress theory. International Journal of Engineering Science. 92, 47-62. https://doi.org/10.1016/j.ijengsci.2015.03.005

[19] Naebe M, Shirvanimoghaddam K, 2016. Functionally graded materials: A review of fabrication and properties. Applied Materials Today. 5, 223-245. https://doi.org/10.1016/j.apmt.2016.10.001

[20] Park S K, Gao X L, 2006. Bernoulli-Euler beam model based on a modified couple stress theory. Journal of Micromechanics & Microengineering. 16(11), 2355-2359. http://iopscience.iop.org/article/10.1088/0960-1317/16/11/015/meta

[21] Pradhan K K, Chakraverty S, 2013. Free vibration of Euler and Timoshenko functionally graded beams by Rayleigh-Ritz method. Composites Part B: Engineering. 51(4), 175-184. https://doi.org/10.1016/j.compositesb.2013.02.027

[22] Reddy J N, 2000. Analysis of functionally graded plates. International Journal for Numerical Methods in Engineering. 47(1-3), 663-684. https://doi.org/10.1002/(SICI)1097-0207(20000110/30)47:1/3<663::AID-NME787>3.0.CO;2-8

[23] Reddy J N, 2011. Microstructure-dependent couple stress theories of functionally graded beams. Journal of the Mechanics & Physics of Solids. 59(11), 2382-2399. https://doi.org/10.1016/j.jmps.2011.06.008

[24] Salamat-Talab M, Nateghi A, Torabi J, 2012. Static and dynamic analysis of third-order shear deformation FG micro beam based on modified couple stress theory. International Journal of Mechanical Sciences. 57(1), 63-73. https://doi.org/10.1016/j.ijmecsci.2012.02.004

[25] Shahba A, Attarnejad R, Marvi M T, Hajilar S, 2011. Free vibration and stability analysis of axially functionally graded tapered Timoshenko beams with classical and non-classical boundary conditions. Composites Part B: Engineering. 42(4), 801-808. https://doi.org/10.1016/j.compositesb.2011.01.017

[26] Sola A, Bellucci D, Cannillo V, 2016. Functionally graded materials for orthopedic applications - an update on design and manufacturing. Biotechnology Advances. 34(5), 504-531. https://doi.org/10.1016/j.biotechadv.2015.12.013

[27] Thai H T, Vo T P, Nguyen T K, Lee J, 2015. Size-dependent behavior of functionally graded sandwich microbeams based on the modified couple stress theory. Composite Structures. 123, 337-349. https://doi.org/10.1016/j.compstruct.2014.11.065

[28] Thai H T, Vo T P, Nguyen T K, Kim S E, 2017. A review of continuum mechanics models for size-dependent analysis of beams and plates. Composite Structures. 177, 196–

219. https://doi.org/10.1016/j.compstruct.2017.06.040
[29] Trinh L C, Nguyen H X, Vo T P, Nguyen T K, 2016. Size-dependent behaviour of functionally graded microbeams using various shear deformation theories based on the modified couple stress theory. Composite Structures. 154, 556-572. https://doi.org/10.1016/j.compstruct.2016.07.033
[30] Wu L, Wang Q S, Elishakoff I, 2005. Semi-inverse method for axially functionally graded beams with an anti-symmetric vibration mode. Journal of Sound and Vibration. 284(3-5), 1190-1202. https://doi.org/10.1016/j.jsv.2004.08.038
[31] Xu F, Zhang X, Zhang H, 2018. A review on functionally graded structures and materials for energy absorption. Engineering Structures. 171, 309-325. https://doi.org/10.1016/j.engstruct.2018.05.094
[32] Yang F, Chong A C M, Lam D C C, Tong P, 2002. Couple stress based strain gradient theory for elasticity. International Journal of Solids and Structures. 39(10), 2731-2743. https://doi.org/10.1016/S0020-7683(02)00152-X
[33] Zdeněk P, Bažant, 1984. Size effect in blunt fracture: concrete, rock, metal. Journal of Engineering Mechanics. 110 (4), 518-535. https://doi.org/10.1061/(ASCE)0733-9399(1984)110:4(518)
[34] Zhao L, Chen W Q, Lü C F, 2012. Symplectic elasticity for bi-directional functionally graded materials. Mechanics of Materials. 54, 32-42. https://doi.org/10.1016/j.mechmat.2012.06.001

Viser Technology Pte. Ltd.
Mechanical Engineering Science
doi: 10.33142/mes.v2i1.2618

Research Article Open Access

Vibration Frequency Characteristic Study of Two-stage Excitation Valve Used in Vibration Experiment System

Yongping WU[1], Chengwei XIONG[1], Yi LIU[1*,2], Jiafei ZHENG [1], Mingxuan ZOU[1]

1 NingboTech University, Ningbo 315100, China
2 Ningbo Shenglong Automotive Powertrain Systems Co., Ltd Ningbo 315105, China

***Corresponding Author:** Yi LIU, NingboTech University, Qianhu South Road No. 1, Ningbo 315100, Zhejiang Province, China; liuyilulu@nit.zju.edu.cn*

Abstract:
To satisfy the demands of higher frequency and amplitude in hydraulic vibration experiment system, the two-stage excitation valve is presented, and a mathematical model of two-stage excitation valve is established after analyzing the working principle of two-stage excitation valve, then the influence of relevant parameters on the displacement of main spool of two-stage excitation valve is studied by using Matlab/Simulink to calculate and analyze. The results show that the displacement of main spool will be smaller with bigger diameter and more secondary valve ports. When the reversing frequency is higher and the oil supply pressure is lower as well as the axial guide width of valve ports is smaller, the maximum displacement of main spool is smaller. The new two-stage excitation valve is easy to adjust reversing frequency and flow. The high frequency can be achieved by improving the rotation speed of servo motor and adding the number of secondary valve ports; the large flow can be realized by increasing the axial guide width of secondary valve ports and oil supply pressure. The result of this study is of guiding significance for designing the rotary valve for the achievement of higher reversing frequency and larger flow.

Keywords: *two-stage excitation valve; rotary valve control; mathematical modelling; numerical analysis*

1 Introduction

Vibration equipment mainly refers to a kind of equipment to generate corresponding vibration. With the further research on high-frequency electro-hydraulic vibration equipment, the vibration frequency has been greatly improved in recent years[1]. Due to the limitation of system frequency bandwidth and the influence of nonlinearity, the traditional electro-hydraulic vibration control technology based on servo control has a deviation between the response signal and the expected input signal, which is difficult to meet the current high accuracy and large flow[2,3]. Hydraulic rotary valve is used to control oil circuit's on-off and direction based on the spool's rotation relative to the valve sleeve or valve body. Compared with hydraulic slide valve, hydraulic rotary valve is significantly different on structural features and performance parameters. So far, the researches on rotary valve are as follows: Ivan Okhotnikov et al. investigated the metering characteristic and pressure losses of the rotary tubular spool valve[4]. Hao Jiangong et al. improved the vibration frequency and the flow of wave generator through the structure of rotary valve, and applied it to the mining industry, metallurgical industry, construction industry and so on[5]. Lu Juxian et al. designed a servo rotary valve and Fu Yongling et al. analyzed the structure and principle of its rotary spool, then deduced the steady flow force when it was working and did a simulating calculation[6,7].Ren Yan et al. presented various series rotary valves applied in the field of vibration engineer and studied the frequency characteristic of electrohydraulic vibration excitor controlled by rotary valve [8–10]. Gong Guofang proposed a high speed rotary valve with four-way commutation that can improve the frequency and flow, which applied to the high-power variable-frequency vibration of tamping device[11]. Li Xing et al. developed the spool transferring composite hydraulic vibration control valve and its hydraulic system[12]. Cui Jian developed a direct-acting electrohydraulic rotary valve[13]. Liu Yi et al[14,15] designed a rotary valve for application to variable-frequency vibration condition. The rotary valve can be used to obtain the required vibration frequency and waveform, and thus meet different working requirements of the tamping machine and wave maker.

In this paper, in order to further increase the reversing

frequency and the flow of rotary valve in hydraulic vibration experiment system, a new two-stage excitation valve element is presented based on the analysis of the application of the above rotary valve control elements. Then the working principle of two-stage excitation valve is described and the mathematical model is established. Finally, the characteristic of two-stage excitation valve is numerically analyzed.

2 Working Principle of Two-stage Excitation Valve

The working principle of two-stage excitation valve is shown in Fig. 1. the oil ports of main valve communicate with the corresponding oil ports of secondary rotary valve. The stepping motor makes secondary spool moving, so the opening size of spool can be changed, and then control the flow of oil. The servo motor drives the secondary spool rotation. Because of the multiple symmetric arrangement ports in four steps of secondary spool, when secondary spool cycles one revolution, the oil reverse several times. The rotation and movement of secondary spool are driven by the control electromotor when the oil flow from the intake of main valve into the intake of secondary valve, so that the oil of secondary valve can communicate with the oil of the right and left chambers of main spool, and then the main spool can move around. Finally, the oil of main valve is inverted. As shown in Fig.1, the oil-way of secondary valve as indicated by the arrows, the oil that flow into the control chamber of main spool can be directed to right end so that the main spool move left to make P switch on B and A switch on T. The control oil will flow into the left side of main spool control chamber when the secondary spool continue to rotate to an angle, then the main spool will move right to make P switch on A and B switch on T.

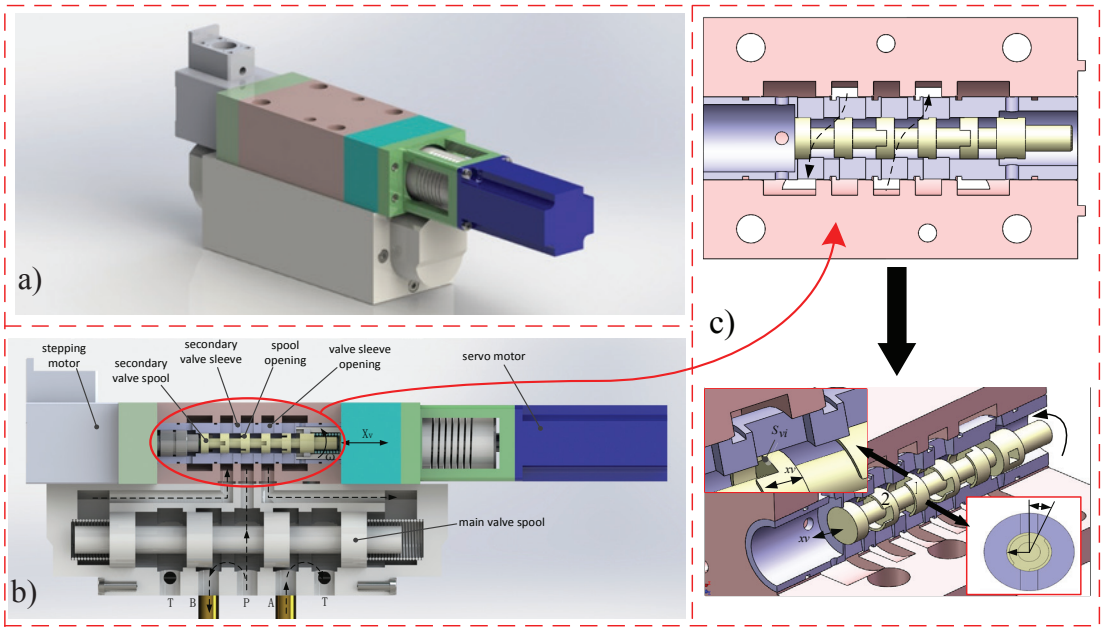

(a) Overall chart. (b) Structural schematic diagram. (c) Reversing schematic diagram.

Figure 1 Two-stage excitation valve

3 Mathematical Modelling

According to the working principle diagram, the equivalence principle analysis diagram is shown in Fig. 2.

The top part of diagram is the simplified model of secondary rotary valve, shown in Fig. 1(c).

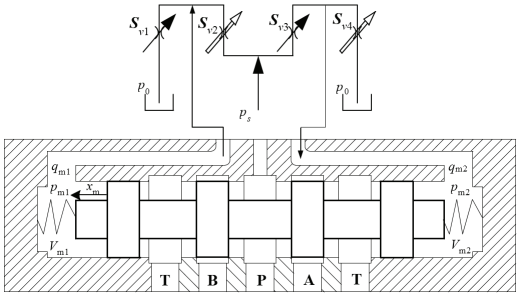

Figure 2 Equivalence principle analysis diagram

3.1 Flow equation of secondary rotary valve

It is assumed that the flow is the ideal fluid in the steady condition, the oil-supply pressure p_s is constant, p_0 is the return pressure of hydraulic system, q_s is the supply flow, the pressure of hydraulic cylinder two chambers are p_{m1} and p_{m2}, respectively, S_{vi} is the conduction area of rotary valve port. On the basis of orifice flow equation in the hydrodynamics theory, the equation of the flow through orifices 1, 2, 3, and 4 are shown as follows:

$$q_{v1} = C_d S_v(x_v, t)\sqrt{\frac{2(p_{m1} - p_0)}{\rho}}$$

$$q_{v2} = C_d S_v(x_v, t)\sqrt{\frac{2(p_s - p_{m1})}{\rho}}$$

$$q_{v3} = C_d S_v(x_v, t)\sqrt{\frac{2(p_s - p_{m2})}{\rho}}$$

$$q_{v4} = C_d S_v(x_v, t)\sqrt{\frac{2(p_{m2} - p_0)}{\rho}}$$

Where C_d is the flow coefficient, ρ is the oil density.

The structure of valve is shown in Fig. 3, x_v is the axial conduction width of valve port, R is the shoulder radius of the rotary spool. Assuming that every shoulder evenly open $2n$ grooves (then in the Fig. 3 is 2), and the opening of grooves on the front and back shoulders distribute with uniformity and symmetry, the windows and grooves of valve are designed as rectangle, then the equation of the flow conduction area is $S_v(x_v, t)=2nx_v y_v$. Assuming that the opening circumferential conduction width of front and back shoulders are y_{v1} and y_{v2}, respectively, definite y_{v1} from zero to maximum, after that from maximum to zero, then enter the next opening mouth of back shoulder y_{v2}, which is as well from zero to maximum, then from maximum to zero. Suppose, the rotary frequency of spool is f, the rotational angular velocity is ω_1, so the equation of y_{v1} and y_{v2} are:

$$y_{v1} = \begin{cases} 2R\sin\dfrac{\omega_1 t}{2} & (0 \le \omega_1 t < \dfrac{\pi}{4n}) \\ 2R\sin\left[\dfrac{\pi}{4n} - \dfrac{\omega_1 t}{2}\right] & (\dfrac{\pi}{4n} \le \omega_1 t < \dfrac{\pi}{2n}) \\ 0 & (\dfrac{\pi}{2n} \le \omega_1 t < \dfrac{3\pi}{4n}) \\ 0 & (\dfrac{3\pi}{4n} \le \omega_1 t \le \dfrac{\pi}{n}) \end{cases} \quad (5)$$

$$y_{v2} = \begin{cases} 0 & (0 \le \omega_1 t < \dfrac{\pi}{4n}) \\ 0 & (\dfrac{\pi}{4n} \le \omega_1 t < \dfrac{\pi}{2n}) \\ 2R\sin\left[\dfrac{\omega_1 t}{2} - \dfrac{\pi}{4n}\right] & (\dfrac{\pi}{2n} \le \omega_1 t < \dfrac{3\pi}{4n}) \\ 2R\sin\left[\dfrac{\pi}{2n} - \dfrac{\omega_1 t}{2}\right] & (\dfrac{3\pi}{4n} \le \omega_1 t < \dfrac{\pi}{n}) \end{cases} \quad (6)$$

Fig. 3 suggests that a single complete cycle of spool valve rotation, the four times of oil reversing, so the relation of working frequency of main valve to rotational frequency of spool is $f_m = 2nf$.

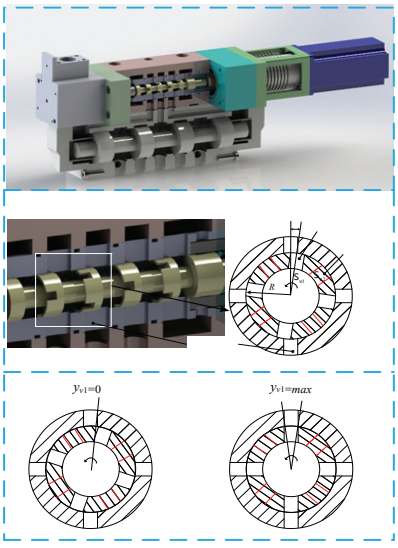

Figure 3 Structure of valve

3.2 Flow continuity equation of the right and left control chambers of main spool

For the left chamber:

$$q\mathrm{m1} = q\mathrm{v2} - q\mathrm{v1} = Am\ddot{x}_m + \frac{V\mathrm{m1}}{E}\dot{P}_{\mathrm{m1}} + C\varepsilon\mathrm{m}P\mathrm{m1} \quad (7)$$

For the right chamber:

$$q\mathrm{m2} = q\mathrm{v3} - q\mathrm{v4} = Am\ddot{x}_m - \frac{V\mathrm{m2}}{E}\dot{P}_{\mathrm{m2}} + C\varepsilon\mathrm{m}pP\mathrm{m2} \quad (8)$$

Where x_m is the displacement of main spool; E is the bulk modulus of oil; A_m is the effective action area of main spool; C_{emp} is the out leakage coefficient of main valve, V_{m1} is the volume of main valve left chamber, V_{m2} is the volume of main valve right chamber. Assuming that the initial position of spool is in the middle, then $V_{m1}=V_{m2}$.

3.3. Force balance equation of main spool

$$A_m(P_{\mathrm{m1}} - P_{\mathrm{m2}}) = m_m\ddot{x}_m + B_m\dot{x}_m + k_m x_m + F_m \quad (9)$$

Where P_{m1}, P_{m2} are the pressure of the left and right control chamber of spool, respectively;

m_m is the mass of main spool; x_m is the displacement of main spool; B_m is the viscous damping coefficient of main spool; k_m is the spring stiffness of main spool; F_m is the steady flow force of main valve. Assuming that the motion of main spool mainly overcome the force of spring stiffness, the friction between main spool and valve sleeve is very small, about 500 N·s/M, the flow force is far less than the force to overcome the spring stiffness.

4 Numerical Analysis

According to the mathematical modelling in the sections above, the solving model of two-stage excitation valve is established through Matlab/Simulink. The total model of two-stage excitation valve can be obtained through deriving the relationship between input and output after checking the accuracy of the solving model of every subsystem, as is shown in Fig. 4. By setting every parameter of model, input different size of controlling parameters to obtain the influence on the performance of the two-stage excitation valve. The key parameters of the rotary valve are shown in Table 1.

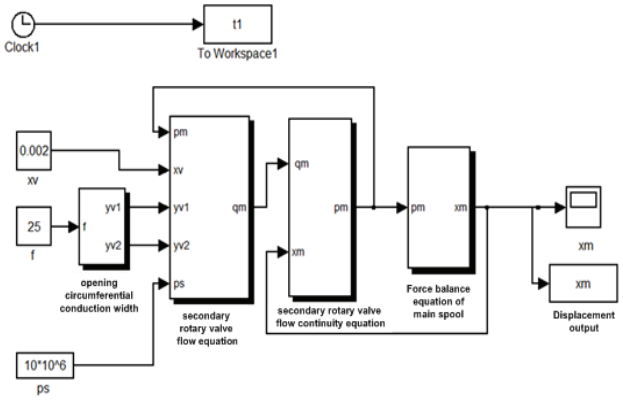

Figure 4 Solving Model of two-stage excitation valve

Table 1 Main parameters of the system of two-stage excitation valve

Parameter	Values	Parameter	Values
B_m (N·s/M)	500	n	1-4
C_d	0.62	p_s (Mpa)	10-21
D_m (mm)	35-44	R(mm)	8
E (Pa)	8×10^8	V_{m1} (m^3), V_{m2} (m^3)	1.9×10^{-5}
k_m (N/m)	50000	x_v (mm)	1-2
m_m (kg)	0.5	y_{vmax} (mm)	3
ρ(kg/m^3)	870		

4.1 Influence of different main spool diameter on the displacement of main spool

Fig. 5 and 6 show the displacement of main spool and the flow area curves from different frequency when the main spool are 35mm and 44mm, respectively. When the oil-supply pressure is 10MPa, x_v=2mm, D_m=35mm, the maximum displacement of main spool and the maximum flow area can achieve 4mm and 440mm^2 with 50Hz. The maximum displacement of main spool and the maximum flow area when frequency is 100Hz are 1/2 of that when frequency is 50Hz. The maximum displacement of main spool and the maximum flow area when frequency is 200Hz are 1/4 of that when frequency is 50Hz. Among them, when D_m=44mm, the maximum displacement of main spool and the maximum flow area are 3.2mm and 440mm^2 with 50Hz. The changing rule of the maximum displacement of main spool and the maximum flow area are the same as the above. Under the same condition, when D_m=44mm, the displacement of main spool is smaller, but the total flow area is invariant relative to the main spool that D_m=35mm.

According to $Q_{mmax} = C_d \pi D_m x_m \sqrt{\frac{2p_s}{\rho}}$, when D_m=35mm, x_m=4mm, p_s=10MPa, the maximum flow can achieve 0.041 m^3/s under no-load condition.

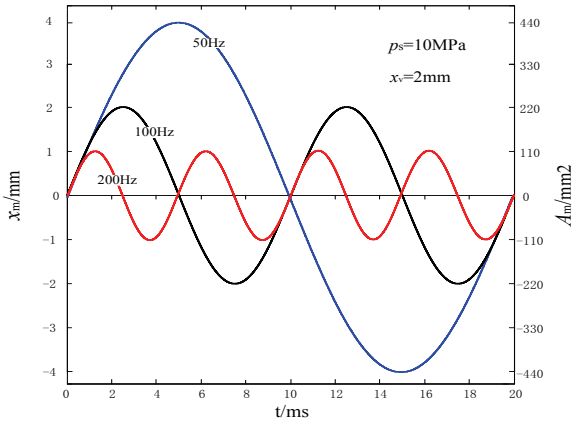

Figure 5 Curves of x_m and A_m with different frequency (the main spool D_m is 35mm)

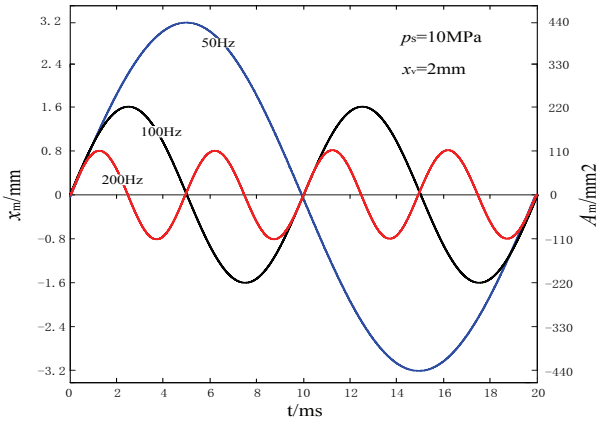

Figure 6 Curves of x_m and A_m with different frequency (the main spool D_m is 44mm)

4.2. Influence of different oil-supply pressure on the displacement of main spool

Fig.7 shows maximum value of x_m with different frequency under three different oil-supply pressure, when the reserving frequency is higher, the maximum value of x_m is smaller; when the oil-supply pressure is higher, the maximum value of x_m is bigger. When the oil-supply pressure is 21MPa, x_v=2mm and f_m=50Hz, the maximum value of x_m can achieve 7mm.

4.3. Influence of different x_v on the displacement of main spool

Fig. 8 shows the maximum value of x_m with different frequency when x_v are 2mm and 1.5mm, respectively. It can be seen from Fig. 8, the smaller the x_v, the smaller the maximum value of x_m . Figs. 7 and 8 show that the main spool can be controlled through controlling the oil-supply pressure of control system, rotate speed of secondary spool and the axial displacement of spool. Besides, when the oil-supply pressure is 21MPa, x_v=2mm and f_m=50Hz, the maximum value of x_m can achieve 7mm.

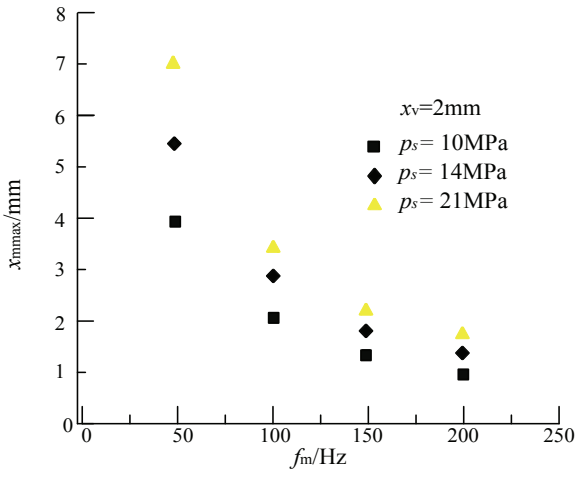

Figure 7 Maximum value of x_m with different reversing frequency (three oil-supply pressure)

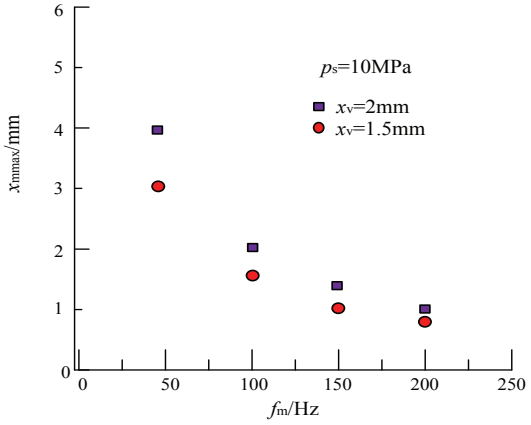

Figure 8 Curves of maximum value of x_m with different frequency(the axial opening of different secondary valves)

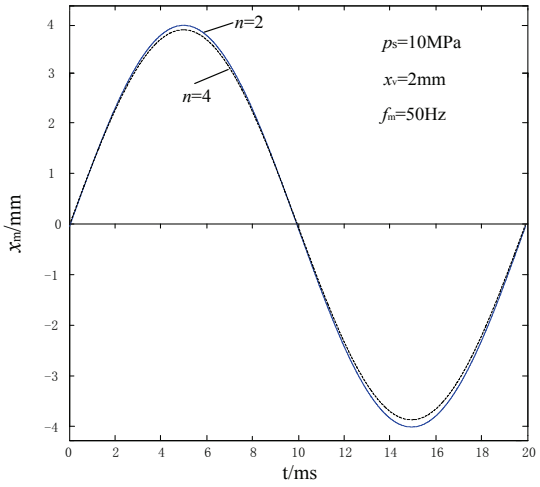

Figure 9 Curves of x_m with different n

4.4. Influence of different number of secondary valve ports on the displacement of main spool

It can be seen from Fig. 9, when the oil-supply pressure is 10MPa, the reversing frequency of main spool is 50Hz, x_v=2mm, the displacement of two-stage valve main spool with 8 secondary valve ports is slightly smaller than that with 4 secondary valve ports. The total flow conduction areas are same with different number of secondary valve ports shown as Fig.10 in theory. However, the more the number of secondary valve ports, the bigger the local resistance of the single controlling port to the oil, causing the displacement of main spool smaller when other condition are same. According to the structure of valve and the equation f_m=2nf, we can get that it is easy to realize bigger reversing frequency or high frequency vibration with more secondary valve ports.

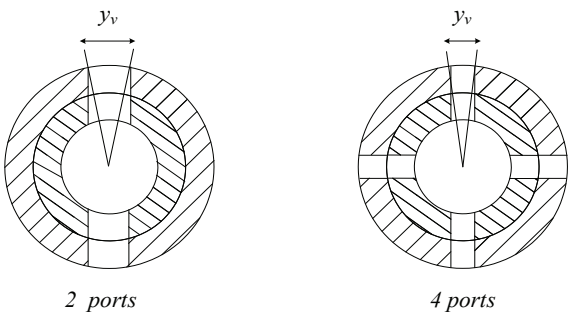

Figure 10 Width of y_v with different ports

Conclusion

The paper presents a new two-stage excitation valve used in vibration experiment system and establishes the mathematical models. The characteristic of two-stage excitation valve is obtained by using Matlab/Simulink.

The results show that the displacement of main spool will be smaller with bigger diameter and more secondary valve ports. The maximum displacement of main spool will be smaller with higher reversing frequency, lower oil-supply pressure and smaller axial guide width of valve ports. The new two-stage excitation valve is easy to adjust reversing frequency and flow. The higher frequency can be realized by adding the number of secondary valve ports. The larger flow can be achieved by increasing axial guide width of secondary valve ports and oil supply pressure. The result of this study is of guiding significance for designing the rotary valve for the achievement of higher reversing frequency and larger flow.

Acknowledgments: This work was supported by the Ningbo "Science and Technology Innovation 2025" major project （202002P2004）, the Natural Science Foundation of Ningbo City of China (2019A610162) and the National Natural Science Foundation of China (51605431).

References

[1] Li Xiaojun, Li Fangfang, Ji Jinbao, Wang Juke. A new control technology of shaking table based on the jerk. Advanced Engineering Sciences 2018, Volume (3), pp. 64-72.

[2] Xin Yanggui, Dou Baohui, Pei Yang, Liu Chunhu. Application of high frequency electro-hydraulic vibration system. Machine Tool & Hydraulics 2015, Volume 43(13), pp. 106-107.

[3] Wang Wei. Research on the technology of impact vibration based on four-way rotary valve. Zhejiang University, 2016.

[4] Ivan O, Karem A, Siamak S, Philip, G. Numerical and experimental investigation of the metering characteristic and pressure losses of the rotary tubular spool valve. Flow Measurement and Instrumentation 2020, DOI :

https: // doi.org/ 10.1016/ j.flowmeasinst. 2019.101679.

[5] Hao Jiangong, Zhang Yaocheng. Study on the properties of a new electrohydraulic exciting system. Journal of Taiyuan University of Technology 2003, Volume 6, pp.706-709.

[6] Lu Juxian, Li Shuli, Jiao Zongxia. A Limited-angle rotating of Electro-Hydraulic Servo-valve. Hydraulics Pneumatics & Seals 2005, Volume 4, pp.40-42.

[7] Fu Yongling, Song Guobiao. The steady flow force analysis of a new direct drive servo valve. Machine Tool & Hydraulics 1998, Volume 6, pp.18-20.

[8] Ren Yan, Tang Hesheng, Xiang Jiawei, Experimental and numerical investigations of hydraulic resonance characteristics of a high-frequency excitation system. Mechanical Systems and Signal Processing 2019, Volume 131, pp. 617-632.

[9] Ren Yan, Bai Jiping, Ruan Jian, Design, modeling and experimental validation of a variable resonant electro-hydraulic fatigue testing system. IEEE ACCESS 2019, Volume 7, pp.180825-180845.

[10] Ren Yan, Ji Xiancheng, Ruan Jian, Output characteristics of a horizontal type electro-hydraulic excitation system with inertial loading: Modeling and experimentation. Journal of Mechanical Science and Technology 2019, Volume 33(11), pp. 5157-5167.

[11] Liu Yi, Gong Guofang, Yang Huayong, Han Dong, and Wang He. Regulating Characteristics of New Tamping Device Exciter Controlled by Rotary Valve . IEEE/ASME Transactions on Mechatronics, 2016, Volume 21(1), pp.497-505.

[12] Wang Weirui, Li Xing, Ge Zheng, Shi Haoran. The spool transfering composite hydraulic vibration control valve and its hydraulic system: China, 201410839682.5.[P].2016-06-08.

[13] Cui Jian, Ding Fang, Li Qi Peng. Novel bidirectional rotary proportional actuator for electrohydraulic rotary valves. IEEE Transactions on Magnetics 2007, Volume 43(7), pp.3254-3258.

[14] Liu Yi, Cheng ShaoKe, Gong GuoFang. Structure characteristics of valve port in the rotation-spool-type electro-hydraulic vibrator. Journal of Vibration and Control 2017, Volume 23, pp. 2179-2189.

[15] Liu Yi, Jiafei ZHENG , Song Ruiyin, Xu Qiaoning, Chen Junhua, Huang Fangping. Simple Push-Type Wave Generating Method Using Digital Rotary Valve Control. Chinese Journal of Mechanical Engineering 2020, Volume 33(1), pp. 1-16.

Viser Technology Pte. Ltd.
Mechanical Engineering Science
doi: 10.33142/mes.v2i1.2619

Research Article Open Access

Design and Engineering Application of Direct Mixing Lubrication System for Emulsion Pipeline in Secondary Cold Rolling Mill

Hangzhe DONG[1], Yazhen ZHANG[1], Wantong HU[1],Zhen-hua BAI[2*],Yan-yan ZHANG[1*]

1 National Engineering Research Center for Equipment and Technology of Cold Strip Rolling, Yanshan University, Yanshan University, Qinhuangdao, China

2 State Key Laboratory of Metastable Materials Science and Technology, Yanshan University, Qinhuangdao, China

***Corresponding Author:** Zhenhua BAI, E-mail: bai_zhenhua@aliyun.com; Yanyan ZHANG, E-mail: ysuzhang2020@126.com*

Abstract:

With the benefit fierce competition in the steel industry market in recent years, double cold reduction products have been developed towards strength improvement and thickness reduction. The traditional cold-rolling lubrication process with a fixed flow rate and concentration cannot solve the problems,which are uncontrollable plate shape and the excessive consumption of lubricating oil. Moreover,based on the analysis of the traditional direct aplication lubrication system of double cold reduction mill, a set of design scheme suitable for the emulsion pipeline direct mixing lubrication system of double cold reduction mill unit was proposed.The design completed the selection of key components, which included the static mixer and atomization nozzle selection, pump and oil pump design selection, pipeline design selection, flow type selection, pressure gauge selection, electronic control cabinet design selection and other eight aspects. Equipment of the emulsion pipeline direct mixing lubrication system of double cold reduction has been developed. Comparing with characteristics of the traditional direct aplication lubrication system, the emulsion pipeline direct mixing lubrication system was better applied to the production practice of a 1220 double cold reduction mill. The consumption of ton of steel was reduced by 9.6%. The rolling energy consumption and fuel consumption comprehensive costs decreased by 10.7%, and the strip steel section thickness difference was reduced by 19.3%. In addition, the plate shape quality defect rate decreased by 25.6 %, otherwise creating a large economic benefit for the unit and promoting the application value.

Keywords: *double cold reduction; emulsion; direct mixing lubrication system; static mixer; plate thickness*

1 Introduction

With the continuous expansion of the market for cans, packaging and other industries, the double cold reduction industry has achieved rapid development[1,2]. Simultaneously, downstream users are increasingly demanding the thickness and strength of products to reduce the cost of raw materials and increase the profitability of cans and packaging. For these users, if the thickness of the plate is reduced by half, then the area of the plate is doubled. Therefore, high strength and thinning have become the trend of double cold reduction product development[3]. In the double cold reduction process, the traditional direct aplication lubrication system is preconfigured in the mixing tank, and this process spends some time stirring the mixture to achieve the emulsion particle size, ESI(Emulsion stability factor) and other characteristic parameters required for on-site production; accordingly, it cannot be adjusted online in real time. The emulsion concentration and the flow rate during the production of the same coil have nearly no adjustment. Thus, for ultra-thin high-strength double cold reduction products with high rolling stability and high precision of plate shape and thickness control, the conventional flow lubrication process with fixed flow rate and concentration can not meet customer needs, because of rolling pressure with the change of rolling speed and excessive fluctuations, rolling instability, unmanageable plate and thickness , growing oil consumption[4-5]. Kimura and Fujita solve the vibration problem of thin strip steel during high-speed rolling by dynamically controlling the flow of direct injection of hybrid-lubrication system[6]Das and his team researched the drop breakage model in static mixers at low and Intermediate reynolds number[7].On the basis of numerous field tests and theoretical studies, a static mixer is applied to the lubrication system of double cold reduction, and the static oil mixer directly mixes the rolling oil with water to replace the original emulsion mixing tank.And developed a emulsion pipeline direct mixing

lubrication system that is suitable for double cold reduction. This lubrication system, with the online adjustment of the flow rate and concentration, eventually achieves the goal of maximum improvement of rolling stability and reducing fuel consumption. This study will introduce the design principle of the emulsion pipeline direct mixing lubrication system, the selection of key components and the application effect of the project.

2 Brief introduction of traditional direct aplication lubrication system for double cold reduction

The traditional direct aplication lubrication system uses a high-concentration, small-flow emulsion, whose concentration is generally 5%–15%, and the flow rate is generally lower than 30 L/min (see Figure 1). The emulsion is sprayed on the strip surface at a certain distance from the roll gap. The rolling oil droplets in the emulsion are separated from the water and gradually precipitate on the strip surface given the oleophilic hydrophobic property of the strip surface. And oil film provides lubricantion during the rolling process. The emulsion of the direct aplication lubrication system only plays a lubricating role in the rolling process. A special roll cooling system is arranged on the outlet side of the rolling deformation zone, and considerable cooling water is sprayed on the roll surface for cooling. Rolling lubrication and cooling capacity can be adjusted separately[8]. The traditional direct aplication lubrication system are discharged directly after use without recycling, thereby resulting in high fuel consumption and waste of substantial emulsion. Therefore, controlling fuel consumption can reduce production costs and environmental pressure.

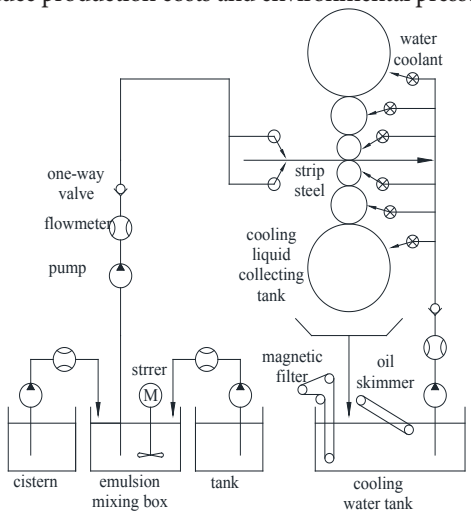

Figure 1 Schematic of the traditional direct application lubrication system.

3 Design of the emulsion pipeline direct mixing lubrication system

3.1 Design principle of the emulsion pipeline direct mixing lubrication system

A schematic of the emulsion pipeline direct mixing lubrication system of the double cold reduction unit is shown (see Figure 2). During the on-site production process of double cold reduction unit, the deionised water in the pump water tank passes through the water filter, flow metrer and pressure gauge,three-way and one-way valves are sent to the upper and lower static mixing inlets,and controlling the flow of deionized water and rolling oil by adjusting the speed of the pump and oil pump in real time with inverter to achieve the flow and concentration of emulsifiers required to regulate different steel species and rolling speeds. The rolling oil and deionised water are sequentially flowed through the static mixing unit in a static mixer, dispersed and mixed into an emulsion and sprayed on the upper and lower surfaces of the strip through nozzles on the upper and lower spray racks. The emulsion is sprayed on the upper and lower spray racks. Ten emulsion nozzles are installed. The double cold reduction strips and the production gap of the strip, the switching of the opening position of the three-way valve, the self-circulation of the deionised water and the rolling oil in the pipeline can be realised, and the frequent switching of the water and oil pumps can be avoided.

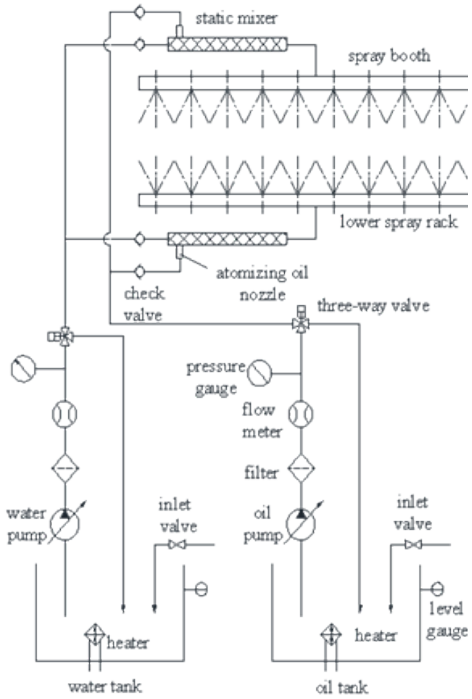

Figure 2 Schematic of the emulsion pipeline direct mixing lubrication system

3.2 Selection of the key components of the emulsion pipeline direct mixing lubrication system for double cold reduction

For the direct mixing lubrication system of double cold reduction, the key components include static mixer, atomising nozzle, water pump, oil pump, pipeline, flow metrer, pressure gauge and electric control cabinet. The result of selection directly determines whether the system can operate normally.

3.2.1 Selection of static mixer and atomising nozzle

The most important component of direct mixing lubrication system is a static mixer. In contrast to conventional agitator devices, despite the lack of moving parts in the static mixer, the initial kinetic energy provided by a momentum source, such as a pump, allows the mixed fluid to pass through a static mixing unit with a special structure. Static mixer dispersed mixing and distributed mixing of fluids of different scales is well achieved over a wide Reynolds-numbered range. Static mixers can be used in various fluid viscosities and in different flow conditions intermittently and continuously. They can make different fluids achieve uniform mixing because the mixing elements enhance the turbulence during the movement of fluid to split, stretch, rotate and merge, thereby significantly promoting convective and turbulent diffusion and resulting in a perfect radial mixing effect[9,10]. To optimise the static mixer type and atomising oil nozzle type of the direct mixing lubrication system of double cold reduction emulsion line, the emulsion particle size and ESI of the direct mixing lubrication system can reach the same performance as the high-speed stirring of the emulsion mixing tank. In combination with the actual working conditions in the on-site production of the emulsion, the injection test is conducted on the experimental device of the direct mixing lubrication system developed. According to the on-site production requirements of the secondary cold rolling mill, the emulsion injection pressure of the injection experiment is set at 5 kg, the emulsion flow rate at 10 L/min, and the frequency of the oil pump motor at 15, 30 and 50 Hz,the emulsion concentration is set at 2%–12% ,the static mixers with SV, SX and SK types are chosen(see Figure 3). And the atomising oil nozzle comprises 1/4LND types 1#, 2# and 4# models (see Figure 4). For the direct mixing lubrication system, the emulsion spray test procedure is presented as follows: 1) heating the water and rolling oil in the tank to a temperature of 60 °C which is commonly applied to the field emulsion; 2) setting the flow rate of the waterway and the oil circuit according to the required emulsion flow rate and concentration; 3) adjusting the water and oil flow rates using the return water-regulating valve and the frequency conversion motor, correspondingly; 4) adjusting the emulsion pressure and flow rate through the opening degree of the ball valve on both sides of the emulsion spray frame coordination; 5) recording water pressure and flow, oil pressure and flow and emulsion pressure; 6) emulsion nozzle and leak ball valve position emulsion sampling; 7) using a Multisizer 3 Coulter counter and a particle size analyser to detect emulsion particle diameter (resistance method); 8) detecting emulsion particle size using a BT-9300Z laser particle size distribution analyser (laser method); 9) detecting emulsion concentration using an OHRUS MB35 moisture analyser; 10) using emulsion cylinder and separatory funnel to detect emulsion ESI.In order to ensure the reliability of the experimental data, all the experimental results below are measured multiple times to take their average.

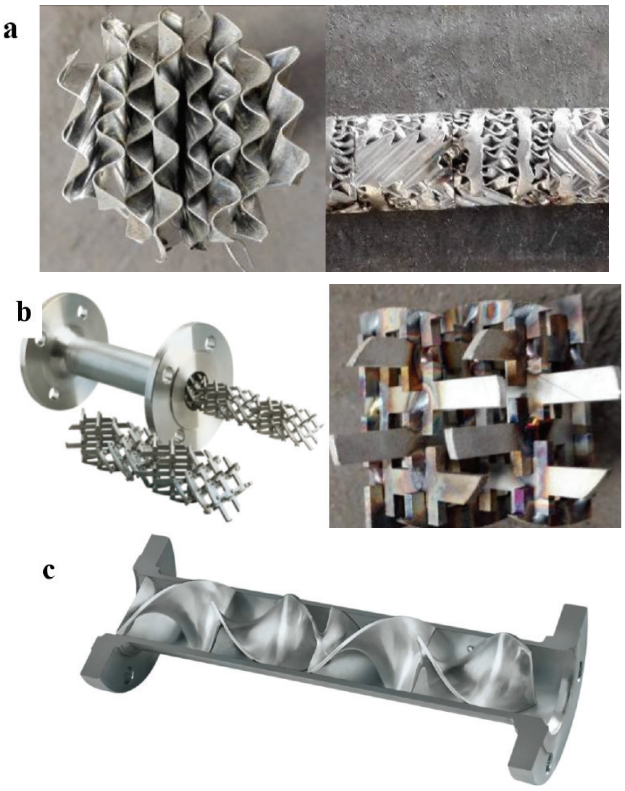

(a) Mixing unit of an SV-type static mixer.(b) Mixing unit of an SX-type static mixer.(c) Mixing unit of an SK-type static mixer.

Figure 3 Element of different static mixers

Figure 4 Atomizing oil nozzle

3.2.1.1 Comparison experiment of the different types of static mixers

SV, SX and SK-type static mixers and empty tubes without mixing units are used for comparative experiments to optimise the static mixer selection. The effects of different types of static mixers on emulsion particle size and ESI performance are analysed. Under the condition of the static mixer inlet port does not use the atomising oil nozzle to predisperse the rolling oil, the corresponding static

pressure of the different static mixers, the concentration of the emulsion, the particle size of the electric resistance method ,the particle size of the laser method and the results of ESI test are obtained (see Table 1).

Table 1 Test results of different static mixers

Number	Static mixer	Oil atomizing sprayer	Oil pump motor frequency(Hz)	Oil pressure (bar)	Emulsion concentration (%)	Resistance particle size (μm)	Laser particle size(μm)	ESI (%)
1			15	5.0	2.65	15.05	6.885	61.9
2	Empty tube	Nothing	30	5.0	6.62	15.84	7.642	67.4
3			50	5.0	10.42	17.76	8.657	70.76
4			15	5.0	2.38	14.95	6.523	70.17
5	SV	Nothing	30	5.0	6.24	15.02	7.552	72.96
6			50	5.0	10.74	16.68	8.471	74.27
7			15	5.0	2.48	14.02	6.343	73.47
8	SX	Nothing	30	5.0	5.83	14.42	6.538	76.67
9			50	5.0	10.41	15.50	7.237	80.12
10			15	5.0	2.48	14.38	6.650	73.79
11	SK	Nothing	30	5.0	6.11	14.72	7.051	72.83
12			50	5.0			10.44	16.61

Table 1 displays that, when the static mixer acts alone, with the increase in the frequency of the oil pump motor, the oil flow rate increases, the emulsion concentration increases, the oil line pressure remains unchanged, the emulsion resistance method particle size and the laser particle size diameter increase and the emulsion ESI increase. In comparison with the particle size of the emulsion that corresponds to the empty tube with ESI, the particle size of the emulsion is reduced by the static mixer, and the ESI is increased. The shear dispersion of the oil droplets in the emulsion by the static mixer is beneficial to reducing the particle size of the emulsion. The stability of the emulsion is improved. The emulsions under the action of different static mixers are SX, SK, SV and empty tubes in the order of particle size from small to large. The ESI values of the emulsions are SX, SK, SV and empty tubes in descending order. Therefore, the direct mixing lubrication system for the emulsion line must preferably be an SX-type static mixer to obtain a small emulsion particle size and a large ESI.

3.2.1.2 Comparison experiment of different types of atomised oil nozzles

Experiments are performed with three types of atomising oil nozzles, that is, 1#, 2# and 4#, to analyse the effects of different types of atomising oil nozzles on the particle size and ESI performance of the emulsion for optimising the selection of atomising oil nozzles. Under the condition of not using a static mixer, the corresponding oil pressure, emulsion concentration, electric resistance particle size, laser particle size and ESI test results of different types of oil nozzles are listed (see Table 2).

Table 2 Test results of different atomizing oil nozzles

Number	Static mixer	Oil atomizing sprayer	Oil pump motor frequency(Hz)	Oil pressure (bar)	Emulsion concentration (%)	Resistance particle size (μm)	Laser particle size (μm)	ESI (%)
1			15	5.5	2.67	15.36	6.538	78.84
2	Empty tube	4#	30	6.4	6.38	13.32	5.927	80.52
3			50	9.2	10.74	13.23	5.791	88.68
4			15	6.1	1.66	14.92	5.920	82.05
5	Empty tube	2#	30	10.9	4.61	11.72	5.592	86.71
6			50	18	7.91	10.02	4.186	91.11
7			15	7.5	1.29	11.84	5.206	92.25
8	Empty tube	1#	30	16	3.76	9.741	4.561	92.29
9			50	26.3	5.68	7.881	3.544	93.07

Table 2 reflects that the pressure drop of the rolling oil that passes through the orifice of the atomising oil nozzle determines the effect of atomising and dispersing the rolling oil in water. With the increase in the frequency of the motor, the oil flow rate and the emulsion concentration increase lead to the increasing pressure of ail. With the

decrease in the diameter of the atomising oil nozzle orifice, the pressure of the oil passage increases remarkably, the particle diameter of the electric resistance of the emulsion and the particle diameter of the laser method decrease and the ESI of the emulsion increases. Simultaneously, with the increase in the oil pressure, the efficiency of the oil pump decreases, and the flow rate of the rolling oil decreases at the same motor frequency, thereby resulting in a decrease in the emulsion concentration. For a specific type of atomising oil nozzle, the increase in emulsion concentration leads to an increase in oil–water pressure difference. However, the oil pressure cannot be increased indefinitely. The selection of atomising oil nozzle requires comprehensive consideration of oil pressure threshold and emulsion particle size. Therefore, the emulsion pipeline direct mixing lubrication system of double cold reduction mill must preferably be 2# atomising oil nozzle.

3.2.1.3 Contrast experiment of the different types of static mixer and 2# atomising oil nozzle

To optimise the selection combination of different types of static mixers and 2# atomising oil nozzles, different types of static mixers are used with 2# atomising oil nozzles to conduct the spraying experiment and determine the corresponding oil pressure difference, emulsion concentration, electric resistance particle diameter and laser particle diameter. The ESI detection results are summarised (see Table 3).

Table 3 Test results of different static mixers with 2# atomizing oil nozzle

Number	Static mixer	Oil atomizing sprayer	Oil pump motor frequency(Hz)	Oil pressure (bar)	Emulsion concentration (%)	Resistance particle size (μm)	Laser particle size(μm)	ESI (%)
1			15	6.3	1.99	14.18	5.910	83.37
2	SV	2#	30	10.8	5.67	11.64	5.339	88.48
3			50	18	8.41	9.098	4.255	92.41
4			15	6.1	1.74	13.11	5.657	86.21
5	SX	2#	30	11	5.52	10.63	5.289	89.68
6			50	18	8.5	8.105	4.103	94.88
7			15	6.1	1.91	14.56	5.806	84.06
8	SK	2#	30	10.5	5.34	10.97	5.376	89.45
9			50	18	8.34	10.18	4.273	92.24

Table 3 presents that, under the joint action of different types of static mixers and 2# atomising oil nozzles, the oil flow rate, emulsion concentration and oil–water pressure difference before and after the oil nozzle increase with the frequency of the oil pump motor. Meanwhile, the emulsion particle size decreases, and ESI increases. In comparison with the 2# atomising oil nozzle alone, the static mixer can perform secondary shear dispersion on the large particle oil droplets dispersed in the atomising oil nozzle, thus slightly reducing the particle size of the emulsion and increasing the ESI. Among them, the emulsion of the SX static mixer and the 2# atomising oil nozzle has smaller particles and larger ESI than the synergistic effect of the SK, SX static mixer and the 2# atomising oil nozzle. Therefore, an SX-type static mixer is recommended to combine with a 2# atomising oil nozzle.

3.2.2 Design selection of water and oil pumps

According to the process characteristics of the emulsion pipeline direct mixing lubrication system of double cold reduction mill, the flow rate of the emulsion in the rolling process must be adjusted rapidly in a wide range, thereby requiring the flow of deionised water and rolling oil rapidly be adjusted over a wide range. And variable pumps are required for water and oil circuits. Simultaneously, the flow rate and concentration of the emulsion during the rolling process must be precisely controlled, and the continuous supply of deionised water and rolling oil must be ensured. The gear pump is a rotary pump that relies on the change and movement of the working volume formed between the pump cylinder and the meshing gear to transport or pressurise the liquid. The pressure of the discharge port completely depends on the resistance at the pump outlet. Furthermore, the flow is smooth, and the pulsation is small. The utility model has the advantages of simple structure, low price, low maintenance rate, good repeatability and accurate measurement. Therefore, the water and oil pumps must give priority to the gear metering pump. The physical object is demonstrated in Figure 5 (see Figure 5).

In the production process of double cold reduction, the maximum adjustment range of the emulsion flow of the upper and lower spray racks is 5–20 L/min. According to the technical requirements of water flow (10–40 L/min) and pressure (3–10 bar), the pump is C4/481. In addition, a stainless steel gear metering pump, import and export size G1, configuration QABP132S6A 3.0 kW-6P-B3 model ABB variable frequency motor, a maximum speed of 980 rpm, a gear metering pump single-rotation displacement of 48.1 cc/rev and a maximum speed rated flow of 47.0 L/Min are adopted. Under the same motor speed, the efficiency of the gear metering pump decreases with the increase in pressure. In accordance with the 85% efficiency at 10 bar, the actual flow rate of the maximum speed can reach 40.0 L/min, thereby satisfying the requirements of maximum oil flow and pressure.

According to the technical requirements of oil flow rate of 0.5–3.0 L/min and pressure of 5–32 kg, C2/475 stainless steel gear metering pump, import and export size G1/2, configure QABP90S6A 0.75 kW-6P-B3 type ABB inverter motor, a maximum speed of 980 rpm, a single-rotation displacement of the gear metering pump of 4.75 cc/rev and a maximum speed rated flow of 4.6 L/min are selected. Under the same motor speed, the efficiency of the gear metering pump decreases with the increase in pressure. In accordance with the efficiency of 75% at 32 kg, the actual flow rate of the maximum speed can reach 3.45 L/min, thus satisfying the requirements of maximum oil flow and pressure.

Figure 5 Gear metering pump and variable frequency motor

3.2.3 Pipe design selection

The chemical pipeline design guidelines indicate that the pipe diameter must be determined in accordance with the flow rate, nature and pressure loss of the pipeline[11]. The predetermined flow rate method is used to select the pipe diameter which can be calculated as

$$D = \sqrt{\frac{200Q_{fluid}}{3\pi v_{fluid}}} \quad (1)$$

where D represents the pipe inner diameter (mm), Q_{fluid} is the volume flow of the medium in the tube (L/min), and , v_{fluid} is the average flow rate of the medium in the tube (m/s).

The flow rate range of the common medium in the pipeline is recommended, as summarised (see Table 4). The water flow rate is set as 1 m/s, the oil flow rate is 0.5 m/s, and the pipe diameter is selected according to the pipeline flow demand of the emulsion direct mixing system, as presented (see Table 5).

3.2.4 Flow metrer selection

The deionised water flow range of water path is 10.0–40.0 L/min; the water path uses a liquid turbine flow metrer, whose model is ECLWGY10CLC2SSN, with DN10 calibre, on-site display, 24 VDC power supply, two-wire 4–20 mA output and G1/2 threaded connection (see Figure 6).

Figure 6 Turbine flow meter for a water pipeline

Table 4 Recommendation velocity range of common fluid

medium	Working condition or pipe diameter range	Flow rate range (m/s)
Water and liquid with similar viscosity	0.1~0.3 MPa	0.5~2
	≤1MPa	0.5~3
	≤8MPa	2.0~3.0
	≤20~30MPa	2.0~3.5
Oil and liquid with higher viscosity Viscosity<0.05 Pa·s	DN25	0.5~0.9
	DN50	0.7~1.0
	DN100	1.0~1.6
Oil and liquid with higher viscosity Viscosity<0.1 Pa·s	DN25	0.3~0.6
	DN50	0.5~0.7
	DN100	0.7~1.0
	DN200	1.2~1.6

Table 5 Pipeline design and selection of emulsion pipeline direct mixing lubrication system

Pipeline	flow (L/min)	Minimum diameter(mm)	Maximum diameter(mm)	Pipe diameter selection
Waterway road	10.0~40.0	14.57	29.13	DN25
Waterway branch	5.0~20.0	10.30	20.60	DN20
Oil road	0.5~3.0	4.61	11.28	DN10
Oil road branch	0.25~1.5	3.26	7.98	DN8

The turbine flow metrer is based on the principle of torque balance and belongs to the speed flow metrer. This flow metrer has the characteristics of simple structure, lightweight, high precision, favourable repeatability, responsiveness and convenient installation and maintenance. When the fluid flows through the turbine flow sensor housing, the momentum of the fluid causes the blade to have a rotational moment because the blade of the impeller has a certain angle with the flow direction, and the blade rotates after overcoming the friction torque and the fluid resistance. After the torque balance, the rotational speed is stable at a certain degree. The rotation speed is proportional to the flow rate under this condition. The blade is magnetically permeable and is thus in the magnetic field of the signal detector. The rotating blade cuts the magnetic line of force and periodically changes the magnetic flux of the coil. Consequently, the electric pulse signal is induced at both ends of the coil. The signal is amplified and shaped by the amplifier to form a continuous rectangular pulse wave with a certain amplitude, which can be transmitted to the display instrument to show the instantaneous flow or total amount of the fluid. At the upstream end of the turbine flow metrer, at least 20 times of the nominal flow can be installed. For straight pipe lengths of the diameter, the downstream end shall be not less than 5 times the straight pipe section of the nominal diameter.

The rolling oil flow range of the oil passage is 0.5–3.0 L/min, and the oil path uses an elliptical gear flow metrer, whose model is ESFD2091, with DN8 calibre, external display instrument, 24 VDC power supply, pulse output and G1/4 threaded connection(see Figure 7). The elliptical gear flow metrer is a typical volumetric flow with a simple structure, reliable use and high accuracy and has no special requirements on the flow field in the inlet and outlet pipes. The viscosity and flow ranges of the measured medium are wide.

Figure 7 Elliptical gear flow meter for an oil pipeline

The elliptical gear flow metrer uses a liquid flow to push a pair of interlocking gears. Each gear cavity has a fixed volume, and the flow rate of the liquid that flows through each revolution of the gear is constant (see Figure 8). The gear speed is extracted. The sensor sends a sync pulse count which can be sent directly to an external receiving component to calculate the fluid flow rate based on the flow metrer for each pulse. The elliptical gear flow metrer can be directly installed on the pipeline, and the flow metrer can be fixed through the pipeline. If the pipeline is a hose, then it can be fixed through the screw hole below; the straight pipe section is required to be larger than 10 times the nominal diameter of the pipeline, and the rear straight section is 5 times the nominal diameter of the pipe.

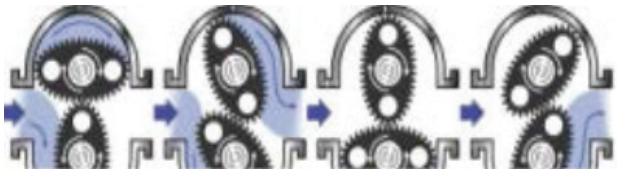

Figure 8 Working mechanism of the elliptical gear flow meter

3.2.5 Pressure gauge selection

A pressure gauge refers to a metrer that uses a spring element as a sensitive component to measure and indicate a pressure higher than the ambient pressure. The pressure gauge is deformed by the elastic deformation of the sensitive component in the watch, and the pressure deformation is transmitted to the pointer by the conversion mechanism of the movement inside the watch. The pointer turns to display the pressure. Sufficient space must be left in accordance with the magnitude of the measured pressure and the pressure change when selecting the gauge range to ensure that the elastic element can work reliably within the safe range of elastic deformation. Therefore, the upper limit of the pressure gauge must be higher than the maximum possible pressure value in the process. When measuring stable pressure, the maximum working pressure must not exceed 2/3 of the upper limit of measurement; when measuring pulsating pressure, the maximum working pressure must not exceed half of the upper limit of measurement; when measuring high pressure, the maximum working pressure must not be more than 3/5 of the upper limit of the measurement. The minimum value of the measured pressure must not be less than 1/3 of the upper limit of the meter measurement.

In the emulsion pipeline direct mixing lubrication system, the water pressure range is 3–10 bar, and the oil pressure range is 5–32 bar. Therefore, the selected water pressure gauge range is 0–1.0 MPa, and the oil pressure gauge range is 0–4.0 MPa (see Figure 9).

Figure 9 Pressure gauge of water and oil pipeline

3.2.6 Design selection of electric control cabinet

According to the requirement of online adjustment of emulsion flow rate and concentration during the rolling process of the secondary cold rolling mill, the oil and water pumps adopt variable frequency motor, the electric control cabinet is equipped with 380 V power source to drive the

variable frequency motor of water and oil pumps, and 24 V DC switching power supply is the water and oil circuit. The flow metrer is powered, and the frequency converter is used to control the rotational speed of the water pump and the oil pump variable frequency motor. In addition, the flow rate of the deionised and rolling oil is adjusted online to realise the online control of the emulsion flow rate and concentration during the rolling process. A physical diagram of the electric control cabinet is displayed in Figure 10 (see Figure10). The main equipment configuration is presented (see Table 6).

Figure 10 Electric control cabinet

Table 6 Main equipment configuration of electric control cabinet

code	name	Model / Specification	Quantity
1	Distribution Cabinet	600*500*250	1
2	Main switch	IC65 3P 25A	1
3	Branch switch	IC65 3P 16A	2
4	AC contactor	EASYPACT 2510	1
5	AC contactor	EASYPACT 1810	1
6	Frequency converter	ACS510-01-04A1-4	2
7	Inverter control panel	ABB	2
8	Cooling fan		1
9	emergency button		1
10	Knob		2
11	pilot lamp		3
12	Switching power supply	ABL2REM24045H	1

4 Engineering application of the emulsion pipeline direct mixing lubrication system of double cold reduction mill

4.1. Equipment renovation and installation of the emulsion pipeline direct mixing lubrication system

According to the equipment conditions of the emulsion pipeline direct mixing lubrication system of double cold reduction mill unit of a tinplate factory, the emulsion of the existing emulsion direct injection system mixing tank is emptied, and deionised water is added and used as the water tank for direct mixing lubrication system of double cold reduction. The emulsion spray pump is used as the water pump of the emulsion pipeline direct mixing lubrication system, and the speed of the water pump is adjusted by the frequency converter to realise the online real-time adjustment of the emulsion flow rate. The emulsion pipeline, flow metrer, pressure gauge and three-way valve equipment are used as the waterway equipment of the direct mixing lubrication system. The connecting hose, waterway check valve and static mixer are added to the emulsion pipeline before the upper and lower spray racks. Thus, the pipeline and equipment of the emulsion mixing tank of the original emulsion direct injection system to the spray rack are fully utilised, and the difficulty and cost of the transformation are reduced. An oil circuit system is added outside the rack to supply rolling oil to the static mixer. The rolling oil is heated to a specified temperature in the fuel tank. The oil pump on the moving trolley is passed through a flow metrer, a pressure gauge, a connecting hose and a check valve. The oil nozzle transports the rolling oil to the static mixer. During the rolling process, the motor speed is adjusted in accordance with the production requirements of the frequency converter to adjust the flow rate of the oil circuit, real-time regulation of the emulsion concentration. Equipment transformation and installation plan for the double cold reduction unit emulsion pipeline direct mixing lubrication system is shown(see Figure 11).

4.2 The emulsions characteristic comparsion of emulsion pipeline direct mixing lubrication system and the traditional direct aplication lubrication system

The emulsion pipeline direct mixing lubrication system and the traditional direct aplication lubrication system are configured with different emulsion concentrations to explain the feasibility of the emulsion pipeline direct mixing lubrication system to replace the traditional direct aplication lubrication system in the field. The corresponding emulsion resistance particle size, laser particle size, ESI and other characteristic parameters are depicted in Figure 12 (see Figure 12).

For the traditonal direct injection system, the emulsion is disposed in the mixing tank, and the rolling oil is cut and dispersed in the water by the blades rotated by an agitator, thereby reducing the particle size of the emulsion and increasing the ESI. Simultaneously, the rolling oil droplets in the emulsion collide with one another in the mixing tank, thus increasing the particle size of the emulsion and decreasing the ESI. Therefore, with the increase in the concentration of the emulsion, the rolling oil in the mixing tank requires additional cutting times for the mixer to form

the original particle size, and the probability that the rolling oil particles of the emulsion collide with one another increases,thus leading to the increase of emulsification particle size, whereas the ESI decreases. For the emulsion direct mixing lubrication system, under the joint action of the SX static mixer combined with the 2# atomising oil nozzle, the increase in the emulsion concentration must increase the rolling oil flow rate given the 2# atomising oil nozzle. The diameter of the nozzle hole is fixed, and the increase in the flow rate of the rolling oil leads to an increase in the pressure of the oil passage. Moreover, the pressure drop of the rolling oil through the atomising oil nozzle is increased, and the shearing predispersion capability of the atomising oil nozzle to the rolling oil is enhanced. The rolling oil can be predispersed in deionised water with small particles. Therefore, with the increase in emulsion concentration, the particle size of the emulsion decreases, and ESI increases. The emulsion and tank mixing and their mixing emulsion characteristics exhibit the opposite trend with the emulsion concentration. When the emulsion concentration is low, the direct mixing of the pipeline is improved with respect to the mixing tank. Thus, the lubrication performance is improved, and the stability is lowered. When the emulsion concentration is high, the lubricating performance of the direct mixing of the pipeline with respect to the mixing tank is lowered, and the stability is improved. Overall, the emulsion pipeline direct mixing lubrication system has the same range of resistance method particle size, laser method particle size and ESI as the traditional direct aplication lubrication system.Therefore, through the optimal selection of key equipment, such as static mixer and atomising oil nozzle, for the emulsion pipeline direct mixing lubrication system, the emulsion pipeline direct mixing system can satisfy the requirements of emulsion performance well on the on-site production of secondary cold rolling mills.

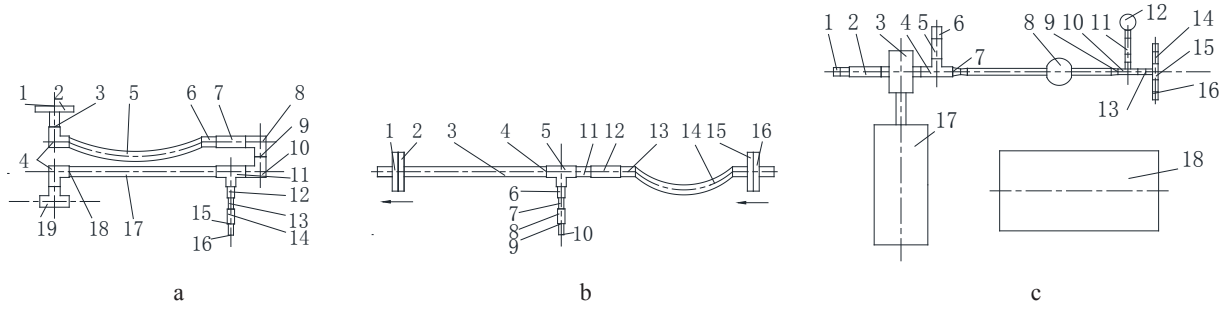

(a) Upper static mixer pipeline transformation plan.(1)Water intake,(2)Flange,(3)Inner and outer wire joint G3/4,(4)Inner and outer wire joint elbow,(5)Hose,(6)Interface G3/4,(7)Check valve,(8)Outer wire elbow,(9)External wire joint G3/4,(10)Inner and outer wire joint elbow,(11)Reducing tee,(12)oil-atomising sprayer,(13)Interface G3/4,(14)One-way valve,(15)Inner and outer wire joint G1/4,(16)Oil inlet (connected to G1/4 hose),(17)Upper static mixer,(18)Inner and outer wire joint G3/4,and(19)Emulsion outlet.(b) Lower static mixer pipeline transformation installation plan. (1)Emulsion outlet (Go down the spray rack) ,(2)Flange, (3)Lower static mixer,(4)Inner and outer wire joint G3/4 ,(5)Reducing tee ,(6)oil-atomising sprayer ,(7)Interface G1/4 ,(8)One-way valve ,(9)Interface G1/4 ,(10)Oil inlet connected to the G1/4 hose 10 m,(11)Interface G3/4,(12)One-way valve,(13)Interface G3/4,(14)hose 800 mm,(15) Flange,(16)Hot water inlet. (c) Oil circuit equipment installation plan. (1)Oil inlet hose,(2)Filter,(3)Gear pump,(4)Three-way valve,(5) Ball valve,(6)Return hose,(7)Interface G1/2,(8)Flow metrer,(9)Interface G1/4,(10)Three-way valve,(11)Needle valve,(12)Pressure gauge,(13)Interface G1/4,(14)Ball valve,(15)Three-way valve,(16)Oil hose,(17)Inverter motor,(18)Electric control cabinet

Figure 11 Modification and installation position of the emulsion pipeline direct mixing lubrication system

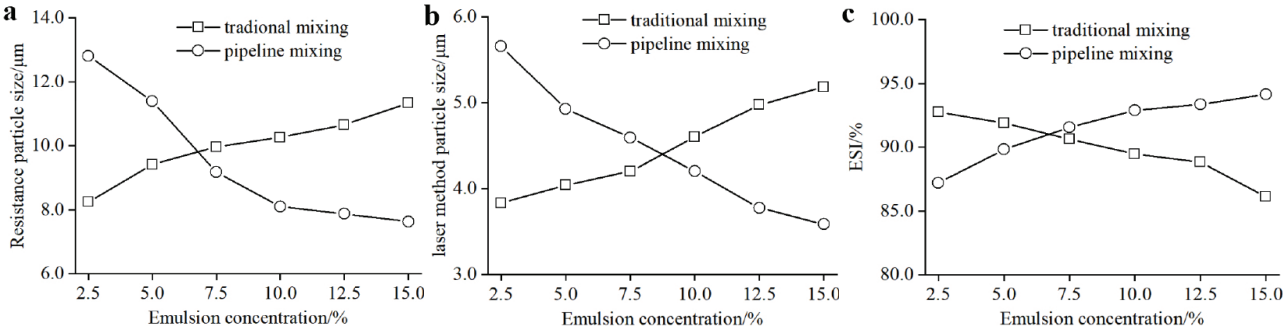

(a) Resistance particle size. **(b)** Laser particle size. **(c)** Emulsion ESI.

Figure 12 Comparison of traditional mixing and pipeline mixing by mixing emulsion property

4.3 Field application effect of emulsion pipeline direct mixing lubrication system

A 1220 double cold reduction unit of a steel enterprise with a set of emulsion pipeline for direct mixing lubrication is adopted by using the design scheme developed in this study to improve the rolling stability and product quality

of the unit, reduce the rolling energy consumption and fuel consumption cost and apply it to production practices. After applying the lubrication system and after 6 months of on-site production statistics, the average fuel consumption per ton of steel is reduced by 9.6%, and the overall cost of rolling energy consumption and fuel consumption per ton of steel is reduced by 10.7%. Furthermore, the thickness of the strip section is reduced by 19.3%, and the incidence of plate shape quality defects is decreased by 25.6%. These conditions create considerable economic benefits for the unit. To analyse the usage effect of the emulsion pipeline direct mixing lubrication system, the TH580 steel grade of the typical specification is selected on the site of trouble cold reduction, and the conventional direct injection and the emulsion pipeline direct mixing lubrication system are used for on-site rolling test. During the rolling process, the flow rate and concentration of the emulsion in the traditional direct aplication lubrication system are fixed. The direct mixing lubrication system of the emulsion is set in accordance with the change in the rolling speed of the emulsion flow and concentration comprehensive optimisation technology. In addition,authors compared the traditional direct aplication lubrication system with the emulsion pipeline direct mixing lubrication system,analysing the rolling pressure, energy consumption, oil consumption and total fuel consumption cost. The steel plate thickness and shape measurement data are also comparatively analysed. The thickness and shape quality of the traditional direct injection lubrication system in the cold rolling mill and the direct hybrid lubrication system of the emulsion pipeline fluctuate. The rolling process parameters are listed (see Table 7).

Table 7 Rolling parameters of field experiment coils of double cold rolling mill

Steel grade	TH580
Strip width$B$/m	0.847
Inlet thickness$H$/mm	0.201
Outlet thickness h/mm	0.150
Entrance yield strength σ_{s0}/MPa	320
Export yield strength σ_{s1}/MPa	580
Post-tension stress σ_0/MPa	118
Pre-tension σ_1/MPa	168

4.3.1 Comparison of energy consumption and fuel consumption parameters

The TH580 steel grade which adopts the traditional direct aplication lubrication system and the emulsion pipeline direct mixing lubrication system obtains disparate result, such as the emulsion flow setting value, emulsion concentration setting value, rolling pressure, rolling energy consumption and fuel consumption. (see Figure 13).

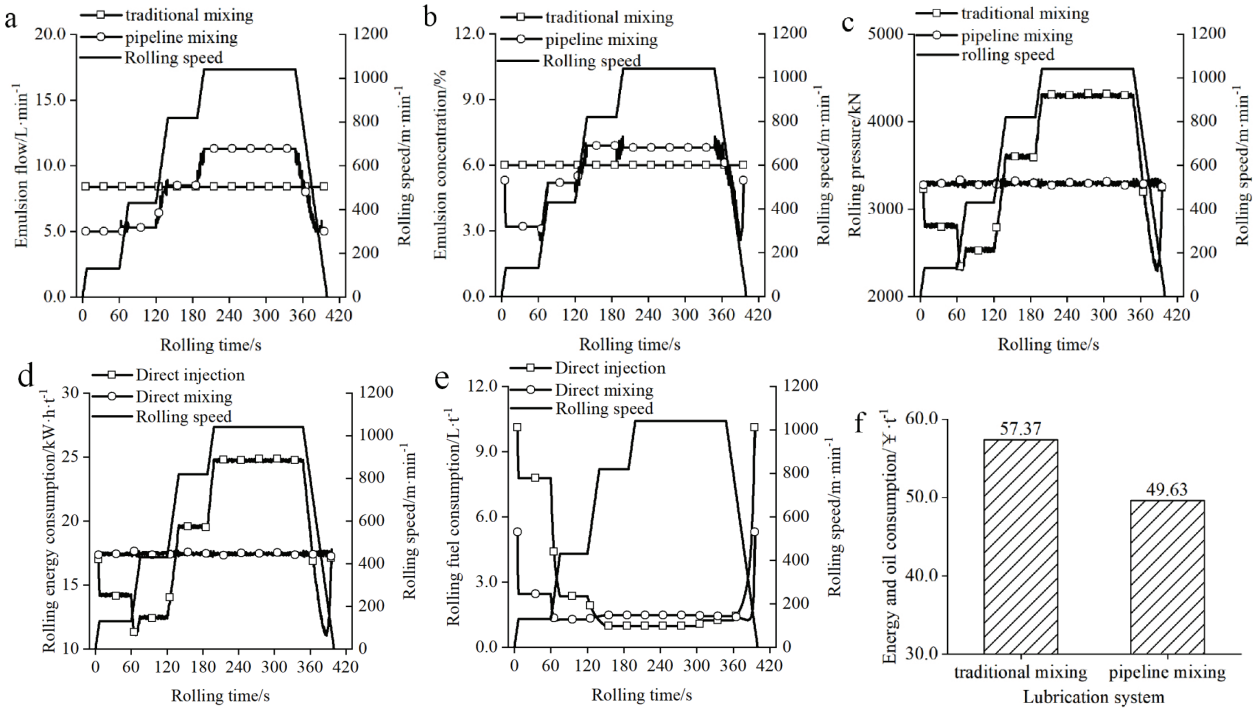

(a) Emulsion flow.(b) Emulsion concentration.(c) Rolling pressure.(d) Rolling energy consumption.(e) Rolling fuel consumption. (f) Rolling energy consumption and total fuel consumption cost.

Figure 13 Comparison of the TH580 steel rolling parameters between traditional direct application and the emulsion pipeline direct mixing lubrication system.

Figure 13 displays that the rolling pressure fluctuation is reduced from 1780 kN to 50 kN at different rolling speeds after applying the emulsion pipeline direct mixing lubrication system of double cold reduction mill unit (see Figure 13). The stability of the rolling pressure is significantly improved, whereas the total rolling energy and

fuel consumption are considerably reduced.

4.3.2 Strip thickness and shape quality comparison

During the on-site rolling test of double cold reduction, the thickness and shape of the strip are measured by the thickness gauge of the rack outlet and the shape metrer, respectively. The thickness and shape data of the on-site rolling test are derived, and the thickness and plate are compared. The shape fluctuation, the traditional direct injection lubrication system and the emulsion pipeline direct mixing lubrication system corresponding to the strip thickness deviation comparison are presented in Figure 14 (see Figure 14). Moreover, the strip shape value comparison is illustrated in Figure 15 (see Figure 15), and the strip shape quality is demonstrated in Figure 16 (see Figure 16).

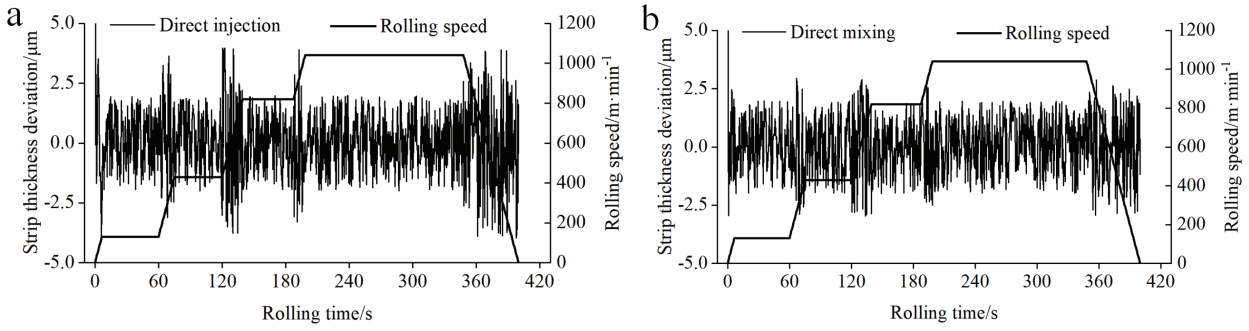

(a) Traditional direct injection (b) Direct mixing

Figure 14 Comparison of the TH580 steel thickness deviation between traditional direct application and direct mixing lubrication system

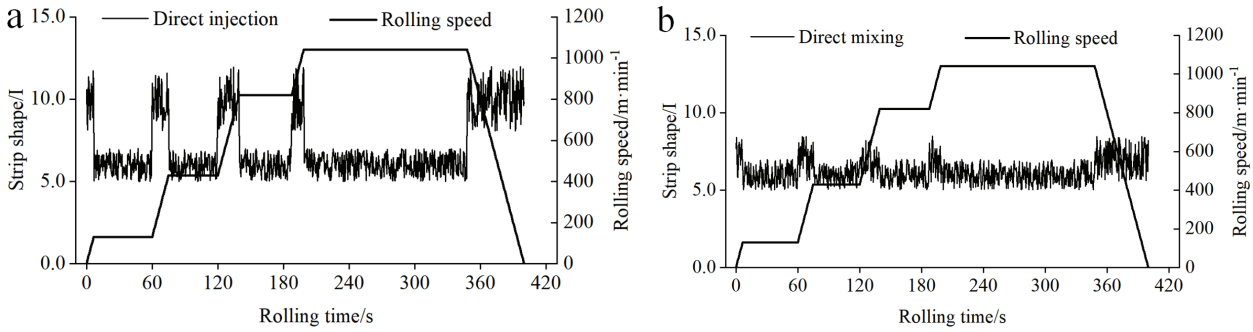

(a) Traditional direct injection (b) Direct mixing

Figure 15 Comparison of the TH580 steel flatness between traditional direct application and direct mixing lubrication system

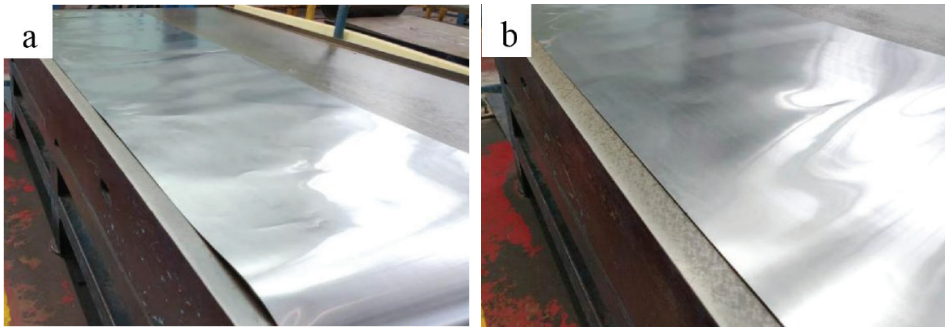

(a) Traditional direct injection (b) Direct mixing

Figure 16 TH580 steel flatness with traditional direct application and direct mixing lubrication system

Figures 14–16 depict that the flow rate and concentration of the emulsion in the traditional direct aplication lubrication system remain unchanged with the rolling speed; consequently, the rolling pressure fluctuates significantly during the lifting speed, and the strip thickness deviation and plate shape value fluctuate more than those in the steady speed stage. After applying the direct mixing lubrication system of the emulsion pipeline, the thickness deviation of the strip and the fluctuation of the plate shape are reduced with the decrease in the rolling

pressure fluctuation during the lifting speed. Furthermore, the thickness stability of the strip is improved, and the plate shape value is lowered.

5 Conclusion

(1) A direct mixing lubrication system suitable for emulsion pipeline is developed by fully considering the equipment and process characteristics of double cold reduction and analysing the technological characteristics of the traditional emulsion direct injection lubrication system. The selection of key components of the emulsion pipeline direct mixing lubrication system is completed in eight aspects, namely, selecting a static mixer and an oil mist nozzle, water and oil pump designs, pipeline design, flow metrer, pressure gauge and electric control cabinet. And forms a complete set of the emulsion pipeline direct mixing lubrication system of double cold reduction mill, which is applied to the production practice of a 1220 double cold reduction unit.

(2) A comparison of the emulsion characteristics of the emulsion pipeline direct mixing lubrication system and the traditional direct injection lubrication system with tank mixing shows that their characteristics have opposite trends with emulsion concentration. When the emulsion concentration is low, the lubricating properties of the pipeline lubricants is directly mixed relative to the mixing tank mixing emulsion are improved and the stability is reduced; when the emulsion concentration is high, the lubricating properties of lubricants are reduced and the stability is improved. Overall, the range of resistance method particle size, laser method particle size and ESI of direct mixing of the pipeline relative to mixing mixing emulsion in the mixing tank is equivalent and is adapted to the demand for the emulsion performance in the on-site production of double cold reduction mill.

(3) With the emulsion pipeline direct mixing lubrication system of double cold reduction mill, after field application of 1220 double cold reduction mill and after 6 months of on-site production data statistics, the average fuel consumption per ton of steel is reduced by 9.6%, and the energy consumption per ton of steel is also reduced. The comprehensive cost of fuel consumption is reduced by 10.7%, and the length of the strip thickness of the strip section is reduced by 19.3%. Moreover, the incidence of sheet shape quality defects is reduced by 25.6%. These conditions create considerable economic benefit for the unit.

Author Contributions: Zhen-hua BAI contributed to the conception of the study; Hang-zhe DONG performed the experiment; Ya-zhen ZHANG contributed significantly to analysis and manuscript preparation; Wan-tong HU performed the data analyses and wrote the manuscript; Yan-yan ZHANG helped perform the analysis with constructive discussions.

Conflict of Interest: The authors declare that there is no conflict of interest regarding the publication of this paper.

Acknowledgments: This work is supported by the Natural Science Foundation of Hebei Province (Grant No. E20160203385) and the Heavy Machinery Collaborative Innovation Program (Grant No. ZX01-20140400-05). A few experiments were made in Baosteel Tinplate Plant. The authors gratefully acknowledge the technical support of Baosteel.

References

[1] BAI Zhen-hua; SONG He-chuan. Research development of double cold reduction equipment and process. Journal of Plasticity Engineering, 2016, 23(06): 87-93.

[2] ZHANG Hong-bo; FENG Xiao-yong. Research progress and application status of double reduced materials for tin-plate. Hebei Metallurgy, 2017, (04): 1-5.

[3] JI Jiang; HU Hong. Development and application of skin pass and double cold-reduced mill processing for high quality ultra-thin uncoated tin-plated sheet. Steel Rolling, 2018, 35(01): 49-51.

[4] CUI Ya-ya; LI Bo-yang. Comprehensive optimization setting of emulsion flowrate and concentration for double cold reduction mill. Iron and Steel, 2018, 53(02): 40-44.

[5] WEI Li-qun; DAI Zhi-fang. Research of vibration and strategy in high speed cold-rolling mill. Journal of Mechanical Engineering, 2016, 52(11): 88-94.

[6] Kimura Y; Fujita N. High-speed rolling by hybrid-lubrication system in tandem cold rolling mills. Journal of Materials Processing Technology, 2015, 216: 357-368.

[7] Das P K; Legrand J. Drop Breakage Model in Static Mixers at Low and Intermediate Reynolds Number. Chemical Engineering Science, 2005, 60(1): 231-238.

[8] LI Xiu-jun; CUI Ya-ya. Model of plate-out oil film thickness on strip surface of direct application system in double cold rolling and its influence factors. Journal of Plasticity Engineering, 2018, 25(4): 285-290.

[9] WANG Xiu-gang; GUO Wa-li. Experimental and numerical study on liquid-liquid dispersion in static mixer. Journal of Chemical Industry and Engineering, 2012, 63(3): 767-774.

[10] Lobry E; Theron F. Turbulent liquid–liquid dispersion in SMV static mixer at high dispersed phase concentration. Chemical Engineering Science, 2011, 66(23): 5762-5774.

[11] XU Bao-dong. Chemical Pipeline Design Manual, 1st ed. Chemical Industry Press: Beijing, China, 2011, 7-8.

Viser Technology Pte. Ltd.
Mechanical Engineering Science
doi: 10.33142/mes.v2i1.2620

Research Article Open Access

Analytic solution for size-dependent behaviors of micro-beam under forced vibration

Shuai WANG, Zhiyong WANG, Feifei WANG, Bo ZHOU*, Shifeng XUE

College of Pipeline and Civil Engineering, China University of Petroleum (East China), Qingdao 266580, P.R. China

***Corresponding Author:** Bo ZHOU, Email: zhoubo@upc.edu.cn*

Abstract:
This paper focuses on the size-dependently mechanical behaviors of a micro-beam under forced vibration. Governing equations of a micro-beam under forced vibration are established by using the modified couple stress theory, Bernoulli-Euler beam theory and D'Alembert's principle together. A simply supported micro-beam under forced vibration is solved according to the established governing equations and the method of separation of variables. The dimensionless deflection, amplitude mode and period mode are defined to investigate the size-dependently mechanical behaviors of a micro-beam under forced vibration. Results show that the performance of a micro-beams under forced vibration is distinctly size-dependent when the ratio of micro-beam height to material length-scale parameter is small enough. Both frequency ratio and loading location are the important factors that determine the size-dependent performance of a micro-beams under forced vibration.

Keywords: *micro-beam; forced vibration; size effect, modified couple stress theory; Bernoulli-Euler beam theory.*

1 Introduction

Microbeams have been widely employed in micro-electro-mechanical systems (MEMS) [1-3]. There have been many applications of microbeams, such as microscale sensors[4-6], microscale actuators[7-8], and microswitch[9].

The experimental results[10-11] have revealed the size-dependent of material behavior in micron scale. However, the classical continuum mechanics theories couldn't describe the phenomenon. Therefore strain gradient and couple stress theory have been applied to study size effect of micron devices[12-16]. In these theories, internal material length scale parameters were introduced. Ansari et al.[17] studied the bending, buckling and free vibration responses of functionally graded Timoshenko beams based on the theory of strain gradient elasticity. They established a size-dependent beam model with five additional material length-scale parameters using Hamilton's principle. Liang et al.[18] built a new Bernoulli-Euler beam model employing a simplified strain gradient elasticity theory and analytically solved static bending of cantilever beams, buckling and free vibration of simply supported beams. Alashti et al.[19] derived the governing equations of Bernoulli-Euler beams by using the variational formula and Hamilton's principle, based on the couple stress model proposed by Hadjesfandiari et al.[16], and discussed the problems of static bending and free vibration of Bernoulli-Euler beams with different boundary conditions.

Yang et al.[20] presented a modified couple stress theory (MCST) based on couple stress theory. This theory revealed that couple stress tensor was symmetric and conjugated with symmetric curvature tensor to total strain energy of the system. In addition, only one material length-scale parameter was used in the MCST, thus this theory was utilized more widely. Park et al.[21] provided a variational formulation for the MCST using the principle of minimum total potential energy. Park et al.[22] studied bending of Bernoulli-Euler microbeam on the basis of the MCST. The governing equation and boundary condition were developed using the principle of minimum total potential energy. Ma et al.[23] developed a micro Timoshenko model using Hamilton's principle and variational formulation based on the MCST. Kong et al.[24] obtained the dynamic equilibrium governing equation, initial condition and boundary condition of Bernoulli-Euler micro-beam combining the basic equation of MCST with Hamilton principle. The boundary value problem of simply supported beam and cantilever beam were solved, and size effect on natural frequencies of beams was studied. Mohammad-Abadi et al.[25] analyzed free vibration of composite

laminated beams using the modified couple stress theory. The governing equation and boundary condition were obtained by applying Hamilton's principle. The differences between Bernoulli -Euler, Timoshenko and Reddy beam models were studied. Dehrouyeh-Semnani et al.[26] obtained Bernoulli-Euler beam model and Timoshenko beam model based on modified couple stress. The effects of size-dependent shear deformation on static bending, buckling and free vibration characteristics of micro-beams were studied.

In summary, many works have been published to investigate the effects of size-dependent on static bending, bulking and free vibration of micro-beams. However the works about the size-dependent behaviors of a micro-beam under forced vibration are few. The objective of this paper is to investigate the size-dependent behaviors of a micro-beam under forced vibration. In Section 2, the modified couple stress theory is briefly introduced for considering the size effect of a micro-beam. In Section 3, the governing equations for a micro-beam under forced vibration are established by using the MCST and D'Alembert's principle together. In Section 4, a simply supported micro-beam under forced vibration is solved based on the method of separation of variables. In Section 5, the size-dependent mechanical behaviors of a micro-beam under forced vibration are numerically investigated. Finally, several important conclusions related to the size-dependent mechanical behaviors of a micro-beam under forced vibration are summarized in Section 6.

2 Modified couple stress theory

According to the MCST, the constitutive equation of an elastomer reads as

$$\sigma_{ij} = \lambda \varepsilon_{kk} \delta_{ij} + 2G\varepsilon_{ij} \tag{1}$$

$$m_{ij} = 2l^2 G \chi_{ij} \tag{2}$$

where l is the length-scale parameter; σ_{ij} and ε_{ij} are stress tensor and strain tensor, respectively; m_{ij} and χ_{ij} are deviatoric part of couple stress tensor and symmetric curvature tensor, respectively; λ and G are Lame's constants expressed as

$$\lambda = \frac{E\mu}{(1+\mu)(1-2\mu)} \tag{3}$$

and

$$G = \frac{E}{2(1+\mu)} \tag{4}$$

respectively; E and μ are elastic modulus and Poisson's ratio, respectively; l is the length-scale parameter, a material constant related to the size effect.

The geometric equation of an elastomer reads as

$$\varepsilon_{ij} = \frac{1}{2}\left(u_{i,j} + u_{j,i}\right) \tag{5}$$

$$\chi_{ij} = \frac{1}{2}\left(\theta_{i,j} + \theta_{j,i}\right) \tag{6}$$

where u_i and θ_i are the displacement tensor and rotation tensor, respectively. The rotation tensor can be expressed as

$$\theta_i = \frac{1}{2} e_{ijk} u_{k,j} \tag{7}$$

where e_{ijk} is the third order alternating tensor.

3 Governing equations micro-beam under forced vibration

3.1 Formulations on basic variables

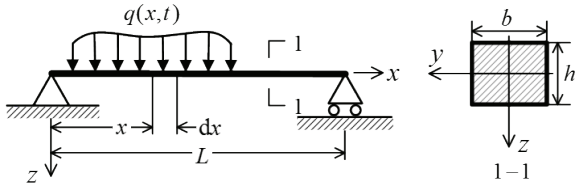

Figure 1 Bernoulli-Euler micro-beam subjected to transverse force under the Cartesian coordinate system x, y, z, where q(x, t) is the line density of transverse force and t stands for time.

According to the theory of Bernoulli-Euler beam, the displacement field of a beam can be expressed as

$$u = -z\frac{\partial w(x,t)}{\partial x}\ ,\ v = 0\ ,\ w = w(x,t) \tag{8}$$

where u, v and w are the displacement components in directions x, y and z respectively. Substituting (8) into the geometric equation (5), one formulates the nonzero strain component of a Bernoulli-Euler beam as

$$\varepsilon_{xx} = -z\frac{\partial^2 w}{\partial x^2} \tag{9}$$

Substituting (8) into the rotation tensor expression (7), one has the rotation components of a Bernoulli-Euler beam

$$\theta_x = 0,\ \theta_y = -\frac{\partial w}{\partial x}\ ,\ \theta_z = 0 \tag{10}$$

Substituting (10) into the geometric equation (6), one formulates the nonzero curvature components of a Bernoulli-Euler beam as

$$\chi_{xy} = \chi_{yx} = -\frac{1}{2}\frac{\partial^2 w}{\partial x^2} \tag{11}$$

Using the nonzero strain component (9) and the constitutive equation (1), one expresses the nonzero stress components of a Bernoulli-Euler beam as

$$\sigma_{xx} = -(\lambda + 2G) z\frac{\partial^2 w}{\partial x^2}\ ,\ \sigma_{yy} = \sigma_{zz} = -\lambda z\frac{\partial^2 w}{\partial x^2} \tag{12}$$

where λ and G are Lame's constants defined by (3) and (4), respectively. Similarly using the nonzero curvature components (11) and the constitutive equation (2), one expresses the nonzero couple stress components of a Bernoulli-Euler beam as

$$m_{xy} = m_{yx} = -Gl^2\frac{\partial^2 w}{\partial x^2} \tag{13}$$

3.2 Motion differential equation

In order to establish the motion differential equation of the beam in Fig 1, we isolate an infinitesimal segment with a length dx and plots its free body diagram in Figure 2. In the

free body diagram, Q and M are shear force and bending moment, respectively; q and f_i is the transverse force and inertial force per unit length, respectively.

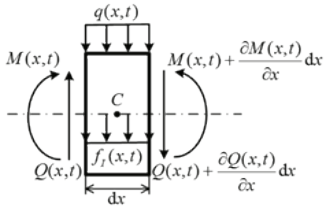

Figure 2 Free-body diagram of an infinitesimal segment with the length dx isolated from the micro-beam under forced vibration shown in Figure 1.

According to the D'Alembert's principle, the equilibrium of the isolated segment in Figure 2 along z-direction requires

$$Q(x,t)-q(x,t)\mathrm{d}x-[Q(x,t)+\frac{\partial Q(x,t)}{\partial x}\mathrm{d}x]-f_i(x,t)\mathrm{d}x=0 \tag{14}$$

The inertial force per unit length is calculated by

$$f_i(x,t)=-\rho A\frac{\partial^2 w(x,t)}{\partial t^2} \tag{15}$$

where ρ and A are the mass density and cross-section area, respectively. Substituting (15) to (14), one has the equilibrium equation

$$\frac{\partial Q(x,t)}{\partial x}-\rho A\frac{\partial^2 w(x,t)}{\partial t^2}+q(x,t)=0 \tag{16}$$

The moment equilibrium equation about the central point of the isolated segment in Figure 2 reads as

$$Q(x,t)\mathrm{d}x+M(x,t)-[M(x,t)+\frac{\partial M(x,t)}{\partial x}\mathrm{d}x]=0 \tag{17}$$

The simplification on (17) relates the bending moment to shear force as

$$\frac{\partial M(x,t)}{\partial x}=Q(x,t) \tag{18}$$

Substituting (18) into (16), the equilibrium equation is rewriten as

$$\frac{\partial^2 M(x,t)}{\partial x}-\rho A\frac{\partial^2 w(x,t)}{\partial t^2}+q(x,t)=0 \tag{19}$$

According to couple stress theory, the bending moment in a cross-section of the beam in Figure 1 is the result from both normal stress σ_{xx} and couple stress m_{xx} in the cross-section, namely

$$M(x,t)=\int_A z\sigma_{xx}\mathrm{d}A+\int_A m_{xy}\mathrm{d}A \tag{20}$$

Substituting the expression σ_{xx} of (12) and the expression m_{xx} of (13) into (20), one has

$$M(x,\,t)=-K\frac{\partial^2 w}{\partial x^2} \tag{21}$$

where K is the bending stiffness of beam as

$$K=(\lambda+2G)I+GAl^2 \tag{22}$$

with G and λ being the Lame's constants defined by (3) and (4) respectively, A being the area of cross-section and

$$I=\int_A z^2\mathrm{d}A \tag{23}$$

being the area second moment of cross-section. For a rectangular cross-section, $I = bh^3/12$, where b and h are the width and height of the rectangular cross-section respectively. For a circular cross-section, $I = \pi d^4/64$, where d is the diameter of the circular cross-section.

Substituting (21) into the equilibrium equation (19), one has the motion differential equation of a Bernoulli-Euler micro-beam

$$\rho A\frac{\partial^2 w(x,\,t)}{\partial t^2}+K\frac{\partial^4 w}{\partial x^4}=q(x,\,t) \tag{24}$$

where K is the bending stiffness of beam defined by (22).

4 Solution of micro-beam under forced vibration

4.1 Natural frequency

Letting q(x, t) = 0 in the motion differential equation (24), one has the free vibration differential equation of a Bernoulli-Euler beam

$$\rho A\frac{\partial^2 w(x,t)}{\partial t^2}+K\frac{\partial^4 w}{\partial x^4}=0 \tag{25}$$

According to method of separation of variables, one can assume the solution of differential equation (25) as the form

$$w(x,t)=\eta(t)\Phi(x) \tag{26}$$

where Φ(x) is called as mode function, and

$$\eta(t)=B\cos(\omega t)+C\sin(\omega t) \tag{27}$$

with ω being the natural frequency, B and C being the undetermined coefficients.

Substituting (26) and (27) into (25), one has

$$\frac{\mathrm{d}^4\Phi}{\mathrm{d}x^4}-\beta^4\Phi=0 \tag{28}$$

where

$$\beta^4=\frac{\rho A\omega^2}{K} \tag{29}$$

The general solution of the mode differential equation (28) reads as

$$\Phi(x)=C_1\sin(\beta x)+C_2\cos(\beta x)+C_3\sinh(\beta x)+C_4\cosh(\beta x) \tag{30}$$

where C_1, C_2, C_3 and C_4 are the undetermined coefficients.

For the simply supported beam in Figure 1, the displacement boundary conditions are

$$\Phi\big|_{x=0}=\Phi\big|_{x=L}=0,\quad \frac{\mathrm{d}^2\Phi}{\mathrm{d}x^2}\bigg|_{x=0}=\frac{\mathrm{d}^2\Phi}{\mathrm{d}x^2}\bigg|_{x=L}=0 \tag{31}$$

Substituting the mode equation (30) into the displacement boundary conditions (31) leads to $C_2 = C_3 = C_4 = 0$, and

$$\sin(\beta L)=0 \tag{32}$$

which requires

$$\beta=\frac{i\pi}{L}\quad (i=1,2,3,\cdots) \tag{33}$$

Then one can express the mode functions of the simply supported beam as

$$\Phi_i(x)=\sin(\frac{i\pi x}{L}) \quad (i=1,2,3,\cdots) \tag{34}$$

when $C_1 = 1$. From (29) and (33), one has the natural frequency of the simply supported beam

$$\omega_i=(i\pi)^2\sqrt{\frac{K}{\rho AL^4}} \quad (i=1,2,3,\cdots) \tag{35}$$

where K is the bending stiffness of beam defined by (22).

4.2 Orthogonality of mode functions

Using (28) and (29), one has

$$\frac{\mathrm{d}^2R_i}{\mathrm{d}x^2}=\omega_i^2\rho A\Phi_i(x) \tag{36}$$

where Φ_i and ω_i are the i^{th} order mode and natural frequency of the simply supported Bernoulli-Euler micro-beam in Figure 1 respectively, and

$$R_i(x)=K\frac{\mathrm{d}^2\Phi_i}{\mathrm{d}x^2} \tag{37}$$

with K being the bending stiffness after (22).

Multiplying both sides of (36) by the j^{th} order mode function $\Phi_j(x)$ and integrating them along the beam length, one has

$$\int_0^L\Phi_j(x)\frac{\mathrm{d}^2R_i}{\mathrm{d}x^2}dx=\int_0^L\Phi_j(x)\omega_i^2\rho A\Phi_i(x)\mathrm{d}x \tag{38}$$

For the left side of (38),

$$\int_0^L\Phi_j(x)\frac{\mathrm{d}^2R_i}{\mathrm{d}x^2}\mathrm{d}x=\Phi_j(x)\frac{\mathrm{d}R_i}{\mathrm{d}x}\Big|_0^L-\frac{\mathrm{d}\Phi_j}{\mathrm{d}x}R_i(x)\Big|_0^L+\int_0^L\frac{\mathrm{d}^2\Phi_j}{\mathrm{d}x^2}R_i(x)\mathrm{d}x \tag{39}$$

The boundary conditions of the simply supported beam in Figure 1 gives

$$\Phi_j(x)R'(x)\Big|_0^L=\Phi'_j(x)R(x)\Big|_0^L=0 \tag{40}$$

Substituting (40) and (37) into (39), one has

$$\int_0^L\Phi_j(x)\frac{\mathrm{d}^2R_i}{\mathrm{d}x^2}\mathrm{d}x=\int_0^L K\frac{\mathrm{d}^2\Phi_j}{\mathrm{d}x^2}\frac{\mathrm{d}^2\Phi_i}{\mathrm{d}x^2}\mathrm{d}x \tag{41}$$

where K being the bending stiffness after (22).

From (38) and (41), one has

$$K\int_0^L\frac{\mathrm{d}^2\Phi_j}{\mathrm{d}x^2}\frac{\mathrm{d}^2\Phi_i}{\mathrm{d}x^2}\mathrm{d}x=\omega_i^2\rho A\int_0^L\Phi_j(x)\Phi_i(x)\mathrm{d}x \tag{42}$$

Interchanging the subscripts i and j in (42) leads to

$$K\int_0^L\frac{\mathrm{d}^2\Phi_i}{\mathrm{d}x^2}\frac{\mathrm{d}^2\Phi_j}{\mathrm{d}x^2}\mathrm{d}x=\omega_j^2\rho A\int_0^L\Phi_i(x)\Phi_j(x)\mathrm{d}x \tag{43}$$

From (42) and (43), one has

$$(\omega_i^2-\omega_j^2)\int_0^L\Phi_j(x)\Phi_i(x)\mathrm{d}x=0 \tag{44}$$

The standard mode function of i^{th} order is defined as

$$\varphi_i(x)=\frac{\Phi_i(x)}{\sqrt{m_i}} \tag{45}$$

where

$$m_i=\rho A\int_0^L\Phi_i^2(x)\mathrm{d}x \tag{46}$$

Using (45), (46) and (44), one has

$$\int_0^L\rho A\varphi_i(x)\varphi_j(x)\mathrm{d}x=\delta_{ij}, \tag{47}$$

where δ_{ij} is the Kronecker delta symbol . (47) illustrates the orthogonality of mode functions.

4.3 Solution of forced vibration

According to the method of mode superposition, one can set the solution of the motion differential equation (24) as

$$w(x,t)=\sum_{j=1}^{\infty}\eta_j(t)\varphi_j(x), \tag{48}$$

where $\varphi_j(x)$ is the j^{th} order standard mode function expressed by (45). Substituting (48) into the motion differential equation (24), one has

$$\rho A\sum_{j=1}^{\infty}\varphi_j(x)\frac{\mathrm{d}^2\eta_j}{\mathrm{d}t^2}+K\sum_{j=1}^{\infty}\frac{\mathrm{d}^4\varphi_j}{\mathrm{d}x^4}\eta_j(t)=q(x,t) \tag{49}$$

Using (28) and (29) in (49), one has

$$\rho A\sum_{j=1}^{\infty}\varphi_j(x)\frac{\mathrm{d}^2\eta_j}{\mathrm{d}t^2}+\rho A\sum_{j=1}^{\infty}\omega_j^2\varphi_j(x)\eta_j(t)=q(x,t) \tag{50}$$

Multiplying both sides of (50) by the i^{th} order standard mode function $\varphi_i(x)$ and integrating them along the beam length with using the orthogonality of standard mode functions expressed in (47), one has

$$\frac{\mathrm{d}^2\eta_i}{\mathrm{d}t^2}+\omega_i^2\eta_i(t)=Q_i(t) \tag{51}$$

where

$$Q_i(t)=\int_0^L q(x,t)\varphi_i(x)\mathrm{d}x \tag{52}$$

According to (48), the initial condition of the simply supported micro-beam in Figure 1 can be expressed as

$$w(x,t)\Big|_{t=0}=\sum_{j=1}^{\infty}\eta_j(t)\Big|_{t=0}\varphi_j(x), \quad \frac{\partial w(x,t)}{\partial t}\Big|_{t=0}=\sum_{j=1}^{\infty}\frac{\mathrm{d}\eta_j}{\mathrm{d}t}\Big|_{t=0}\varphi_j(x) \tag{53}$$

Multiplying both sides of (53) by the i^{th} order standard mode function $\varphi_i(x)$ and integrating them along the beam length with using the orthogonality of standard mode functions in (47), one has

$$\eta_i(t)\Big|_{t=0}=\int_0^L w(x,t)\Big|_{t=0}\varphi_i(x)\mathrm{d}x, \quad \frac{\mathrm{d}\eta}{\mathrm{d}t}\Big|_{t=0}=\int_0^L\frac{\partial w}{\partial t}\Big|_{t=0}\varphi_i(x)\mathrm{d}x \tag{54}$$

Using the Duhamel integral, one obtains the solution of the differential equation (51) as

$$\eta_i(t)=\frac{1}{\omega_i}\int_0^t[Q_i(\tau)\sin\omega_i(t-\tau)]\mathrm{d}\tau+\eta_i(t)\Big|_{t=0}\cos\omega_i t+\frac{\mathrm{d}\eta}{\mathrm{d}t}\Big|_{t=0}\frac{\sin\omega_i t}{\omega_i} \tag{55}$$

Substituting (55) and (45) into (48) gives the solution of the Bernoulli-Euler simply supported micro-beam under forced vibration.

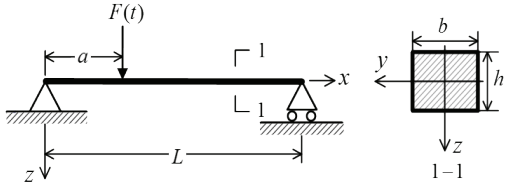

Figure 3 A simply supported Bernoulli-Euler micro-beam with rectangular section subjected a concentrated force, where F(t) is the concentrated force functioned by (56) and a is the distance between the point concentrated force applied and the left-hand side of beam.

Figure 3 shows a simply supported Bernoulli-Euler micro-beam subjected to a concentrated force formulated as

$$F(t) = P\sin(\omega_p t) \tag{56}$$

then the line density of distributed load is formulated as

$$q(x,t) = \begin{cases} 0 & \text{others} \\ \dfrac{P(t)}{\Delta} & (a \le x \le a+\Delta) \end{cases} \tag{57}$$

where Δ is an infinitesimal value. Substituting (57) into (52), one has

$$Q_i(t) = P\sqrt{\frac{2}{\rho AL}}\sin(\omega_p t)\sin(\frac{i\pi a}{L}) \tag{58}$$

Substituting (58) into (55) and using the initial conditions

$$\eta_i(t)\big|_{t=0} = 0 \quad \text{and} \quad \frac{\mathrm{d}\eta}{\mathrm{d}t}\bigg|_{t=0} = 0 \tag{59}$$

one has

$$\eta_i = \frac{P}{\omega_i^2 - \omega_p^2}\sqrt{\frac{2}{\rho AL}}\sin(\frac{i\pi a}{L})[\sin(\omega_p t) - \frac{\omega_p}{\omega_i}\sin(\omega_i t)] \tag{60}$$

Substituting (60) and (45) into (48) and using (34), one has the solution of forced vibration of the micro-beam in Figure 3,

$$w(x,t) = \sum_{i=1}^{\infty}\frac{2P}{\rho AL(\omega_i^2 - \omega_p^2)}\sin(\frac{i\pi x}{L})\sin(\frac{i\pi a}{L})[\sin(\omega_p t) - \frac{\omega_p}{\omega_i}\sin(\omega_i t)] \tag{61}$$

In order to investigate the size effect of the forced vibration of micro-beam conveniently, the dimensionless deflection is defined as

$$w'(x,t) = w(x,t)/(\frac{2P}{\rho gA}) \tag{62}$$

Substituting (61) into (62), the dimensionless deflection can be expressed as

$$w'(x,t) = \sum_{i=1}^{\infty} W_i(x)\Psi_i(t) \tag{63}$$

where

$$W_i(x) = \frac{g}{L(\omega_i^2 - \omega_p^2)}\sin(\frac{i\pi a}{L})\sin(\frac{i\pi x}{L}) \tag{64}$$

is called the i[th] order dimensionless amplitude mode and

$$\Psi_i(t) = \sin(\omega_p t) - \frac{\omega_p}{\omega_i}\sin(\omega_i t) \tag{65}$$

is called the i[th] order dimensionless period mode.

5 Analysis on forced vibration of micro-beam

In this section the micro-beam under forced vibration in Figure 3 is numerically investigated to reveal the size effects and the influences of Poisson's ratio, frequency ratio and loading location. The frequency ratio is defined as ω_p/ω_1, where ω_p and ω_1 are the load frequency and the first order natural frequency of the micro-beam, respectively.

Figure 4 shows the curves of dimensionless deflection versus dimensionless time of a point in the micro-beam under forced vibration in Figure 3 based on the front 1, 2, 3 and 4 orders of dimensionless modes of amplitude and period, respectively. The dimensionless deflection is calculated by (63) with x = L/2, and the dimensionless modes of amplitude and period are determined by (64) and (65), respectively. Figure 4(a) plots the curves during the period $T_p = 2\pi/\omega_p$ when the value of frequency ratio is 0.2. It is found that the curves based on the front 1, 2, 3 and 4 orders of dimensionless amplitude and period modes are very close and similar. Figure 4(b) plots the curves during the period $T_1 = 2\pi/\omega_1$ when the value of frequency ratio is 2.0, we can also see that the dimensionless amplitudes and periodic modes of the front 1, 2, 3, and 4 orders are very close. This means the first order dimensionless modes of amplitude and period are the main contribution to the solution of the micro-beam under forced vibration. Therefore the forced vibration of the micro-beam are calculated using only the first order dimensionless modes of amplitude and period in the following sections.

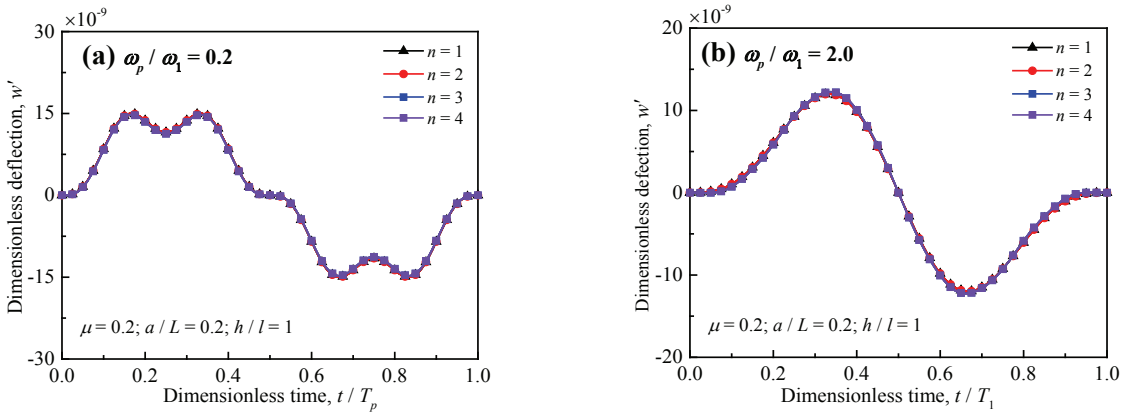

Figure 4 Curves of dimensionless deflection vs. dimensionless time of a point according to the front 1, 2, 3 and 4 orders of dimensionless amplitude and period modes, respectively.

On the other hand, comparisons between Figure 4(a) and Figure 4(b) illustrate that the frequency ratio is an important factor determining the performance of the micro-beam under forced vibration. Although when the frequency ratio is changed, the curve as a whole shows an "increasing-decreasing-increasing" trend, a small

frequency ratio will cause more fluctuations, and changing the frequency ratio can change the variation range of the dimensionless deflection.

5.1 Influences of frequency ratio

Figure 5 shows the curves of first order dimensionless amplitude mode of the micro-beam under forced vibration in Figure 3 with respect to the different values of frequency ratio. Figure 5(a) plots the curves when the value of frequency ratio is below 1.0. It is clear that each curve forms a hump and the altitude of hump rises with the increased value of frequency ratio when the value of frequency ratio is below 1.0. This means that the flexibility of the micro-beam under forced vibration increases with the increased value of frequency ratio when the value of frequency ratio is below 1.0. Figure 5(b) plots the curves when the value of frequency ratio is above 1.0. It is clear that each curve forms a hump and the altitude of hump declines with the increased value of frequency ratio when the value of frequency ratio is above 1.0. This means that the flexibility of the micro-beam under forced vibration decreases with the increased value of frequency ratio when the value of frequency ratio is above 1.0.

Figure 6 shows the curves of first order dimensionless period of the micro-beam under forced vibration in Figure 3 with respect to the different values of frequency ratio. Figure 6(a) plots the curves when the value of frequency ratio is below 1.0. Figure 6(b) plots the curves when the value of frequency ratio is above 1.0. It is found that the frequency ratio has significant influence on the period mode of micro-beam under forced vibration.

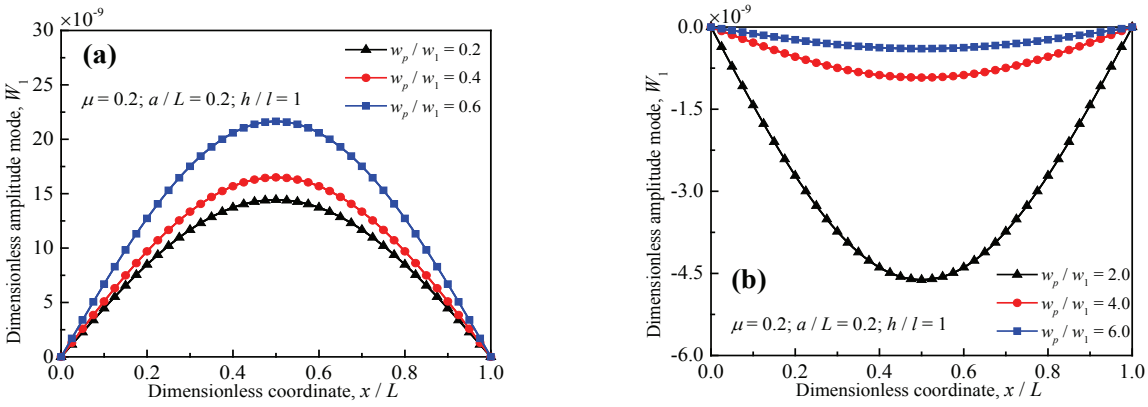

Figure 5 Curves of first order dimensionless amplitude mode of the micro-beam under forced vibration with respect to the different values of frequency ratio.

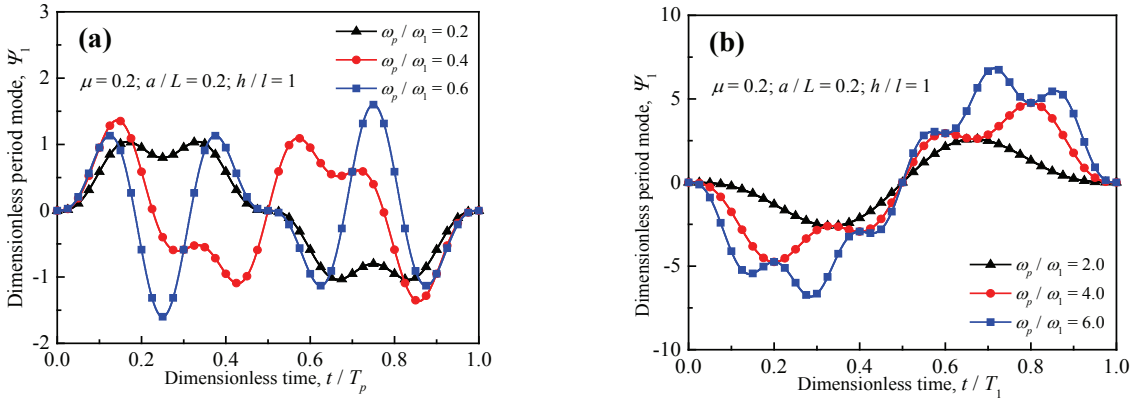

Figure 6 Curves of first order dimensionless period mode of the micro-beam under forced vibration with respect to the different values of frequency ratio.

Figure 7 shows that the curves of dimensionless deflection versus dimensionless time of a point in the micro-beam under forced vibration in Figure 3 with respect to the different values of frequency ratio. Figure 7(a) plots the curves when the value of frequency ratio is below 1.0. Figure 7(b) plots the curves when the value of frequency ratio is above 1.0. It is clear that the frequency ratio has a significant influence on the performance of the micro-beam under forced vibration.

5.2 Size effect of forced vibration

Figure 8 shows the curves of the first order dimensionless amplitude mode of the micro-beam under forced vibration in Figure 3 with respect to the different values of dimensionless height, where L and h are the length and height of the micro-beam, respectively, and l is the material length-scale parameter. The first order dimensionless amplitude mode is calculated by (64) and the dimensionless

height is defined as the ratio of the height of micro-beam to the material length-scale parameter h/l. Figure 8(a) plots the curves when the value of frequency ratio is 0.2. It is clear that each curve is with a shape of hump, and the altitude of hump increases with the increased value of dimensionless height. This illustrates that the flexibility of the micro-beam under forced vibration rises with the increased value of dimensionless height. Figure 8(b) plots the curves when the value of frequency ratio is 2.0. The comparisons between Figure 8(a) and Figure 8(b) show that the frequency ratio has a significant influence on the amplitude mode of the micro-beam under forced vibration.

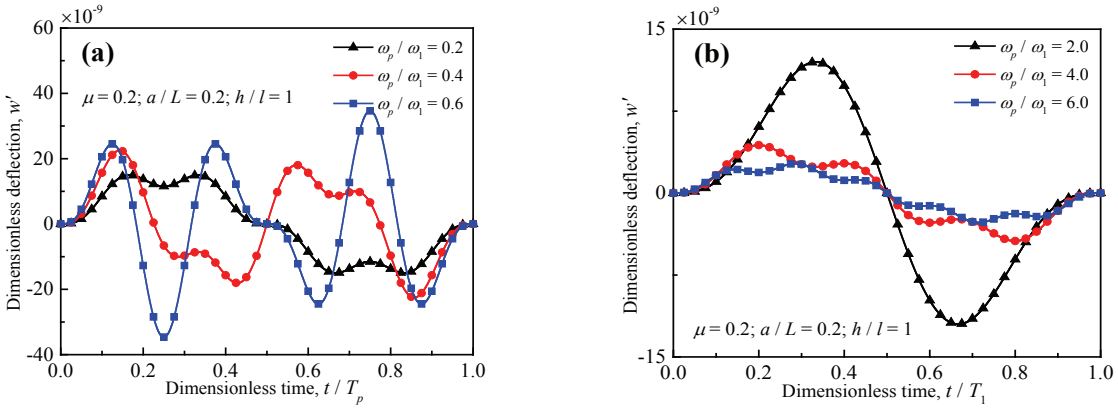

Figure 7 Curves of dimensionless deflection vs. dimensionless time of a point in the micro-beam with respective to the different values of frequency ratio.

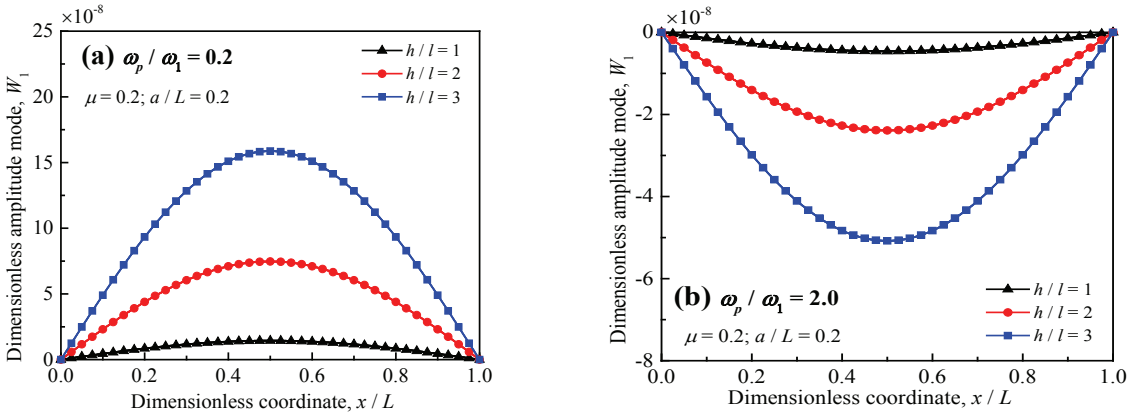

Figure 8 Curves of first order dimensionless amplitude mode of the micro-beam under forced vibration with respect to the different values of dimensionless height.

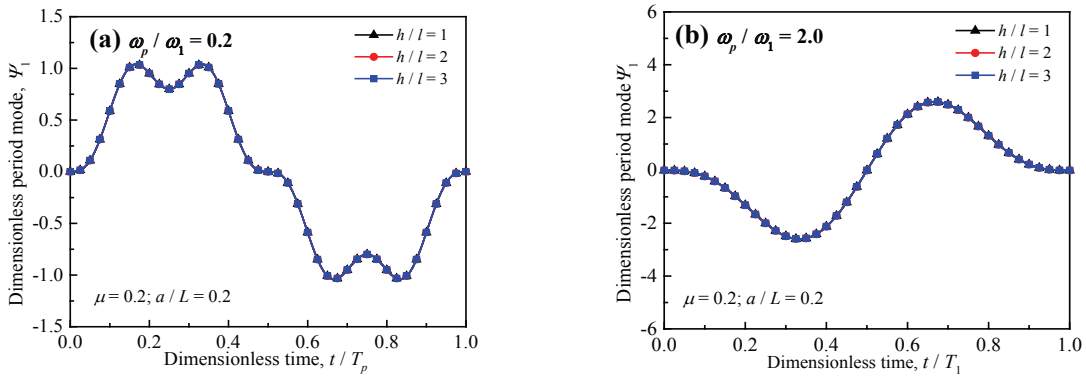

Figure 9 Curves of first order dimensionless period mode of the micro-beam under forced vibration with respect to the different values of dimensionless height.

Figure 9 shows the curves of first order dimensionless period mode of the micro-beam under forced vibration in Figure 3 with respect to the different values of dimensionless height, where the first order dimensionless period mode is calculated by (65). Figure 9(a) plots the curves during the period $T_p = 2\pi/\omega_p$ when the value of frequency ratio is 0.2.

It is clear that the curves with respect to the different values of dimensionless height are very close and similar, which illustrates that the dimensionless height has little influence on the period mode of the micro-beam under forced vibration. Figure 9(b) plots the curves during the period $T_1 = 2\pi/\omega_1$ when the value of frequency ratio is 2.0. The comparisons between Figure 9(a) and Figure 9(b) show that the frequency ratio ω_p/ω_1 has a significant influence on the period mode of the micro-beam under forced vibration.

Figure 10 shows the curves of dimensionless deflection versus dimensionless time of a point in the micro-beam under forced vibration in Figure 3 with respect to the different values of dimensionless height, where the dimensionless deflection is calculated by (63) with x = L/2 based on the first order modes of dimensionless amplitude and period. Figure 10(a) plots the curves during the period $T_p = 2\pi/\omega_p$ when the value of frequency ratio is 0.2. It is clear that the curve vertically extends with the increased value of dimensionless height. This is due to that the flexibility of the micro-beam increases with the increased value of dimensionless height. Figure 10(b) plots the curves during the period $T_1 = 2\pi/\omega_1$ when the value of frequency ratio is 2.0. The comparisons between Figure 10(a) and Figure 10(b) show that the frequency ratio ω_p/ω_1 has a significant influence on the performance of the micro-beam under forced vibration.

5.3 Influences of loading location

Figure 11 shows that the curves of first order dimensionless amplitude mode of the micro-beam under forced vibration in Figure 3 with respect to the different loading locations. Figure 11(a) and Figure 11(b) plot the curves when the values of frequency are 0.2 and 2.0, respectively. It is found that the loading location has an obvious influence on the amplitude mode of the micro-beam under the forced vibration. It is also found that the frequency ratio has an obvious influence on the dimensionless amplitude mode of the micro-beam under the forced vibration.

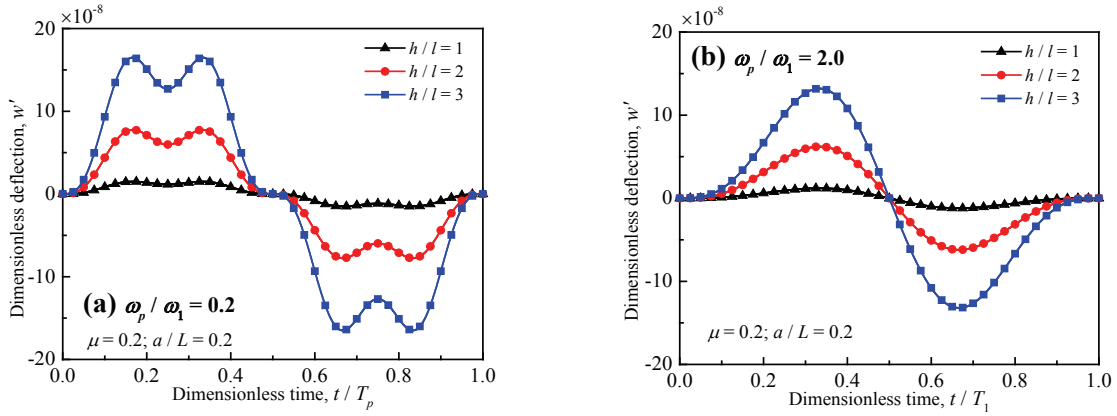

Figure 10 Curves of dimensionless deflection vs. dimensionless time of a point in the micro-beam with respect to the different values of dimensionless height.

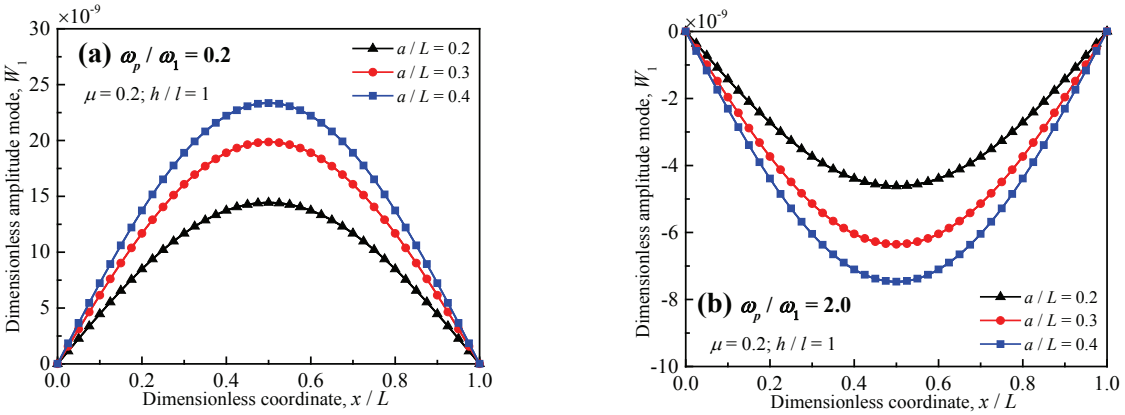

Figure 11 Curves of first order dimensionless amplitude mode of the micro-beam under forced vibration with respect to the different location load applied.

Figure 12 shows the curves of first order dimensionless period mode of the micro-beam under forced vibration in Figure 3 with respect to the different loading locations. Figure 12(a) and Figure 12(b) plot the curves when the values of frequency are 0.2 and 2.0, respectively. It is found that the loading location has little influence on the period mode of the micro-beam under the forced vibration. It is also clear that the frequency ratio has a significant influence on the period mode of the micro-beam under the forced vibration.

Figure 13 shows the curves of dimensionless deflection

versus dimensionless time of the micro-beam under forced vibration in Figure 3 with respect to the different loading locations. Figure 13(a) and Figure 13(b) plot the curves when the values of frequency are 0.2 and 2.0, respectively. It is found that the loading location has obvious influence on the performance of the micro-beam under the forced vibration. It is also clear that the frequency ratio has obvious influence on the performance of the micro-beam under the forced vibration.

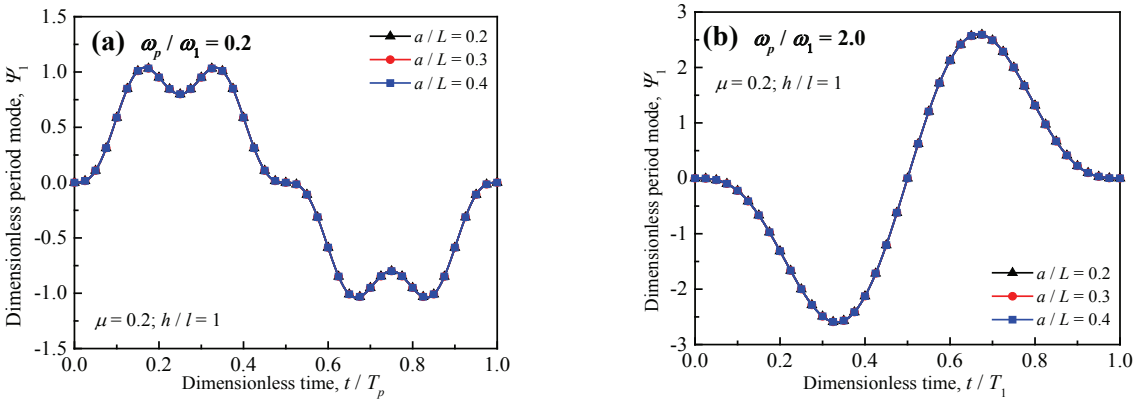

Figure 12 Curves of first order dimensionless period mode of the micro-beam under forced vibration with respect to the different location load applied.

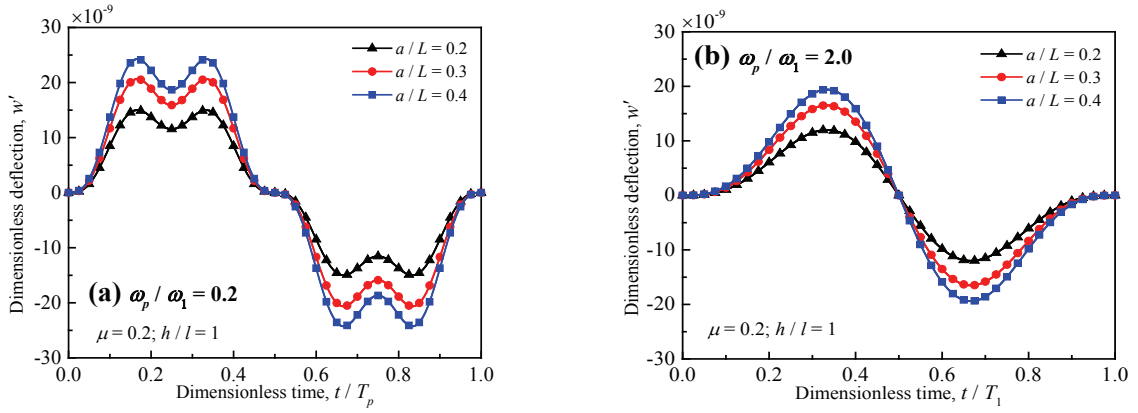

Figure 13 Curves of dimensionless deflection vs. dimensionless time of a point in the micro-beam with respect to the different location load applied.

6 Conclusions

The components of strain, curvature, stress and couple stress of a micro-beam are formulated according to the MCST and Bernoulli-Euler beam theory. The motion differential equation of a micro-beam is derived by using the D'Alembert's principle. The solution of a micro-beam under forced vibration is obtained by using the method of separation of variables. Based on the numerical results, the important conclusions related to the behaviors of a micro-beam under forced vibration are summarized as follows.

1) The size effects of a micro-beam under forced vibration, which includes the size effects of deflection, amplitude mode and period mode, are obvious when the value of dimensionless height is small enough.

2) The frequency ratio has a significant influence on both dimensionless modes of amplitude and period of a micro-beam under forced vibration, therefore it is the important factor that determines the behaviors of a micro-beam under forced vibration.

3) The loading location has a significant influence on the dimensionless amplitude mode of a micro-beam under the forced vibration, however its influence on the dimensionless period mode of a micro-beam under the forced vibration is negligible.

Author Contributions: Bo ZHOU first proposed a method to analyze the size-dependently mechanical behaviors of a micro-beam under forced vibration by using modified couple stress theory, Bernoulli-Euler beam theory and D'Alembert's principle. Shuai WANG solved a simply supported micro-beam under forced vibration according to the established governing equations and the method of separation of variables, and defined the dimensionless deflection, amplitude mode and period mode to investigate the size-dependently mechanical behaviors of a micro-beam under forced vibration. Zhiyong WANG established the governing equations of a micro-beam under forced

vibration. Feifei WANG summarized the results of numerical simulation. Shifeng XUE put forward some guiding opinions on the logicality and innovation of the article.

Conflict of Interest: We declare that there is no conflict of interest regarding the publication of this paper.

Acknowledgments: The authors of this paper acknowledge the supports from the National Key Research and Development Program of China (Grant No. 2017YFC0307604) and the Talent Foundation of China University of Petroleum (Grant No. Y1215042).

This is the Appendix: This article does not cover the details that require an appendix.

References

[1] Chen, S., Baughn, T. V., Yao, Z. J., and Goldsmith, C. L. A new in situ residual stress mea¬surement method for a mems thin fixed-fixed beam structure. Journal of Microelectromechanical Systems, 11(4), 309–316 (2002)

[2] Li, M., Huang, Q. A., and Li, W. H. A nodal analysis method for electromechanical behavior simulation of bow-tie shaped microbeams. Microsystem Technologies, 15(7), 985-991 (2009)

[3] Dai, H. L., Wang, Y. K., and Wang, L. Nonlinear dynamics of cantilevered microbeams based on modified couple stress theory. International Journal of Engineering Science, 94(2), 103–112 (2015)

[4] Muniraj, N. J. R. Mems based humidity sensor using Si cantilever beam for harsh environmental conditions. Microsystem Technologies, 17(1), 27–29 (2011)

[5] Nallathambi, A., and Shanmuganantham, T. Performance analysis of cantilever based MEMS sensor for environmental applications. 2014 International Conference on Smart Structures and Systems (ICSSS),IEEE, 2015.

[6] Shoaib, M. , Khamis, N. H. , Basheer, N. , and Tariq, M. Frequency and displacement analysis of electrostatic cantilever-based mems sensor. Analog Integrated Circuits and Signal Processing, 88(1), 1–11 (2016)

[7] Zhang, W., Meng, G., and Li, H. Adaptive vibration control of micro-cantilever beam with piezo-electric actuator in mems. International Journal of Advanced Manufacturing Technology, 28(3-4), 321–327 (2006)

[8] Li, X., Zhao, Y., Hu, T., Xu, W., Zhao, Y., and Bai, Y. Design of a large displacement thermal actuator with a cascaded v-beam amplification for mems safety-and-arming devices. Microsystem Technologies, 21(11), 2367–2374 (2015)

[9] Harsha, C. S., Prasanth, C. S., and Pratiher, B. Prediction of pull-in phenomena and structural stability analysis of an electrostatically actuated microswitch. Acta Mechanica, 227(9), 2577–2594 (2016)

[10] Fleck, N. A., Muller, G. M., Ashby, M. F., and Hutchinson, J. W. Strain gradient plasticity: theory and experiment. Acta Metal Mater, 42(2), 475–487 (1994)

[11] J.S., St¨olken, and A.G., Evans. A microbend test method for measuring the plasticity length scale. Acta Materialia, 46(14), 5109–5115 (1998)

[12] Toupin, R. A. Elastic materials with couple-stresses. Archive for Rational Mechanics and Analysis, 11(1), 385–414 (1962)

[13] Mindlin, R. D. Micro-structure in linear elasticity. Archive for Rational Mechanics and Analysis, 16(1), 51–78 (1964)

[14] Fleck, N. A., and Hutchinson, J. W. A reformulation of strain gradient plasticity. Journal of the Mechanics and Physics of Solids, 49(10), 2245–2271 (2001)

[15] Huang, Y., Qu, S., Hwang, K. C., Li, M., and Gao, H. A conventional theory of mechanism-based strain gradient plasticity. International Journal of Plasticity, 20(4), 753–782 (2004)

[16] Hadjesfandiari, A. R., and Dargush, G. F. Couple stress theory for solids. International Journal of Solids and Structures, 48(18), 2496–2510 (2011)

[17] Ansari, R., Gholami, R., Shojaei, M. F., Mohammadi, V., and Sahmani, S. Size-dependent bend¬ing, buckling and free vibration of functionally graded timoshenko microbeams based on the most general strain gradient theory. Composite Structures, 100(5), 385–397 (2013)

[18] Liang, X., Hu, S., and Shen, S. A new Bernoulli-Euler beam model based on a simplified strain gradient elasticity theory and its applications. Composite Structures, 111(1), 317–323 (2014)

[19] Alashti A. R., and Abolghasemi, A. H. A size-dependent Bernoulli-Euler beam formulation based on a new model of couple stress theory. International Journal of Engineering Transactions C, 27(6), 951–960 (2014)

[20] Yang, F., Chong, A. C. M., Lam, D. C. C., and Tong, P. Couple stress based strain gradient theory for elasticity. International Journal of Solids and Structures, 39(10), 2731–2743 (2002)

[21] Park, S. K. and Gao, X. L. Variational formulation of a modified couple stress theory and its application to a simple shear problem. Zeitschrift Fu¨r Angewandte Mathematik Und Physik, 59(5), 904–917 (2008)

[22] Park, S. K. and Gao, X. L. Bernoulli-euler beam model based on a modified couple stress the-ory.Journal of Micromechanics and Microengineering, 16(11), 2355–2359 (2006)

[23] Ma, H. M., Gao, X. L., and Reddy, J. N. A microstructure-dependent timoshenko beam model based on a modified couple stress theory. Journal of the Mechanics

and Physics of Solids, 56(12), 3379–3391 (2008)

[24] Kong, S., Zhou, S., Nie, Z., and Wang, K. The size-dependent natural frequency of bernoulli-euler micro-beams. International Journal of Engineering Science, 46(5), 427–437 (2008)

[25] Mohammad-Abadi, M., and Daneshmehr, A. R. Modified couple stress theory applied to dynamic analysis of composite laminated beams by considering different beam theories. International Jour-nal of Engineering Science, 87, 83–102 (2015)

[26] Dehrouyeh-Semnani, A. M., and Nikkhah-Bahrami, M. The influence of size-dependent shear deformation on mechanical behavior of microstructures-dependent beam based on modified couple stress theory. Composite Structures, 123, 325–336 (2015)

Publisher: Viser Technology Pte. Ltd.

URL: www.viserdata.com

Add.:21 Woodlands Close, #08-18,

Primz Bizhub SINGAPORE (737854)